

AD-A247 551

PL-TR-91-2191 (I)

E 200 837

J.V
②

THE DESIGN, DEVELOPMENT AND TEST OF BALLOONBORNE
AND GROUNDBASED LIDAR SYSTEMS
Volume 1: Balloonborne Coherent CO₂ Lidar System

O. Shepherd
G. Aurilio
R. D. Bucknam
A. G. Hurd

S. A. Rappaport
W. P. Reidy
R. J. Rieder
N. F. Robertie

W. H. Sheehan

Visidyne, Inc
10 Corporate Place
South Bedford Street
Burlington, MA 01803

1 June 1991

DTIC
SELECTED
FEB 11 1992
S B D

Final Report
30 May 1986-31 December 1990

APPROVED FOR PUBLIC RELEASE; DISTRIBUTION UNLIMITED



PHILLIPS LABORATORY
AIR FORCE SYSTEMS COMMAND
HANSOM AIR FORCE BASE, MASSACHUSETTS 01731-5000

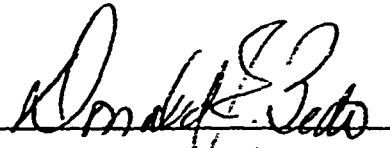
92-03186

02 2 02 033

This technical report has been reviewed and is approved for publication.



Robert A. Swirbalus
Contract Manager



Donald E. Bedo, Chief
Electro-Optical Measurements Branch



Alan D. Blackburn, Col., USAF
Director, Optical Environment Division

This document has been reviewed by the ESD Public Affairs Office (PA) and is releasable to the National Technical Information Service (NTIS).

Qualified requestors may obtain additional copies from the Defense Technical Information Center. All others should apply to the National Technical Information Service.

If your address has changed, or if you wish to be removed from the mailing list, or if the addressee is no longer employed by your organization, please notify PL/IMA, Hanscom AFB, MA 01731-5000. This will assist us in maintaining a current mailing list.

Do not return copies of this report unless contractual obligations or notices on a specific document requires that it be returned.

REPORT DOCUMENTATION PAGE

Form Approved
OMB No. 0704-0193

This form is used for the submission of information to DODD-1. Your use of this form indicates your understanding of the information contained therein, including the fact that it may be used for purposes other than its intended purpose. The information contained in this document is not to be distributed outside the Defense Department without prior approval of the Defense Secretary or his/her designee. It is to be controlled by the Defense Security Classification Control System. Distribution, handling, storage, and disposal shall be in accordance with Defense Security Classification Control System Instructions and Regulations. DOD Form 298, Revision 2, 28 SEP 89, and DOD Instruction 3210.2, Distribution Control System, 10 SEP 89.

1. AGENCY USE ONLY (Leave blank)			2. REPORT DATE 1 June 1991		3. REPORT TYPE AND DATES COVERED Final - 5/30/86 - 12/31/90		
4. TITLE AND SUBTITLE The Design, Development, and Test of Balloonborne and Groundbased Lidar Systems, Volume 1 - Balloonborne Coherent CO₂ Lidar System			5. FUNDING NUMBERS F19628-S6-C-0105 PE 62101F PR 7670 TA 16 WUAA				
6. AUTHOR(S) G. Shepherd, G. Aurilio, K.D. Bucknam, A.G. Hurd, S.A. Rappaport, W.P. Reidy, R.J. Rieder, N.F. Robertson, and W.H. Sheehan			8. PERFORMING ORGANIZATION REPORT NUMBER VI-1707-A				
7. PERFORMING ORGANIZATION NAME(S) AND ADDRESS(ES) Visidyne, Inc. 10 Corporate Place South Bedford St. Burlington, MA 01803			9. SPONSORING/MONITORING AGENCY NAME(S) AND ADDRESS(ES) Phillips Laboratory Hanscom AFB, Massachusetts 01731-5000 Contract Manager: R. Swirbalus/OPA				
11. SUPPLEMENTARY NOTES			10. SPONSORING/MONITORING AGENCY REPORT NUMBER PI-TR-91-2191 (1)				
12a. DISTRIBUTION AVAILABILITY STATEMENT Approved for public release; Distribution unlimited			12b. DISTRIBUTION CODE				
13. ABSTRACT (Maximum 200 words) This final report is in three volumes which describe the work performed under the above contract. This is Volume 1 of the three. Volume 2 describes the flight test of Atmospheric Balloonborne Lidar Experiment, ABLE II, which successfully made atmospheric density backscatter measurements during a flight over White Sands Missile Range. Volume 3 describes groundbased lidar development and measurements, including the design of a telescope dome lidar installation, the design of a transportable lidar shed for remote field sites, and field measurements of atmospheric and cloud backscatter from Ascension Island during SABLE 89 and Terciera, Azores during GABLE 90.							
In this volume, Volume 1, the design and fabrication of a balloonborne CO ₂ coherent lidar payload are described. The purpose of this payload is to measure, from altitudes greater than 20 km, the 10.6 μm backscatter from atmospheric aerosols as a function of altitude. Minor modifications to the lidar would provide for aerosol velocity measurements to be made. The lidar and payload system design was completed, and major components were fabricated and assembled.							
These tasks have been successfully completed, and recommendations for further lidar measurements and data analysis have been made.							
14. SUBJECT TERMS Coherent lidar, Balloonborne payload, 10.6 μm backscatter, CO ₂ laser, Aerosol backscatter, Wind velocities				15. NUMBER OF PAGES 118			
				16. PRICE CODE			
17. SECURITY CLASSIFICATION OF REPORT UNCLASSIFIED		18. SECURITY CLASSIFICATION OF THIS PAGE UNCLASSIFIED		19. SECURITY CLASSIFICATION OF ABSTRACT UNCLASSIFIED		20. LIMITATION OF ABSTRACT SAR	

TABLE OF CONTENTS

<u>Section</u>	<u>Page</u>
1. INTRODUCTION	1
2. THEORY OF OPERATION	2
2.1 Heterodyne Detection	6
2.2 Transmit/Receive Switch	6
3. SIMULATION OF A COHERENT LIDAR SIGNAL	8
3.1 Introduction	8
3.2 Simulation of Return Signal	12
3.2.1 No Doppler Shifts, Uniform Atmosphere	12
3.2.2 Nonuniform Atmosphere, Photon Statistics, Pulse-to-Pulse Variations	21
3.2.3 Doppler Effects Due to Winds	29
3.3 Lidar SNR Simulations	32
4. LIDAR DESCRIPTION	36
4.1 CO ₂ Laser Description	36
4.2 Laser Operation	36
4.3 Transmit-Receive Switch	40
4.3.1 Quarter Wave Plate	40
4.3.2 Brewster Window	43
4.4 Telescope	45
4.4.1 Specifications	45
4.4.2 Initial Design Considerations	45
4.4.3 Mechanical and Thermal Considerations	49
4.5 Optical Alignment and Beam Characteristics	53
4.5.1 Detector Size	55
4.5.2 Transmitted Beam	55
4.5.3 Received Beam	58
4.5.4 Lidar Wave Front Error	65

TABLE OF CONTENTS

<u>Section</u>	<u>Page</u>
5. SIGNAL PROCESSING	70
5.1 Local Oscillator Power	70
5.2 Electronics	70
6. BALLOON PAYLOAD	75
6.1 Mechanical Design	75
6.2 Thermal Control System	90
6.3 Power	90
6.4 Data	95
6.5 Experiment Control Software	95
6.6 Functional Description	105
7. CURRENT STATUS OF CO ₂ LIDAR SYSTEM	107
8. TASKS TO BE DONE	108
9. CONCLUSIONS AND RECOMMENDATIONS	109
10. REFERENCES	110

Accession For	
NTIS GRA&I <input checked="" type="checkbox"/> DTIC TAB <input type="checkbox"/> Unannounced <input type="checkbox"/>	
Justification	
By	
Distribution/	
Availability Codes	
Dist	Avail and/or Special
A-1	3.



LIST OF FIGURES

<u>Figure</u>	<u>Page</u>
1 10.6 μm lidar transmitter including CO ₂ , TEA laser	3
2 Lidar receiver optical bench layout	4
3 Chamber mounting of lidar system	5
4 Laser pulse	9
5 Fourier transform of laser pulse	10
6 Schematic of lidar shot Fourier transform	13
7 Fourier transform of laser pulse	15
8 Random phases and amplitudes	15
9 Return lidar signals	16
10 Envelope detector	17
11 Output of envelope circuit	18
12 Output of low-pass filter	18
13 Filtered return lidar shot, 0.03 μs bins	19
14 Filtered return lidar shot, 0.5 μs bins	19
15 Amplitude distribution in return shot #1	20
16 Amplitude distribution in return shot #2	20
17 Effects of photon statistics on the detected background signal, $N_{l,0} = 10^5$, $N_{rs} = 4 \times 10^4$	26
18 Effects of photon statistics on the detected background signal, $N_{l,0} = 10^5$, $N_{rs} = 4000$	26
19 Effects of photon statistics on the detected background signal, $N_{l,0} = 10^5$, $N_{rs} = 800$	27
20 Effects of photon statistics on the detected background signal, $N_{l,0} = 10^5$, $N_{rs} = 400$	27
21 Effects of photon statistics on the detected background signal, $N_{l,0} = 10^5$, $N_{rs} = 200$	28
22 Effects of photon statistics on the detected background signal, $N_{l,0} = 10^5$, $N_{rs} = 100$	28

LIST OF FIGURES

<u>Figure</u>	<u>Page</u>
23 Output vs. input of envelope detector	30
24 SNR vs. range for various balloon heights	33
25 SNR at different altitudes vs. balloon height	34
26 Outline drawing of LSI CO ₂ TEA laser	38
27 CO ₂ laser output pulse	39
28 Brewster window transmission efficiency	44
29 Brewster window reflection efficiency	44
30 Lidar telescope optical layout	46
31 Balloonborne coherent CO ₂ lidar telescope structure	51
32 Moment of inertia, perforated tube vs. wall thickness	52
33 Detector spectral response	57
34 Intensity of the incident radiation of the following lens as a function of the radial distance	61
35 Phase of the incident radiation of the focusing lens as a function of radial distance	62
36 Diffraction pattern at lens focal plane	63
37 Integrated energy at detector vs. off-axis angle	64
38 Signal processing electronics	71
39 Lidar payload electronics	73
40 Lidar pressure chamber	77
41 Laser power supply chamber	78
42 Laser power supply rack	79
43 Balloonborne coherent CO ₂ lidar payload, side view	80
44 Balloonborne coherent CO ₂ lidar payload, top view	81
45 Lidar payload, assembled mechanical structure	82
46 Coherent CO ₂ lidar receiver optical bench	83
47 CO ₂ la	84
48 Receiver optical bench mounted in lidar pressure chamber	85

LIST OF FIGURES

<u>Figure</u>		<u>Page</u>
49	Laser power supplies and controls mounted in pressure chamber rack	86
50	Chamber installation of laser power supply rack	87
51	CO ₂ lidar thermal control system	93
52	Program BCBL architecture	106

LIST OF TABLES

<u>Table</u>	<u>Page</u>
1 Laser Specifications	37
2 CdS $\lambda/4$ - Wave Sensitivities	42
3 Telescope Specifications	47
4 Remote Adjustments Used for Alignment	54
5 Lidar Heterodyne Detector Characteristics	56
6 Degradation of Heterodyne Modulation as a Function of Wave Front Error	66
7 Wave Front Error Summary for CO ₂ Lidar $\lambda = 10.6 \mu\text{m}$	67
8 Balloon Payload Environmental Specifications	76
9 CO ₂ Lidar Payload Weight Budget	88
10 Balloon Payload Thermal Environmental Design Specifications	91
11 Thermal Load Summary	92
12 Payload Power Summary	94
13 Thermal Control Monitors/Data	96
14 CO ₂ Laser Data	97
15 Receiver Data	98
16 CO ₂ Laser Controls	99
17 Receiver Controls	100
18 Thermal Control Functions	101
19 CO ₂ Lidar Payload	102
20 High Reliability/Safety Commands	103
21 Balloon Control	104

1.0 INTRODUCTION

A balloonborne platform can be used to make downward-looking $10.6 \mu\text{m}$ aerosol backscatter measurements from near space. These backscatter data are required to support the design of future global wind measurement satellites. The use of a balloon measurement platform is a low cost alternative to a satellite lidar system, and the design-to-flight time is considerably shorter than that of a space system. The high altitude environment of a balloon platform is similar to that of space systems; thus balloonborne lidars can serve as test beds for future space systems.

The objective of this effort was to design, fabricate, and test a balloonborne coherent CO₂ lidar to measure the aerosol backscatter at $10.6 \mu\text{m}$ as a function of altitude. The lidar beam would be directed downward as the balloon payload ascended to an altitude of greater than 20 km. The lidar backscatter return signal is time-resolved and arranged to obtain 1 km altitude resolution of the backscatter. The system is capable of being upgraded to acquire aerosol velocity data.

The advantages of this payload result from the optical bench configuration, the coaxial transmitter/receiver telescope, and the static transmit-receive switch.

The design of the balloonborne coherent CO₂ lidar experiment is based on previous Visidyne balloonborne lidar systems which are described in References 1 and 2 and in Volume 2 of this report.

2.0 THEORY OF OPERATION

The $10.6 \mu\text{m}$ lidar transmitter is a CO₂ Transverse-Excitation Atmospheric-Pressure (TEA) laser (see Fig. 1) developed by Laser Science Inc. (LSI). A schematic drawing of the lidar receiver optical bench is shown in Fig. 2. In the balloon configuration the laser is mounted on the top side of the optical bench and the optical components for the lidar receiver are mounted on the bottom side. This arrangement, shown in Fig. 3, provides an interferometrically rigid mount for all of the lidar optics. The pulsed laser beam is transmitted from the top of the bench to the bottom side by beam directors. When the laser beam arrives on the lidar side it is polarized in the plane of the optical bench. It is directed to the secondary mirror of the off-axis telescope passing through a Brewster window and a quarter-wave plate. The quarter-wave plate converts the linearly polarized beam to circularly polarized. The telescope optics then spatially expand the beam and decrease its divergence. Finally, the beam is transmitted through a chamber window which is transparent at $10.6 \mu\text{m}$ and is directed downward by a fixed diagonal plane mirror.

The transmitted beam is backscattered by atmospheric aerosols which reverse the direction of its circular polarization. This backscattered radiation is collected by the afocal telescope and reduced to a narrow collimated beam after the secondary mirror. This received beam is then directed onto the quarter-wave plate which converts the circularly polarized beam back to linear polarization. The beam is then incident on the Brewster window which now reflects the beam because of its polarization onto a folding mirror. It continues through the beamsplitter, lens, and finally onto the face of the detector.

The return signals are on the order of 10^{-13} - 10^{-11} watts per laser pulse when scattering from an atmospheric volume one kilometer thick. Typical values for detector noise are approximately 10^{-11} watts. Thus the return signal cannot be discerned from the noise, and therefore direct detection cannot be used. Heterodyne detection can be used to great advantage to measure small signals in the presence of detector noise. To implement this technique a reference laser beam, the local oscillator (LO), is optically mixed with the return signal. The LO is a frequency-stable cw CO₂ laser which is the frequency reference of the TEA laser. The LO beam is transmitted to the lidar side and onto the beamsplitter by means of a series of beam directors. Heterodyne

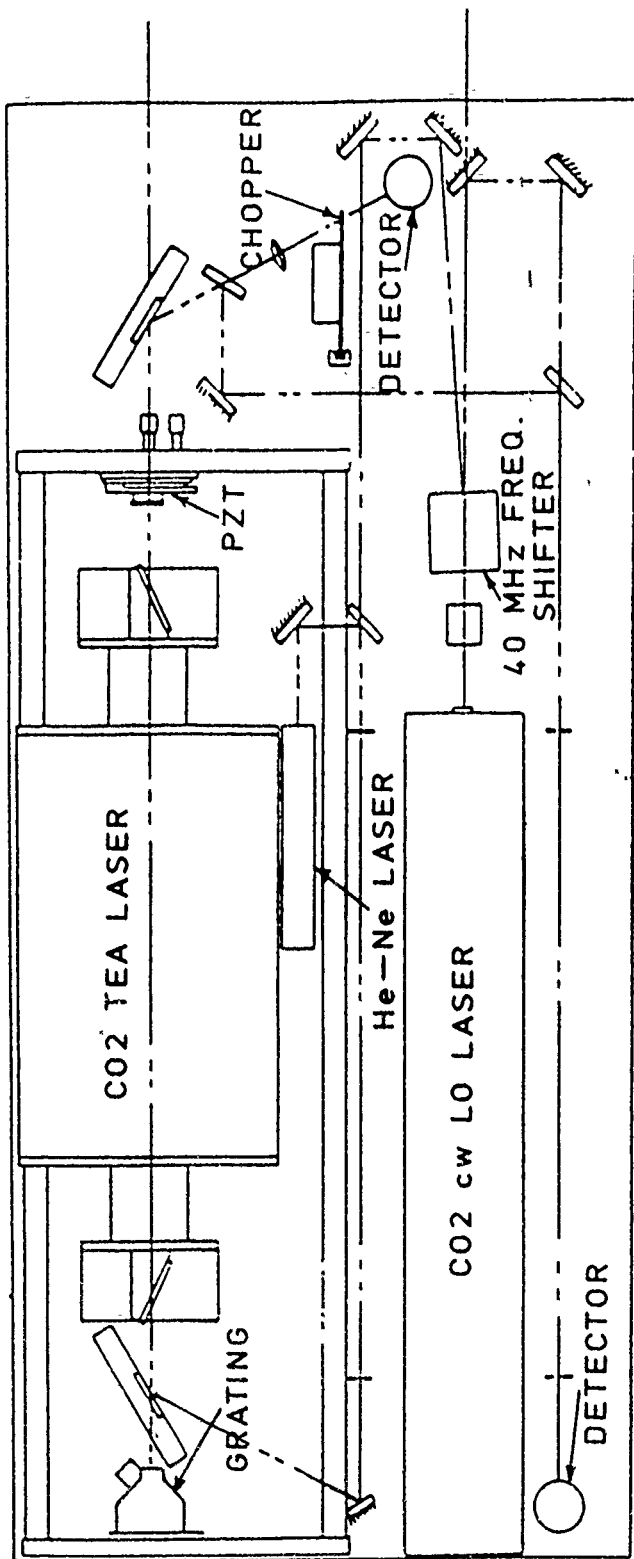


Figure 1. 10.6 μm lidar transmitter including CO₂ TEA laser.

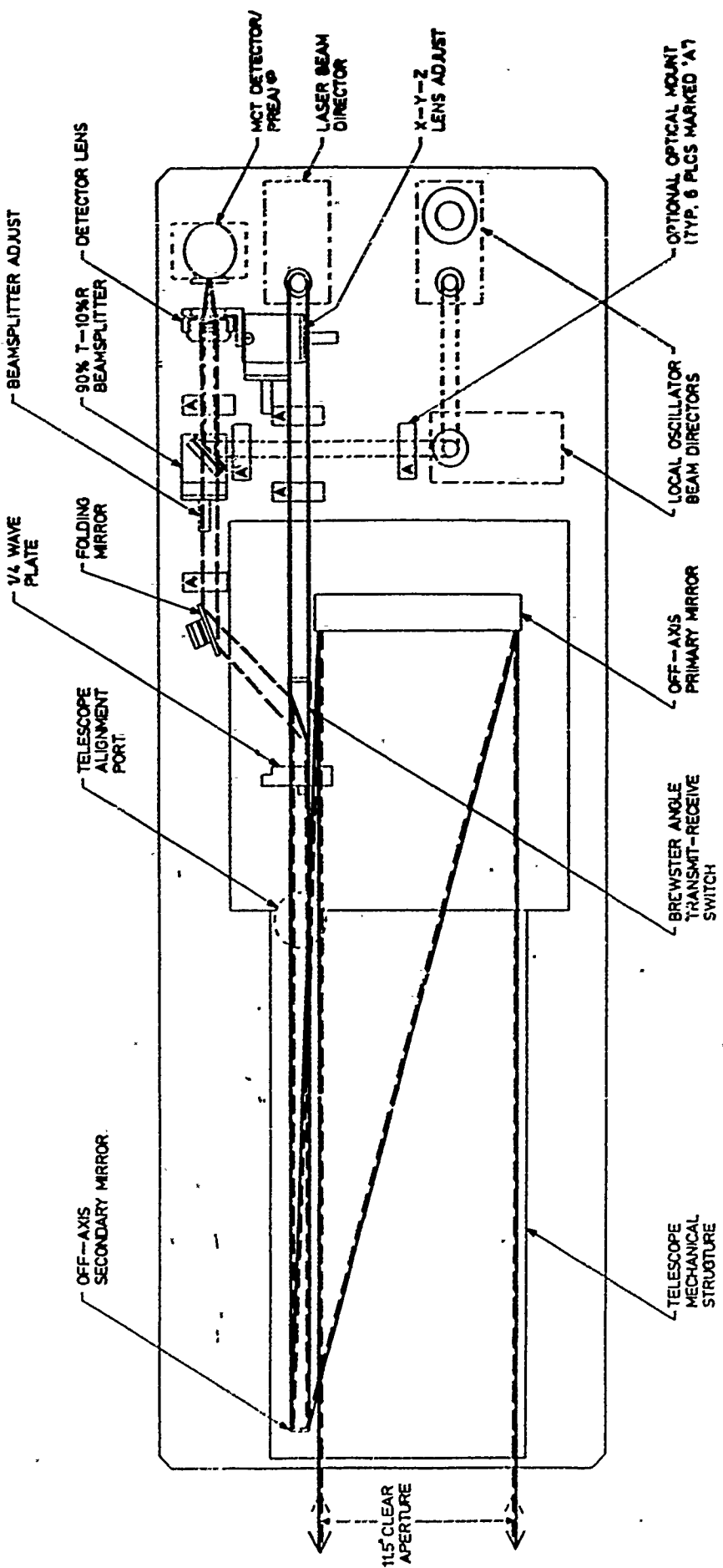


Figure 2. Lidar receiver optical bench layout.

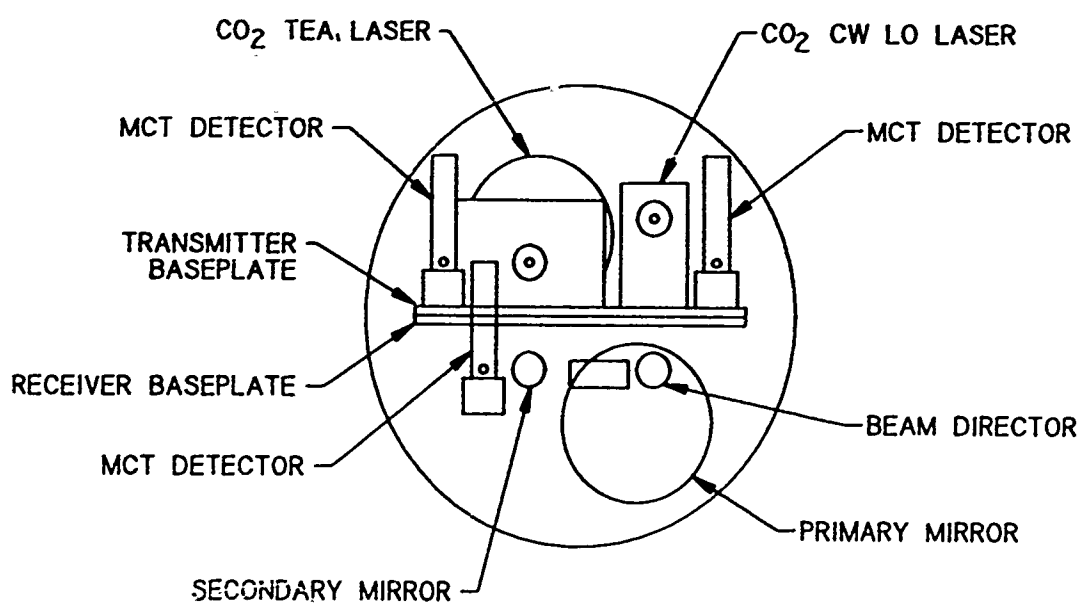


Figure 3. Chamber mounting of lidar system.

detection is the coherent addition of two signals; thus the polarization of the LO signal must be the same as that of the received beam. The polarization of the LO is rotated 90° with respect to its initial direction by reflection so as to match that of the received signal. The two beams mix on a beamsplitter and are then focused by a lens onto the HgCdTe detector.

2.1 Heterodyne Detection

Heterodyne detection is a signal (or shot) noise limited technique which removes the detector noise as a measurement limit. The essence of the technique is to coherently mix the received signal with a local oscillator reference signal slightly shifted in frequency and constant in phase. The difference frequency term ($\omega_s - \omega_{LO}$) generated by the coherent summation is the signal of interest. This signal is within the 100 MHz bandwidth of the IR detector. If the LO reference power is much larger than that of the received signal, the ideal result is a shot noise-limited measurement of power incident on the detector. The expression for the power signal-to-noise is given by

$$SNR_{pow} = \frac{\eta P_s}{h\nu B}, \quad (1)$$

where P_s is the power from the received signal, η equals the number of photoelectrons created per photon, B is the bandwidth of the detector, and $h\nu$ is the energy of photon from the received signal. An expression for the signal-to-noise is derived in Section 3.3.

2.2 Transmit/Receive Switch

The transmit-receive switch (T/R) consists of a quarter-wave plate and a Brewster window. These two components are used to separate the transmitted and received signals.

The operation of the T/R switch is as follows: The TEA laser beam is p-polarized with respect to the Brewster window and is therefore transmitted to the quarter-wave plate. The quarter-wave plate converts the linear polarization into circularly polarized light. This light is scattered from the atmosphere and the backscattered component is detected. The backscattered

radiation is circularly polarized in the opposite direction and is incident on the quarter-wave plate where it is converted into linearly polarized light. The received beam is now s-polarized with respect to the Brewster window and thus is separated from the transmitted beam by reflection.

3.0 SIMULATION OF A COHERENT LIDAR RETURN SIGNAL

To support the design of the coherent lidar signal-processing electronics, a computer simulation of the lidar backscatter signals was performed. The objective of these simulations was to investigate the operation of an envelope detector for both high and low level backscatter signals. The simulation used the actual CO₂ laser operational specifications to compute atmospheric backscatter return signals. The extension of these simulations to include Doppler shifted return signals is discussed.

3.1 Introduction

Consider an outgoing pulse, with a given pulse profile, basic frequency, and chirp, as shown in Fig. 4. Here the ordinate is the E-field amplitude, not the power. The oscillations depicted are shown at the 40 MHz heterodyne frequency for purpose of clarity. This wave packet propagates out into the atmosphere, and some of it is backscattered via the inhomogeneities in the aerosol scatterers. To compute the backscattered signal, decompose this packet into a sum of plane waves:

$$A(k) = \int E_o(x,0)e^{-jkr} dx, \quad (2)$$

where E_o(x,0) is the E-field at t=0 (just after the pulse leaves the laser). The pulse, as a function of space and time (with no scattering) is given by

$$E(x,t) = \int_{-\infty}^{\infty} A(k) e^{jkr-j\omega t} dk, \quad (3)$$

where $\omega = ck$.

This formalism represents the full time-dependent, moving, wave packet. Figure 5 depicts A(k) computed from the wave form shown in Fig. 4.

First, we compute the return scattered signal from each plane wave. We neglect (for this initial discussion) atmospheric attenuation, 1/r² dilution effects, changes in atmospheric density

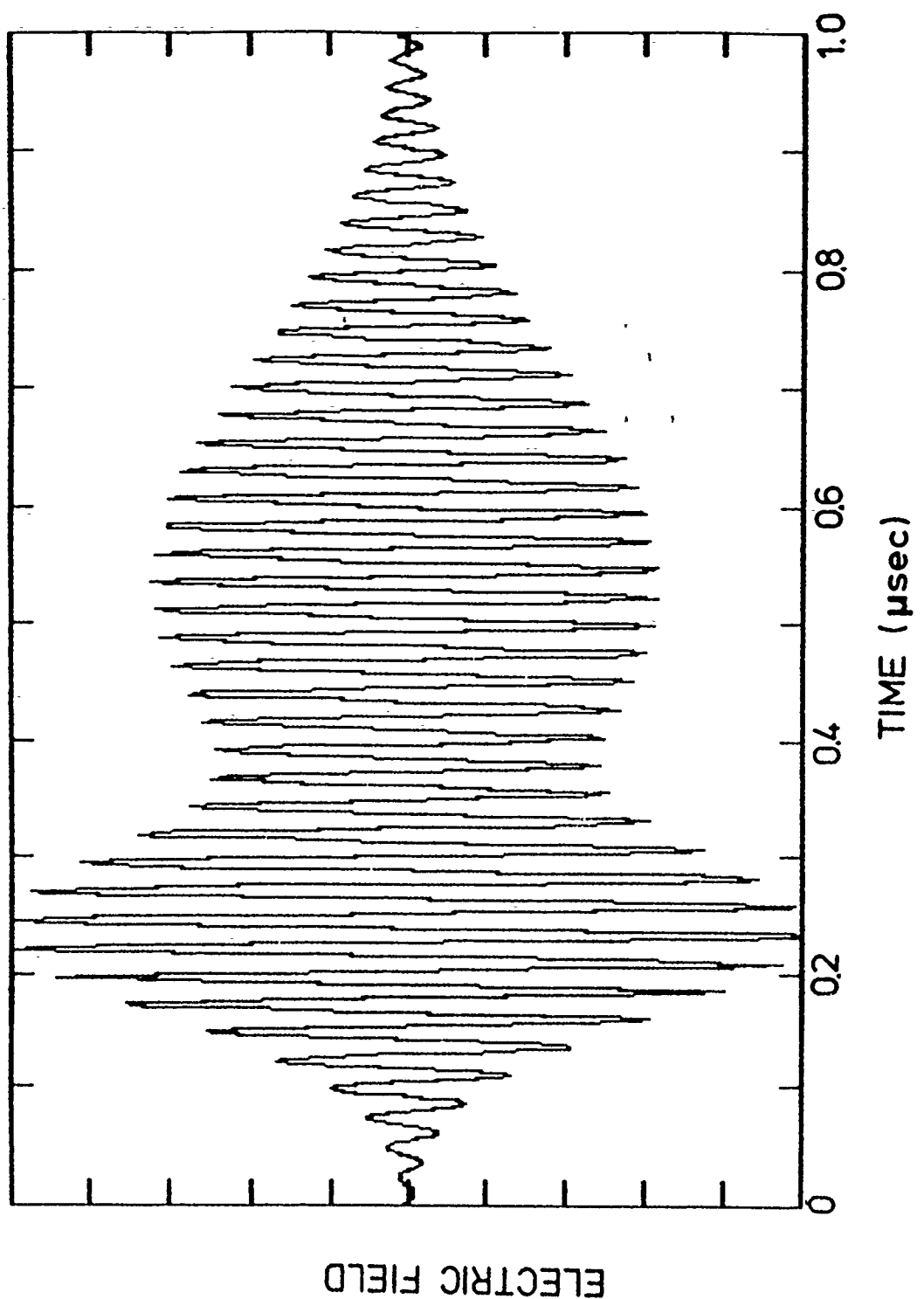


Figure 4. Laser pulse.

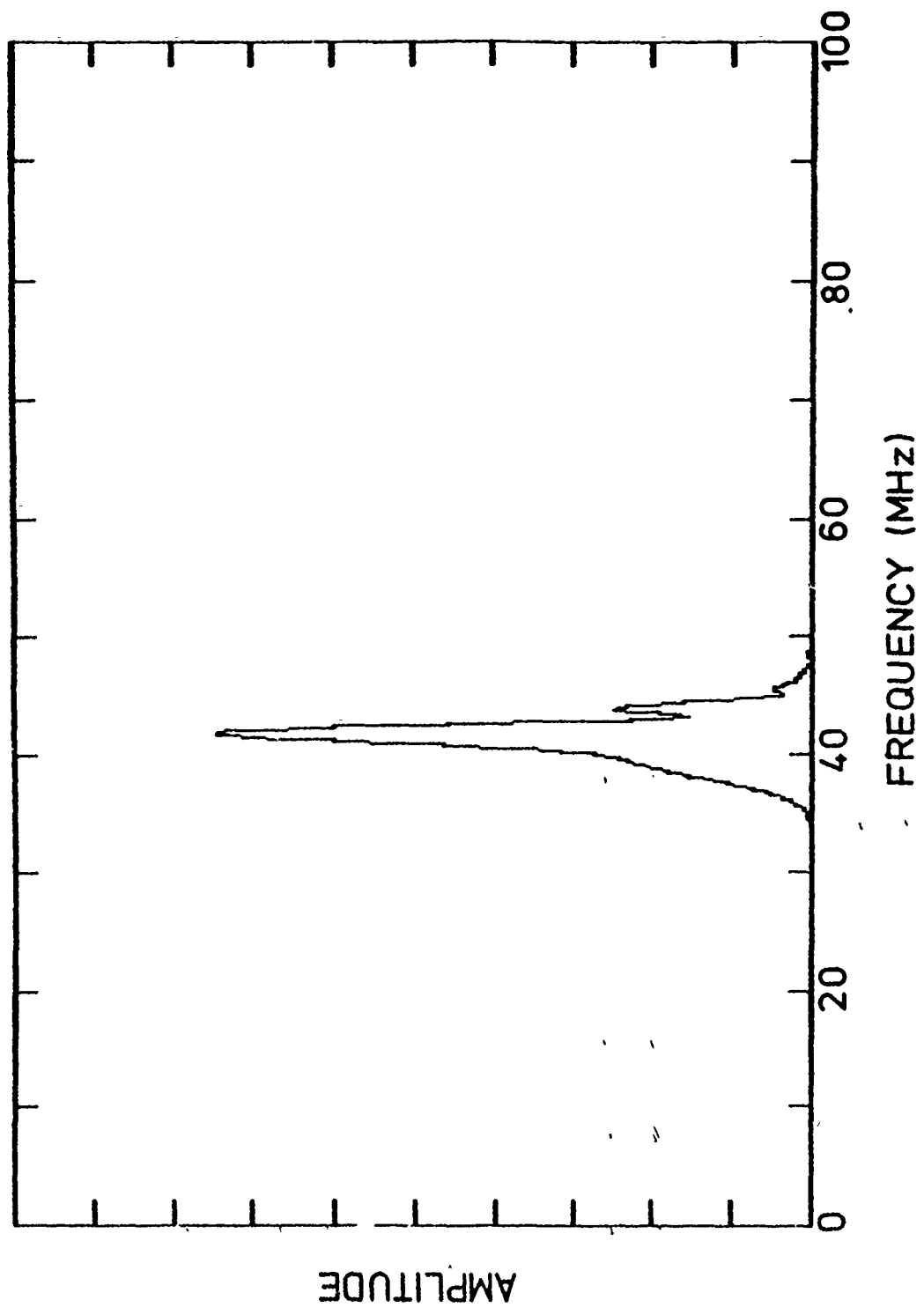


Figure 5. Fourier transform of laser pulse.

with distance, etc. At a frequency k , a wavelet arriving back at the detector and originating from a point x , yields a contribution to the received E-field:

$$\delta E_r(t) \propto N(x)A(k)e^{2jkx-j\omega t} dx dk, \quad (4)$$

where $N(x)$ represents the number density of scatterers along the entire atmospheric path and e^{2jkx} is the phase delay for traveling to x and back.

The total contribution to E_r from all points along the atmospheric path, but still from only the frequency k , is

$$\Delta E_r(t) \propto \int_0^L N(x)A(k)e^{2jkx-j\omega t} dx dk, \quad (5)$$

where the integral 0 to L is over the entire atmospheric path. The total detected E-field from all frequencies is

$$E_r(t) \propto \int_{-\infty}^{\infty} A(k)dk \int_0^L N(x)e^{2jkx-j\omega t} dx, \quad (6)$$

and by making the substitution $\omega = ck$, we find

$$E_r(t) \propto \int_{-\infty}^{\infty} A(k)e^{-jckt} dk \int_0^L N(x)e^{2jkx} dx. \quad (7)$$

Let $\tilde{N}(k)$ be defined as $\int N(x)e^{-2jkx}$. This is the Fourier transform of the density distribution of the scatterers. We then find the following simplified expression for the return signal:

$$E_r(t) \propto \int_{-\infty}^{\infty} dk A(k)\tilde{N}(2k)e^{-jckt}. \quad (8)$$

To the first order, $\bar{N}(2k \neq 0)$ is a constant and is equal to zero for a perfectly uniform density of scatterers. However, for randomly distributed scatterers,

$$\langle N(2k) \rangle = \text{constant for all } k \propto (\text{number of scatterers})^{1/2}$$

with fluctuations such that both the real and imaginary parts are Gaussian distributed; this has the effect of randomizing the phases of $A(k)$!

If $\bar{N}(2k)$ were truly a (non-zero) constant,

$$E_r(t) \propto \int_{-\infty}^{\infty} dk A(k) e^{-jkt} = \int_{-\infty}^{\infty} dk A(k) e^{-jkX}, \quad (9)$$

where X is a dummy variable equal to ct . But this procedure would exactly replicate a reflected image of the outgoing packet!

What has happened is that all the phases which initially conspired to form the outgoing packet have been scrambled by the behavior of $\bar{N}(2k)$. What we get back is a signal that extends from $t=0$ (laser firing) to t_{sum} , the time the pulse takes to traverse the entire atmospheric path and return.

The effect is to create a continuous pulse train made up of quasi-coherent packets that have a "coherence" length about equal to that of the outgoing packet.

3.2 Simulation of Return Signal

3.2.1 No Doppler Shifts; Uniform Atmosphere

Let the data train have a duration T (e.g., 130 μs). We desire a simulation with a temporal resolution τ (e.g., 2 ns).

First, we construct an array of n elements where $n = T/\tau$ (e.g., 65,536 points). Anywhere within this array we then fill in a representation of the output laser pulse with a temporal resolution of τ . The rest of the points are set equal to zero. A schematic of the array is shown in Fig. 6. Next, we compute the Fourier transform of this data set. The transform will have the same shape as in Fig. 5 except that the frequency resolution will have been artificially

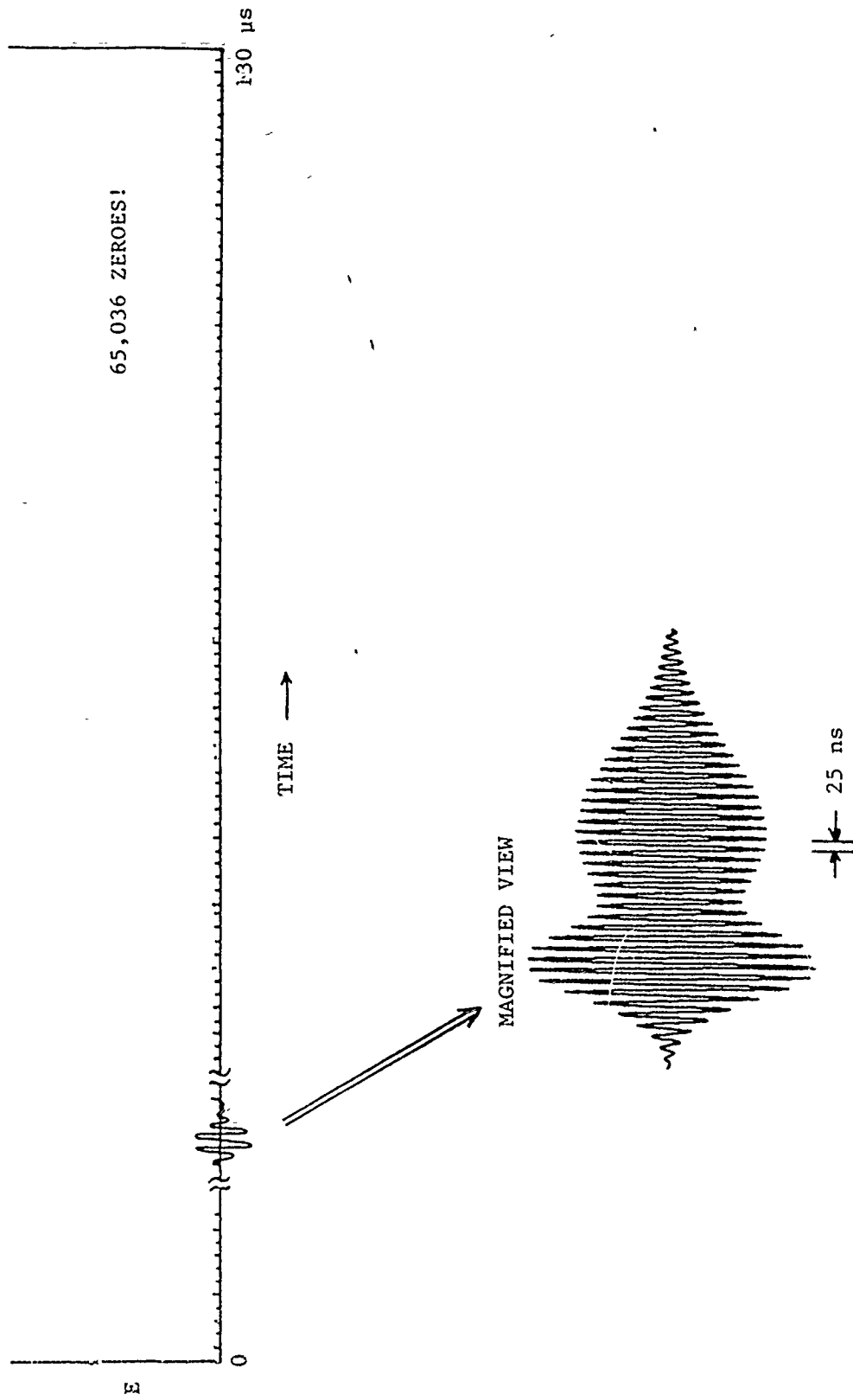


Figure 6. Schematic of lidar shot Fourier transform.

enhanced because of the long array filled with zeros. For each frequency we choose two Gaussian random numbers R_1 and R_2 . We then take each complex $E(k)$ and multiply by these random numbers such that

$$\tilde{E}_r(k) \rightarrow R_1 \tilde{E}_r(k) - R_2 \tilde{E}_i(k),$$

$$E_i(k) \rightarrow R_2 E_r(k) - R_1 E_i(k).$$

An example of what the amplitudes of the transform now look like is shown in Figs. 7 and 8. The largest change, however, is in the scrambling or randomizing of the phases, rather than in adding "noise" to the Fourier amplitudes. Following this procedure, we next inverse Fourier transform the array to find the received E-field amplitude vs. time at the receiver. Three samples of the results from one simulated shot are shown in Fig. 9(a) - 9(c). The appearances of quasi-coherent pulses of duration $\sim 1 \mu\text{s}$ are evident in the simulated return signal.

In order to be able to display the full simulated data set in a convenient way, we pass it through an ideal nonlinear envelope filter similar to one that would be used on the first flight of the CO₂ lidar payload. The circuit is shown schematically in Fig. 10. A sample of the results from applying the mathematical analog of this circuit to the simulated data train is shown in Fig. 11. The high-frequency "sawtooth" features evident in Fig. 11 can be filtered with a low pass filter with a roll-off frequency of 5 MHz, similar to what might be utilized in the actual experiment. The results of the application of such a filter to the data in Fig. 11 are shown in Fig. 12.

The entire simulated and processed data train can now be represented by plotting every 16th point (corresponding to 32 ns intervals). As this is smaller than the typical coherence length in the return signal, virtually no information concerning the density of backscatterers as a function of distance will be lost in the process. The results for the backscatter amplitude as a function of time for one complete laser shot are shown in Fig. 13. Each amplitude corresponds to only a five meter segment of the atmosphere. The same results, except averaged over 0.5 μs intervals, are shown in Fig. 14.

We next computed a distribution of the backscatter amplitudes for a complete laser shot as follows. We recorded the output of the simulated envelope detector and smoothing filter for every 2 ns interval. Figure 15 shows a distribution of the 65,536 amplitudes for one simulated laser shot. A similar distribution for a second simulated shot is shown in Fig. 16 to help assess

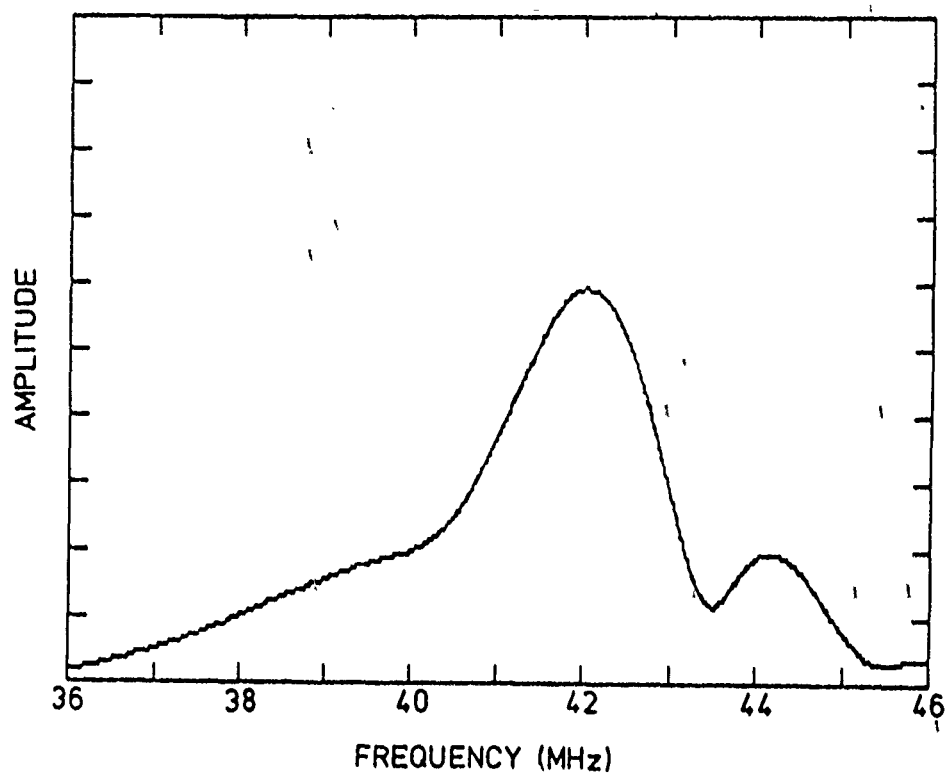


Figure 7. Fourier transform of laser pulse.

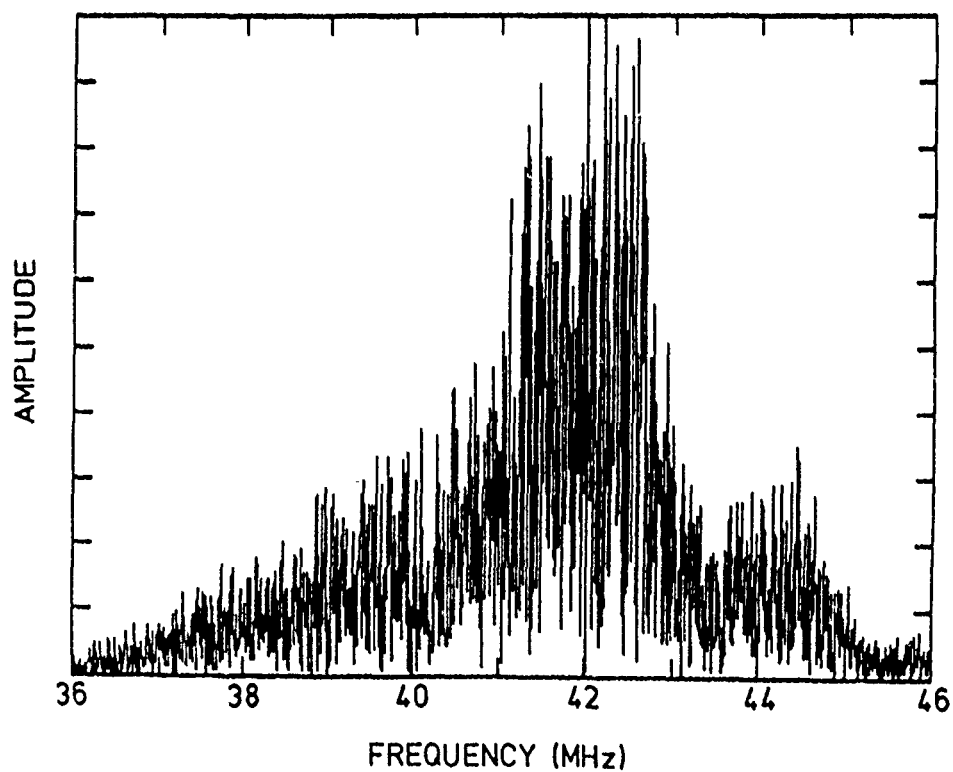


Figure 8. Random phases and amplitudes.

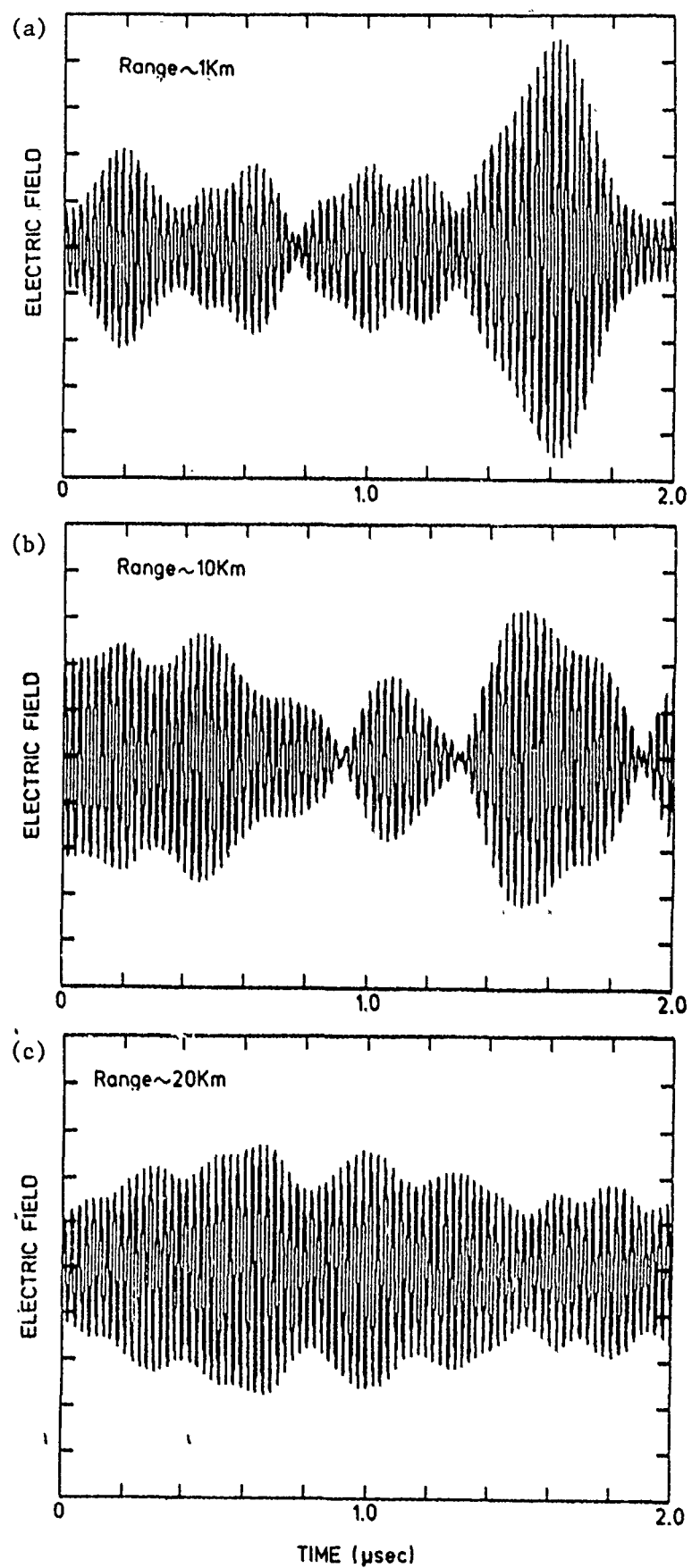
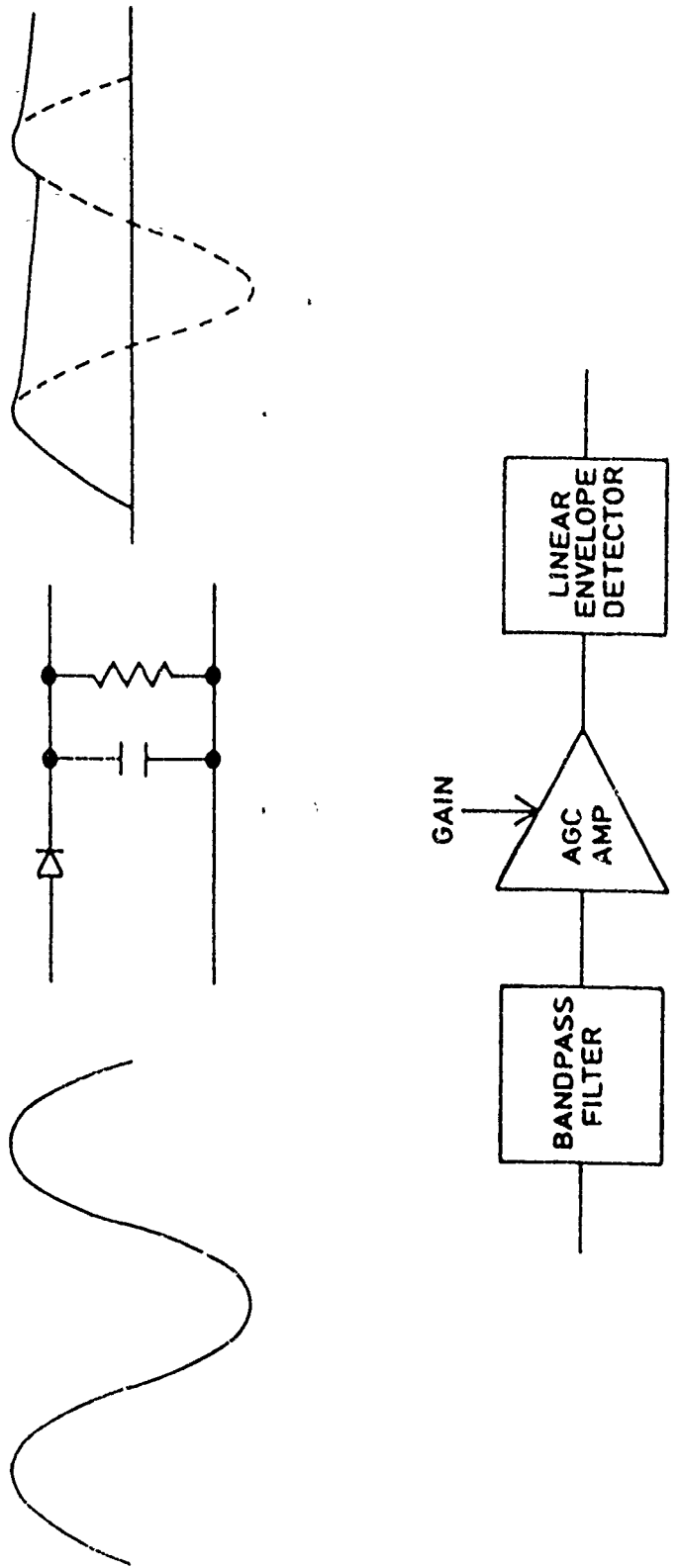


Figure 9. Return lidar signals.



RHG ELECTRONICS
EVT SERIES LINEAR IF AMPLIFIER

Figure 10. Envelope detector.

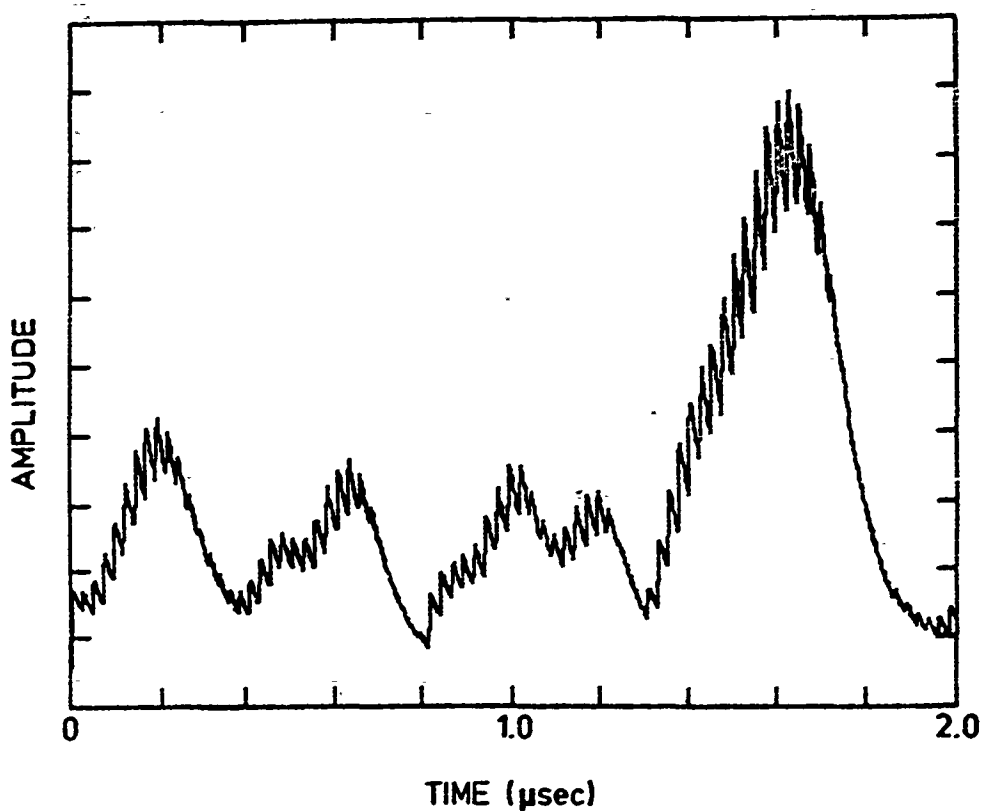


Figure 11. Output of envelope circuit.

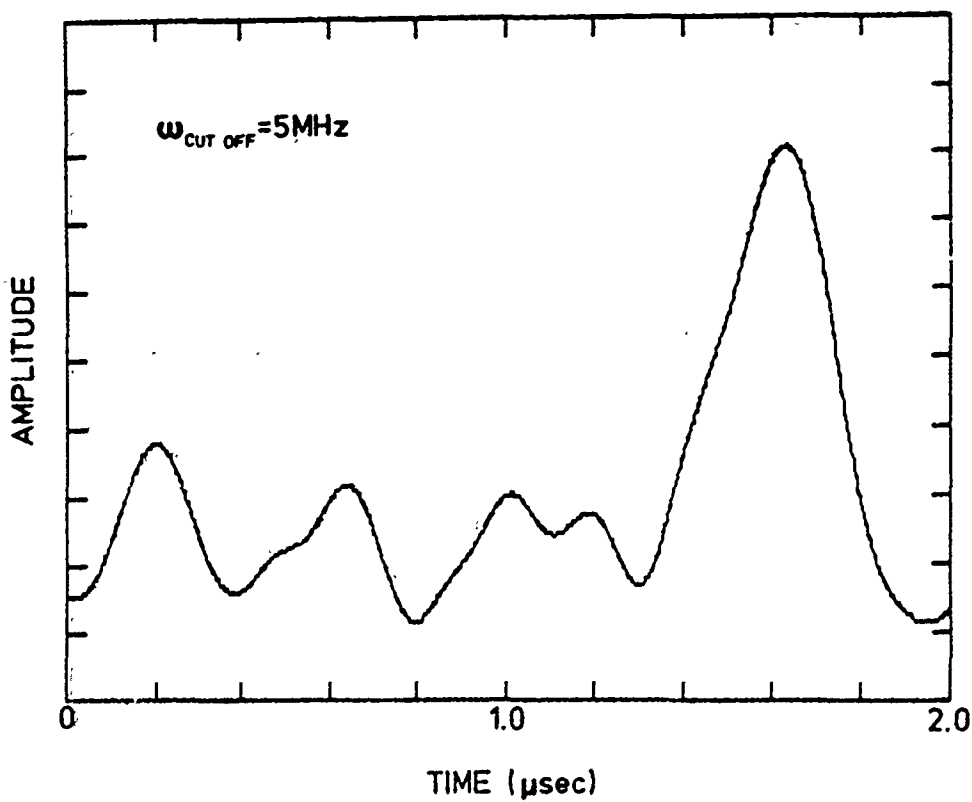


Figure 12. Output of low-pass filter.

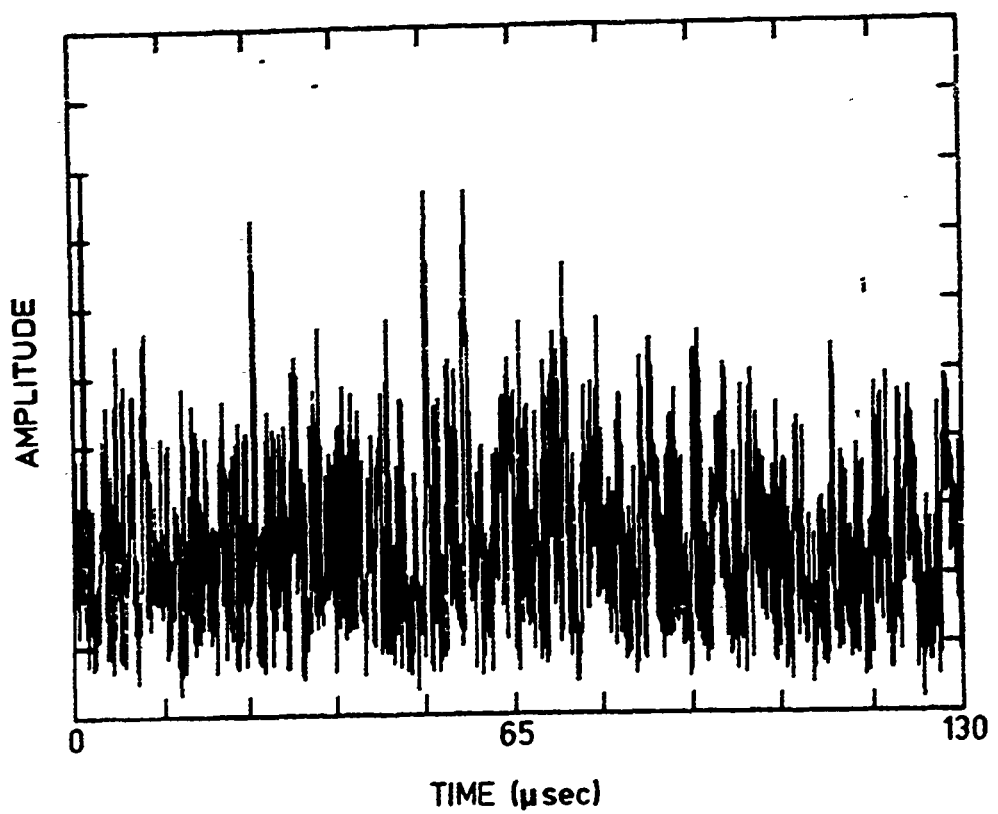


Figure 13. Filtered return lidar shot, 0.03 μ s bins.

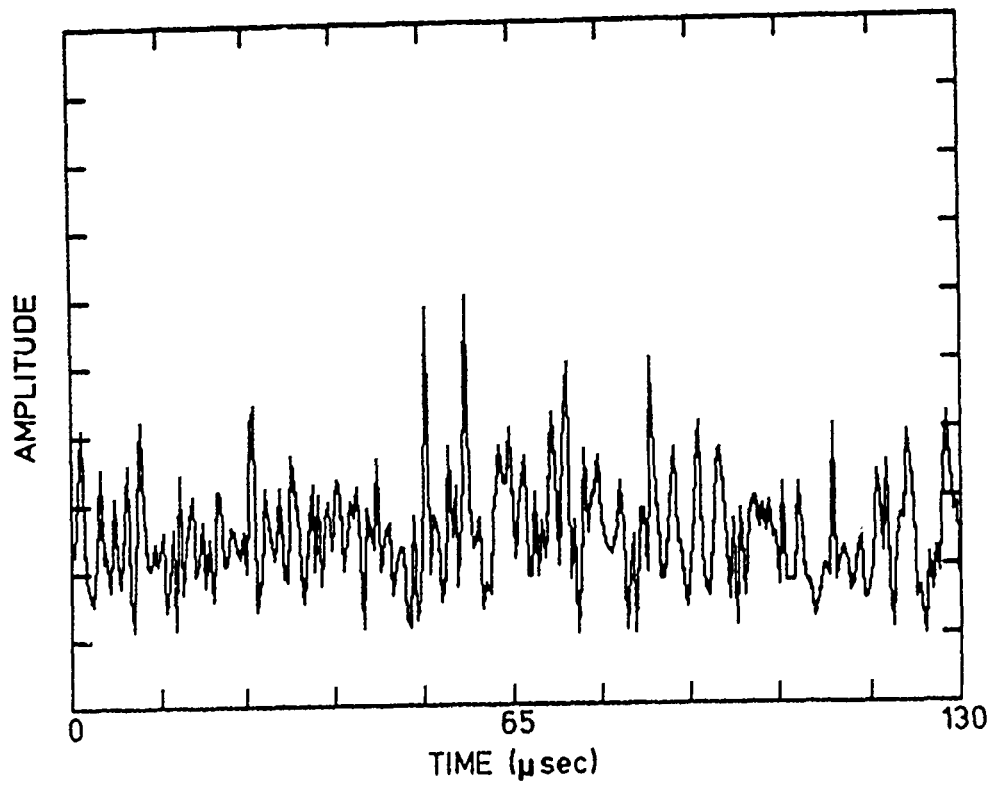


Figure 14. Filtered return lidar shot, 0.5 μ s bins.

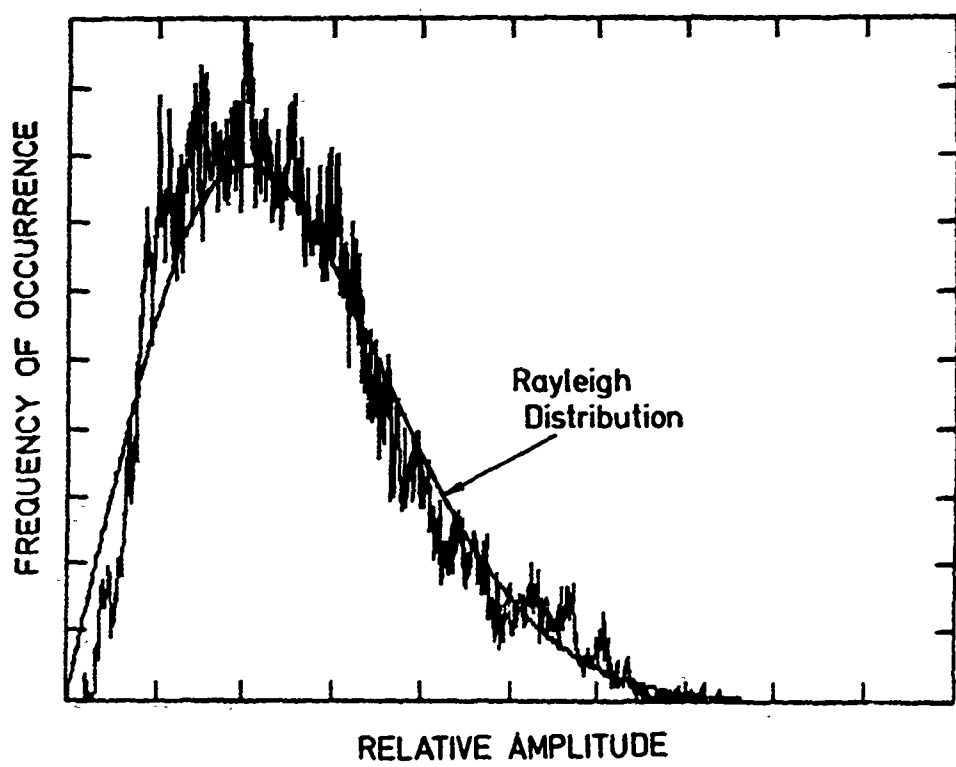


Figure 15. Amplitude Distribution in return shot #1.

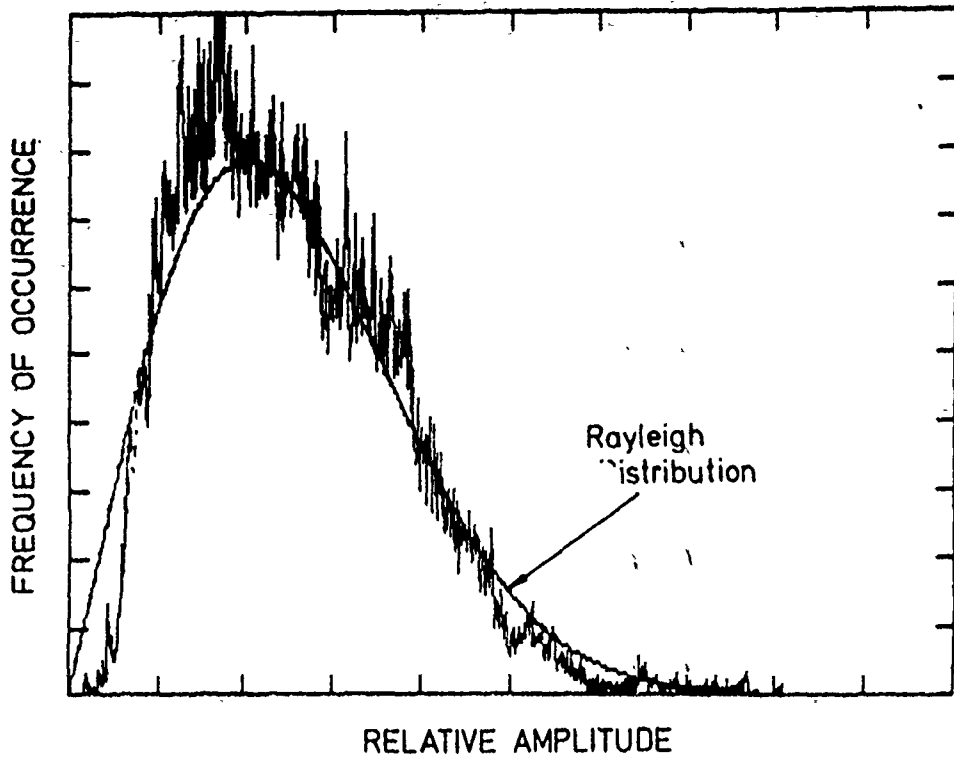


Figure 16. Amplitude Distribution in return shot #2.

which features are significant and which are statistical fluctuations. It is worth noting that even though there are 65,536 entries in the histogram, the statistical precision of these distributions is determined by only a few hundred independent (uncorrelated) points (i.e., the shot time coherence time). For the case where the amplitudes could be measured by an ideal and linear circuit (the one shown in Figure 10 is not), the distributions shown in Figures 15 and 16 should be well represented by a Rayleigh distribution of the form

$$p(E) = \frac{2E}{E_o^2} e^{-E^2/E_o^2}, \quad (11)$$

where the mean amplitude is $\sqrt{\pi}A_o/2$ and the rms width is $(1-\pi/4)^{1/2}A_o$.

Superposed on Figs. 15 and 16 we have graphed the appropriate Rayleigh distribution for comparison. The fit is quite good, except for very small amplitudes where we believe that the envelope detector may be slightly distorting the linearity of the detection process. With this information, we can now simulate the results that would be obtained by summing many shots (see also Sec. 3.2.2 below). Instead of going through the entire simulation procedure described above, we can simply utilize the statistical properties of a Rayleigh distribution to help understand the improvement in statistical precision that is to be gained by summing shots.

3.2.2 Nonuniform Atmosphere, Photon Statistics, Pulse-to-Pulse Variations

The simulated return signal from an "ideal" atmosphere discussed above can be easily transformed to simulate other effects. For example, the actual signal will tend to fall off like d^2 , where d is the distance from the laser. Furthermore, the density and composition of aerosol scatterers will be nonuniform throughout the atmosphere. As long as both of these effects lead to changes in the return signal that vary on time scales that are very long compared to the coherence length, they can be put in "by hand", i.e., by multiplying the simulated data with a slowly varying function that represents the density variations or d^2 dilution effects.

Where photon statistics are quite adequate, the dominant source of noise will be typical of the fluctuations illustrated in Figs. 13 and 14. The photon statistics in the return signal can be

estimated simply from the standard (incoherent) lidar equation. For regions of the atmosphere or for other conditions where photon counting statistics may become important, these can be incorporated into the coherent simulations in the manner described below.

There are two ways to simulate the effects of detecting and adding laser shots. The most straightforward is to simulate directly a large number of shots. For a reasonable number, e.g., 10-100, this can easily be carried out, while for large numbers the process becomes time consuming and unnecessary. The statistical distribution of the detected amplitudes can be well established by simulating relatively few laser shots (see Figs. 15 and 16). Once this distribution has been established, all further statistical questions can be answered using the distribution rather than by simulating more shots.

The current driven by an electromagnetic wave incident on a detector of area A and quantum efficiency η is

$$I(t) = \frac{eCA\eta}{4\pi} E^2(t), \quad (12)$$

where $E(t)$ is the magnitude of the electric field. The E-field incident on a coherent lidar detector is

$$E(t) = E_{LO}\cos(\omega_{LO}t) + E_{rs}\cos(\omega_{rs}t),$$

where the subscripts LO and rs represent the local oscillator and return scattered signal, respectively. Thus, the current driven in the detector can be written as

$$\begin{aligned} I(t) = & \frac{eCA\eta}{4\pi} [E_{LO}^2\cos^2(\omega_{LO}t) + E_{rs}^2\cos^2(\omega_{rs}t) + 1/2 E_{rs}E_{LO}\cos(\omega_{LO} + \omega_{rs})t \\ & + 1/2 E_{rs}E_{LO}\cos(\omega_{LO} - \omega_{rs})t]. \end{aligned} \quad (14)$$

Since $\omega_{LO} \sim \omega_{rs}$, the first three terms have a frequency approximately twice that of the laser radiation and contribute to an essentially dc current and its associated noise term. The last term represents the detectable ac signal, which is given by

$$I_{sig}(t) = \frac{eCA\eta}{8\pi} E_{LO} E_{rs} \cos(\omega_{LO} - \omega_{rs})t. \quad (15)$$

For convenience, we compute the number of electrons, N_{LO} , that are moved through the detector by the local oscillator signal in a time Δt where $\omega_{LO} - \omega_{rs} << \Delta t^{-1} << \omega_{LO}$:

$$N_{LO} = \frac{CA\eta}{8\pi} E_{LO}^2 \Delta t. \quad (16)$$

Similarly, the corresponding number of electrons associated with only the returned scattered signal is

$$N_{rs} = \frac{CA\eta}{8\pi} E_{rs}^2 \Delta t. \quad (17)$$

With these expressions we can rewrite Eq. (15) as follows:

$$N_{sig}(t) = \frac{CA\eta}{8\pi} \left[\frac{8\pi N_{rs}}{CA\eta \Delta t} \right]^{1/2} \left[\frac{8\pi \eta_{LO}}{CA\eta \Delta t} \right] \cos(\omega_{LO} - \omega_{rs})t \Delta t \quad (18)$$

$$N_{sig}(t) = N_{rs}^{1/2} N_{LO}^{1/2} \cos(\omega_{LO} - \omega_{rs})t.$$

In our simulation of the lidar return signal (see Sec. 3.2) we find that the signal is quasi-sinusoidal as in Eq. (18) only for a correlation time ($\leq 0.5 \mu s$), and that the amplitude varies dramatically (with a Rayleigh distribution; see Figs. 15 and 16) during the course of the return signal.

Let the mean amplitude in the coherent simulation be A_0 and the instantaneous signal be $A(t)$. We then utilize the results of our simulation of the incoherent return signal via the basic lidar

equation, i.e., the number of backscattered photons detected as a function of time (reference Sec. 3.2). The latter calculation directly yields the average value of the quantity N_{rs} defined in Eq. (17).

To simulate the photon counting statistics we utilize the numbers N_{sig} and N_{LO} , where N_{sig} is given by

$$N_{sig}(t) = N_{rs}^{1/2} N_{LO}^{1/2} \frac{A(t)}{A_o}, \quad (19)$$

and where N_{LO} is dependent on the strength of the local oscillator. Here, N_{sig} is the number of electrons (in time Δt) associated with the oscillating signal and N_{LO} is the number of electrons (in time Δt) associated with the dc noise level, which we take to be dominated by the local oscillator. Note that the signal-to-noise ratio is:

$$SNR = N_{rs}^{1/2} \frac{A(t)}{A_o}, \quad (20)$$

which is independent of the local oscillator intensity. From this result, we see that if a total of N_{rs} photons are detected in a longer interval (long compared to the $A(t)$ oscillations, then the signal-to-noise ratio is $1/2 N_{rs}^{1/2}$, the factor of $1/2$ representing the rms variations in $A(t)$.

To compute the simulated number of electrons that are detected in an interval of width Δt , we use a random number generator to choose the actual number of electrons N_e from a Poisson distribution (or Gaussian distribution where appropriate) whose mean is $N_{sig}(t) + N_{LO}$. The following simple example will illustrate this procedure. Let $N_{rs} = 100$ (mean number of scattered photons detected in a time Δt , according to simulations via the basic lidar equation) and $N_{LO} = 10^4$ (number of electrons driven in the detector by the local oscillator in time Δt). For

$A(t)/A_0 = 1$, we would find from Eq. (19) $N_{\text{sig}} = (100 \times 10^4)^{1/2} = 1000$. The mean number for that time bin would then be $10^4 + 10^3 = 11\,000$, with Gaussian fluctuations of $\sim 105(1\sigma)$. The signal-to-noise ratio for this bin is $1000/(11\,000)^{1/2} \approx 9.5$.

To illustrate specifically what effects photon counting statistics will have on our ability to detect and successfully interpret the return lidar signal, we have carried out the following simulation. We consider a $1\ \mu\text{s}$ segment of the return laser pulse. For the waveform of this segment we could have chosen any portion of the simulated return signals, such as those illustrated in Figs. 9(a) - 9(c). However, we simply chose the shape of the outgoing laser pulse as representative of the waveform in the return signal. We also chose, as an illustrative value, a local oscillator strength that would yield 10^5 photons in $1\ \mu\text{s}$ (corresponding to a detected power of only $\sim 10^{-9}$ watts). In practice, the local oscillator would have to have at least 1000 times this power to be able to dominate the thermal noise of the detector; however, since the number of simulated return scattered photons we are using is much smaller than either of these numbers (and there is no thermal noise in the simulation), the resultant signal-to-noise will be the same as if we had used a larger value of N_{LO} .

To implement the simulations, we first chose a value for the total number of return scattered photons (values ranging from 4×10^4 to 100). At each of 512 points in the simulated return signal, we assigned a number of electrons that were moved through the detector according to the prescription described earlier in the text. Once the data were simulated, a Fourier transform was carried out to inspect the frequency content in the signal. The results are shown in Figs. 17-22 where the number of scattered photons has been systematically reduced from the high signal-to-noise regime to the point where the signal can no longer be detected. We find, as expected, the point where the signal can no longer be detected, and that with as few as ~ 100 photons, the signal can not only be detected, but the centroid of the (heterodyne) frequency distribution can be determined to an accuracy of $\sim 0.4\ \text{MHz}$; this corresponds to a Doppler velocity of 5 mph (7.3 km/h).

We have also carried out a preliminary study of the effects of photon counting statistics on the behavior of an envelope detector (Fig. 10). The simulations of the response of the envelope detector were carried out in much the same manner as described above for the generation of Figs. 17-22. In the present case, however, the simulated signal with counting statistics was

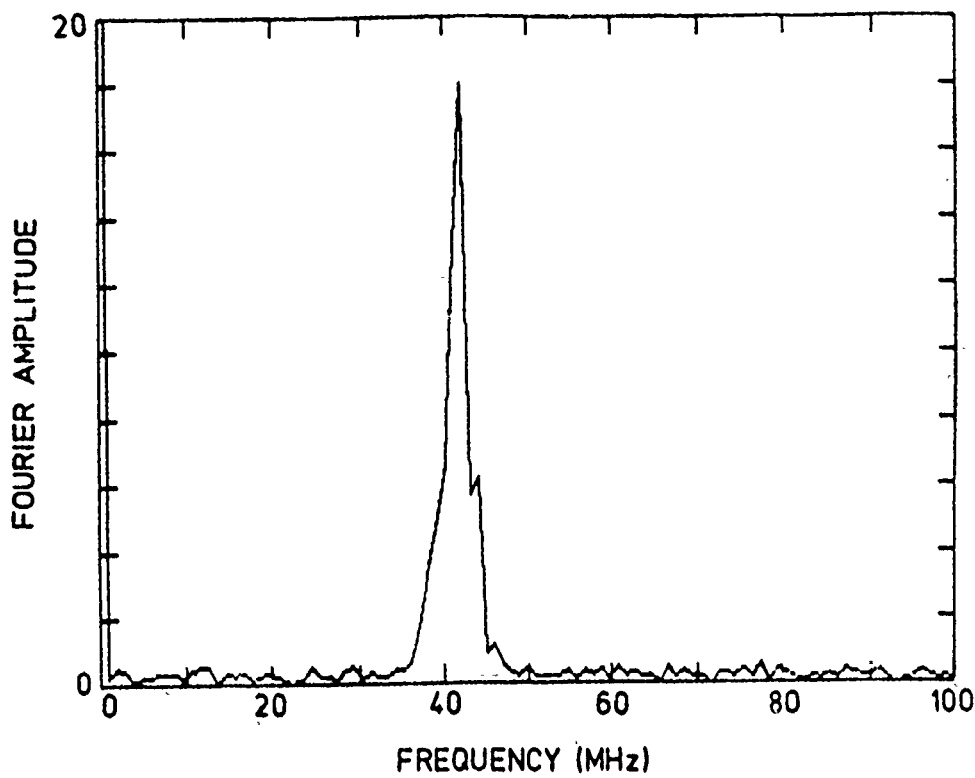


Figure 17. Effects of photon statistics on the detected background signal, $N_{LO} = 10^5$, $N_{RS} = 4 \times 10^4$.

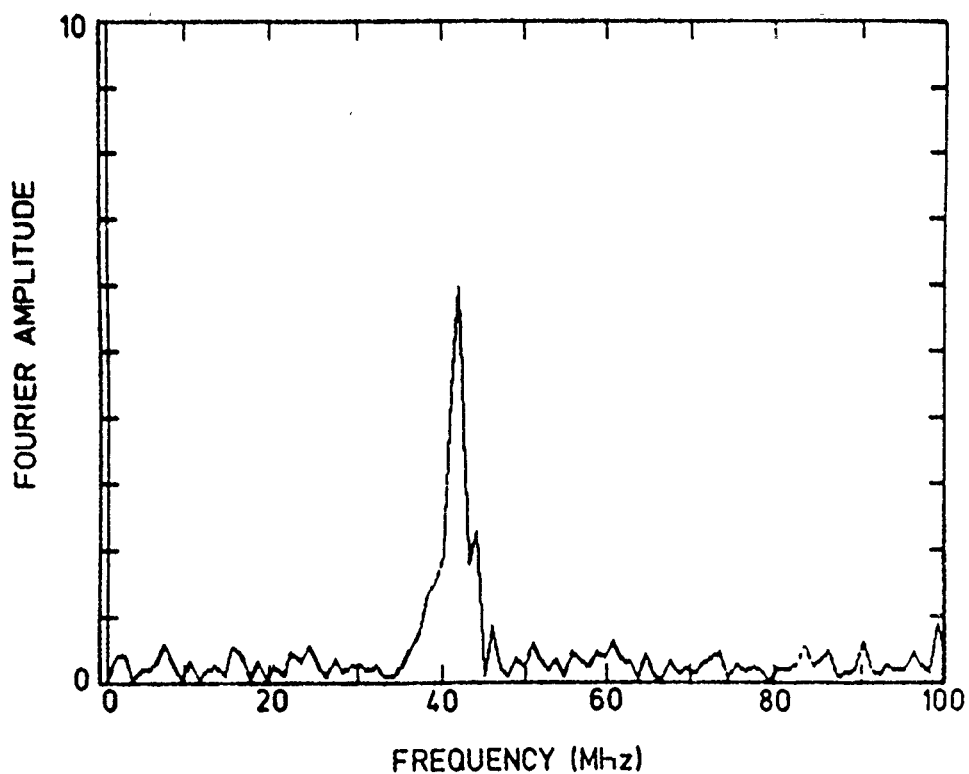


Figure 18. Effects of photon statistics on the detected background signal, $N_{LO} = 10^5$, $N_{RS} = 4000$.

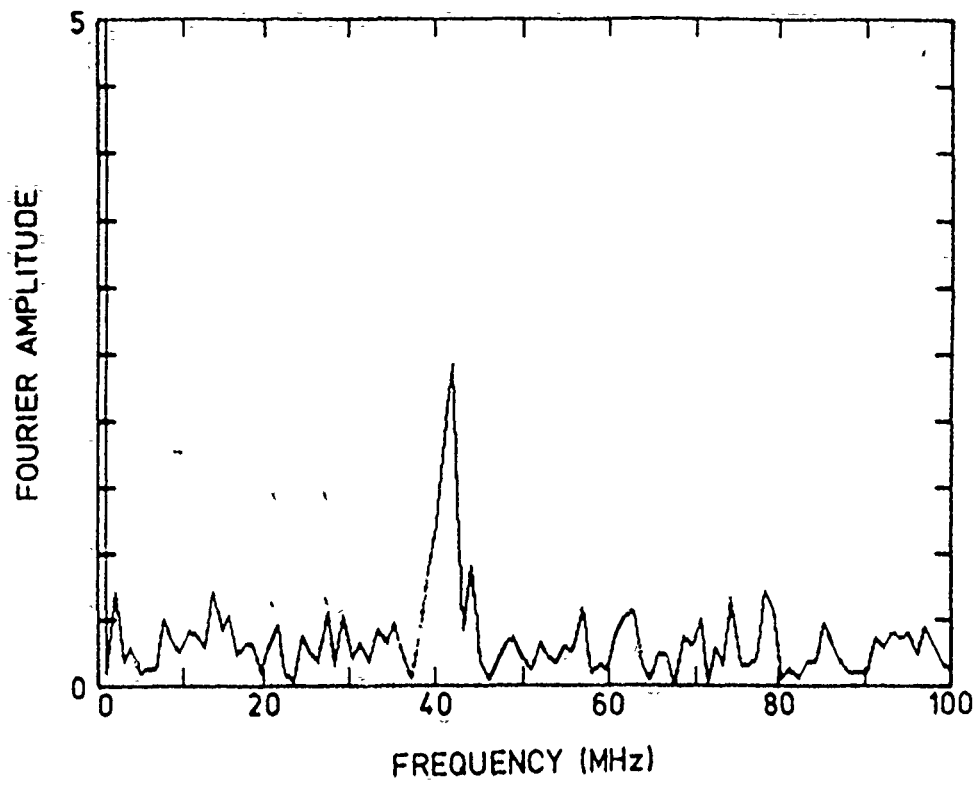


Figure 19. Effects of photon statistics on the detected background signal, $N_{LO} = 10^5$, $N_{RS} = 800$

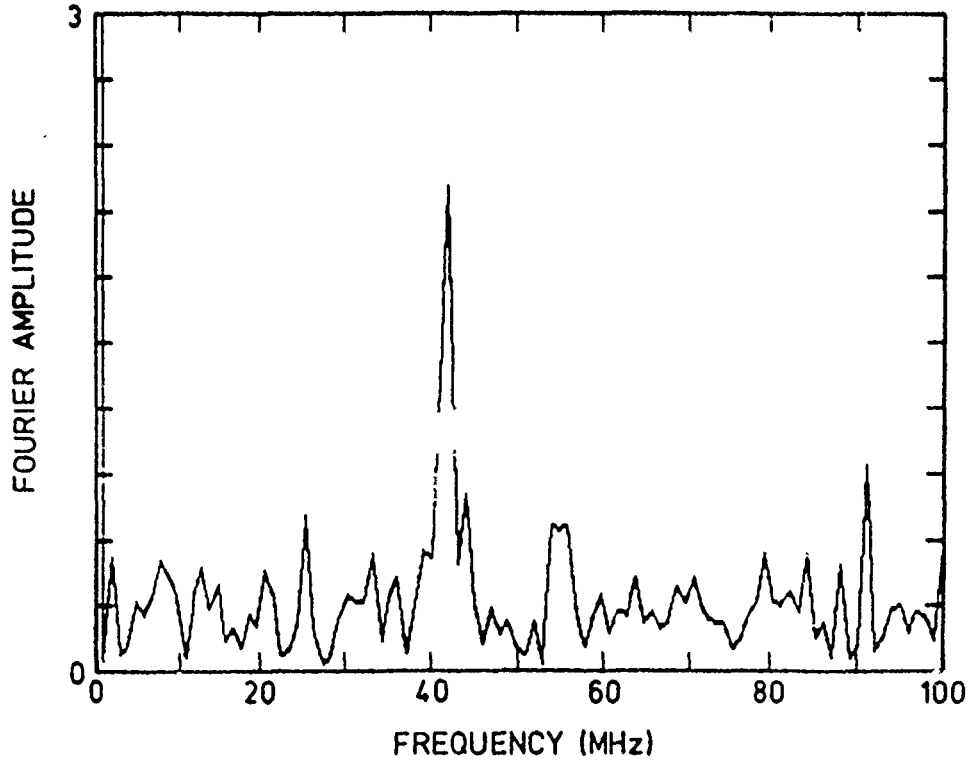


Figure 20. Effects of photon statistics on the detected background signal, $N_{LO} = 10^5$, $N_{RS} = 400$.

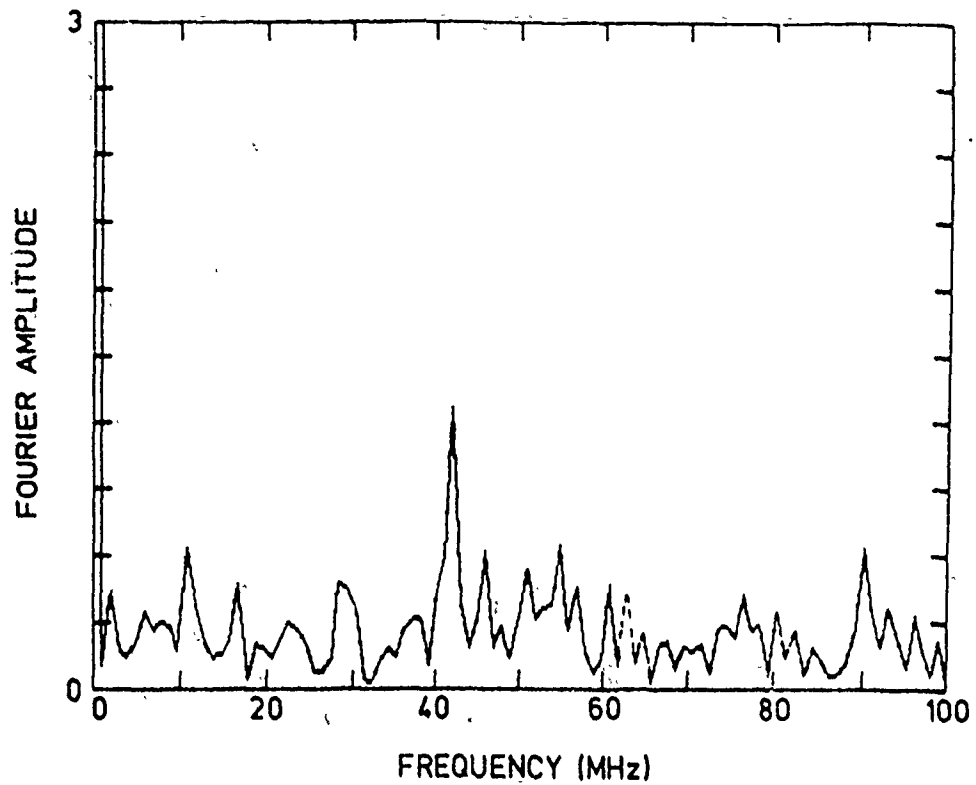


Figure 21. Effects of photon statistics on the detected signal, $N_{LO} = 10^5$, $N_{RS} = 200$.

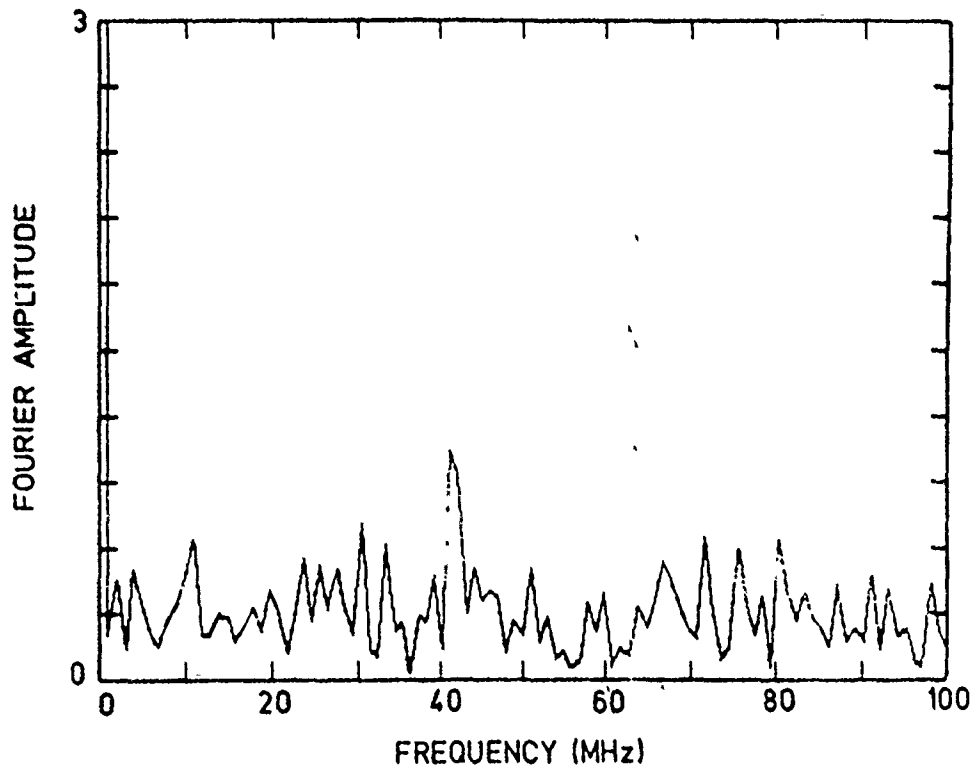


Figure 22. Effects of photon statistics on the detected backscatter signal, $N_{LO} = 10^5$, $N_{RS} = 100$.

passed through a prefilter, an envelope detector, and a low-pass filter. The results are shown in Fig. 23. In this figure we plot the mean amplitude out of the envelope detector (and subsequent low-pass filter) as a function of the number of return scattered photons N_{rs} detected in a ~ 200 ns interval. As Fig. 23 demonstrates, the amplitude is proportional to $N_{rs}^{1/2}$ (see Eq. 19) for $N_{rs} \geq 50$, below which the output of the envelope detector becomes increasingly dominated by noise. This result is similar to that found by simply Fourier-transforming the return signal (Figs. 17-22), thereby demonstrating the effectiveness of the envelope detector.

3.2.3 Doppler Effects Due to Winds

The following briefly describes our present efforts to add Doppler velocity shifts to the simulated coherent lidar shots. We point out, however, that if two conditions are met, it is not necessary to add anything to the present simulations to represent Doppler effects. These conditions are (1) that at each point along the lidar path, there is essentially only a single wind speed to consider (i.e., there are no significant turbulent velocity motions), and (2) the wind speed varies sufficiently slowly along the path that, within one coherence length (~ 100 m), the value of the wind speed can be taken to be essentially a constant. If these conditions are met, Fourier transforms of small segments of lidar data ($\sim 1 \mu\text{s}$ in duration) will all yield the same results (to within statistical accuracy) except for a simple overall constant shift in frequency $\Delta\omega_D$, which is given by

$$\Delta\omega_D = \frac{2\omega_o}{c} V_w, \quad (21)$$

where ω_o is the basic laser frequency and V_w is the wind velocity at that point along the range. Thus, the simulations shown in Figs. 17-22 are still valid except for a shift in the origin. If, however, it becomes desirable to simulate complete shots with wind velocities that vary dramatically with range, then we could use a technique such as the one described below.

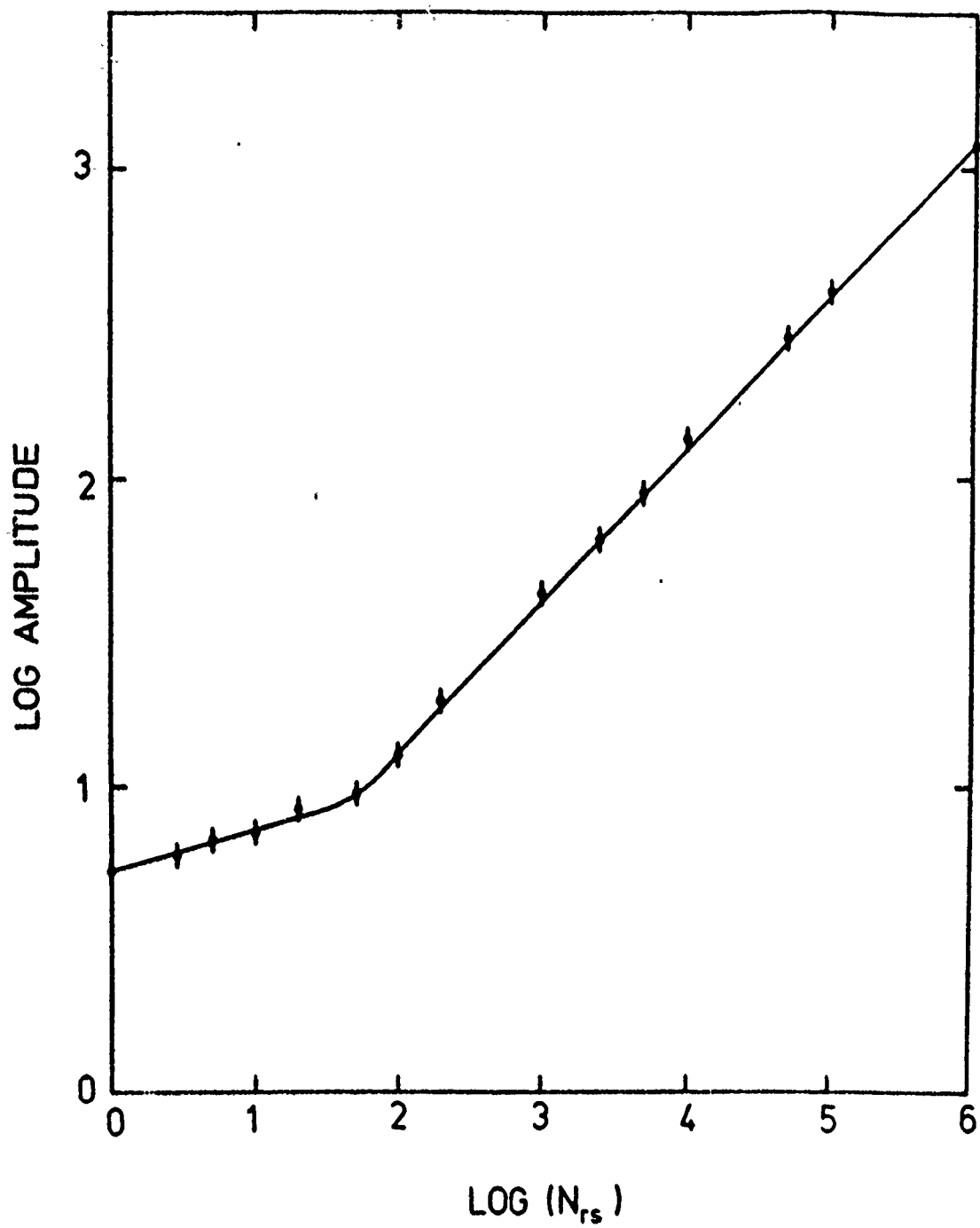


Figure 23. Output vs. input of envelope detector.

Our prescription involves multiplying the simulated return shot (see, e.g., Fig. 9) by a function of the form

$$f(t) = \cos(2\omega_o \int_0^t V_w(t')dt'/c), \quad (22)$$

where ω_o is the basic laser frequency and V_w is the wind velocity as a function of range. The oscillatory frequency of $f(t)$ is defined as

$$\Delta\omega_D = \frac{d\phi}{dt} = \frac{2\omega_o}{c} V_w(t), \quad (23)$$

where ϕ is the argument of the cosine function. If we write the return signal $E_r(t)$ as in Eq. (9),

$$E_r(t) \propto \int A(\omega) e^{j\omega t} d\omega, \quad (24)$$

then we would represent the Doppler-shifted return signal as

$$E_D(t) \propto f(t) \int A(\omega) e^{j\omega t} d\omega, \quad (25)$$

which, if $V_w(t)$ is a slowly varying function, can be written locally (in time) as

$$E_D(t) \propto \cos(\Delta\omega_D t) \times \int A(\omega) e^{j\omega t} d\omega. \quad (26)$$

This equation can be written in the following suggestive form:

$$E_D(t) \propto \int A(\omega) e^{j(\omega + \Delta\omega_D)t} d\omega - i \int A(\omega) e^{j(\omega - \Delta\omega_D)t} d\omega. \quad (27)$$

A Fourier transform of data simulated in this way would yield a spectrum that is shifted both up and down in frequency by an amount $\Delta\omega_b$. The magnitude of the shift in frequency will vary with the range (or return time) according to the input prescription given by the argument of Eq. (22). We have not yet devised an algorithm for producing only a "one-way" Doppler shift that also can be varied in an arbitrary way over the atmospheric path. It is recommended that lidar simulations involving Doppler shifts be continued so as to support actual atmospheric backscatter data analysis.

3.3 Lidar SNR Simulations

A computer model to simulate the atmospheric backscatter signals for a coherent balloonborne CO₂ lidar system was developed. The model is based on a vertically downward looking lidar detector operating at 10.6 μm that measures the coherent backscatter from the different aerosol populations. The system considered has been given the following properties:]

- coaxial transmitter/receiver
- heterodyne detection system
- spatial resolution of 1 km
- incident laser pulse energy of 135 mJ/shot

The efficiencies included in the calculation are:

- heterodyne (mixing of LO and return signal) - 60%
- detector - 30%
- optical transmission and reflection - 53%
- speckle

Calculations of the power signal-to-noise ratio are plotted in Figs. 24 and 25. Figure 24 shows the detected SNR coming from the aerosol populations in the atmosphere at different altitudes. Several curves are plotted corresponding to various altitudes of the balloonborne lidar. The enhancement of the signal in the 0-5 km region is due to the large aerosol population nearer the earth's surface. The enhancement of near field signals is due to the increased solid angle i.e., although fewer photons are scattered back toward the detector compared with signals generated by higher densities of aerosols, more of these photons are detected.

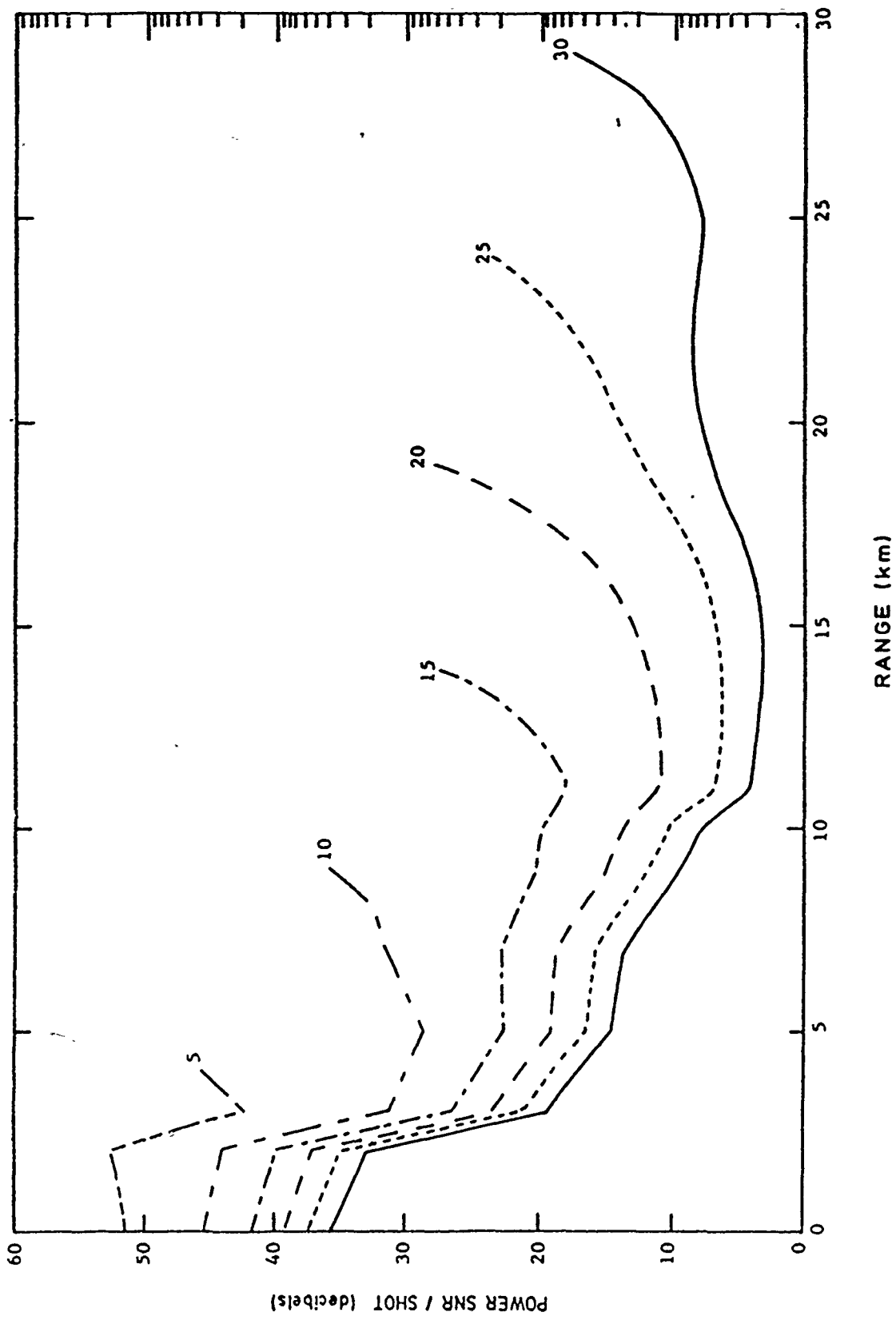


Figure 24. SNR vs. range for various balloon heights.

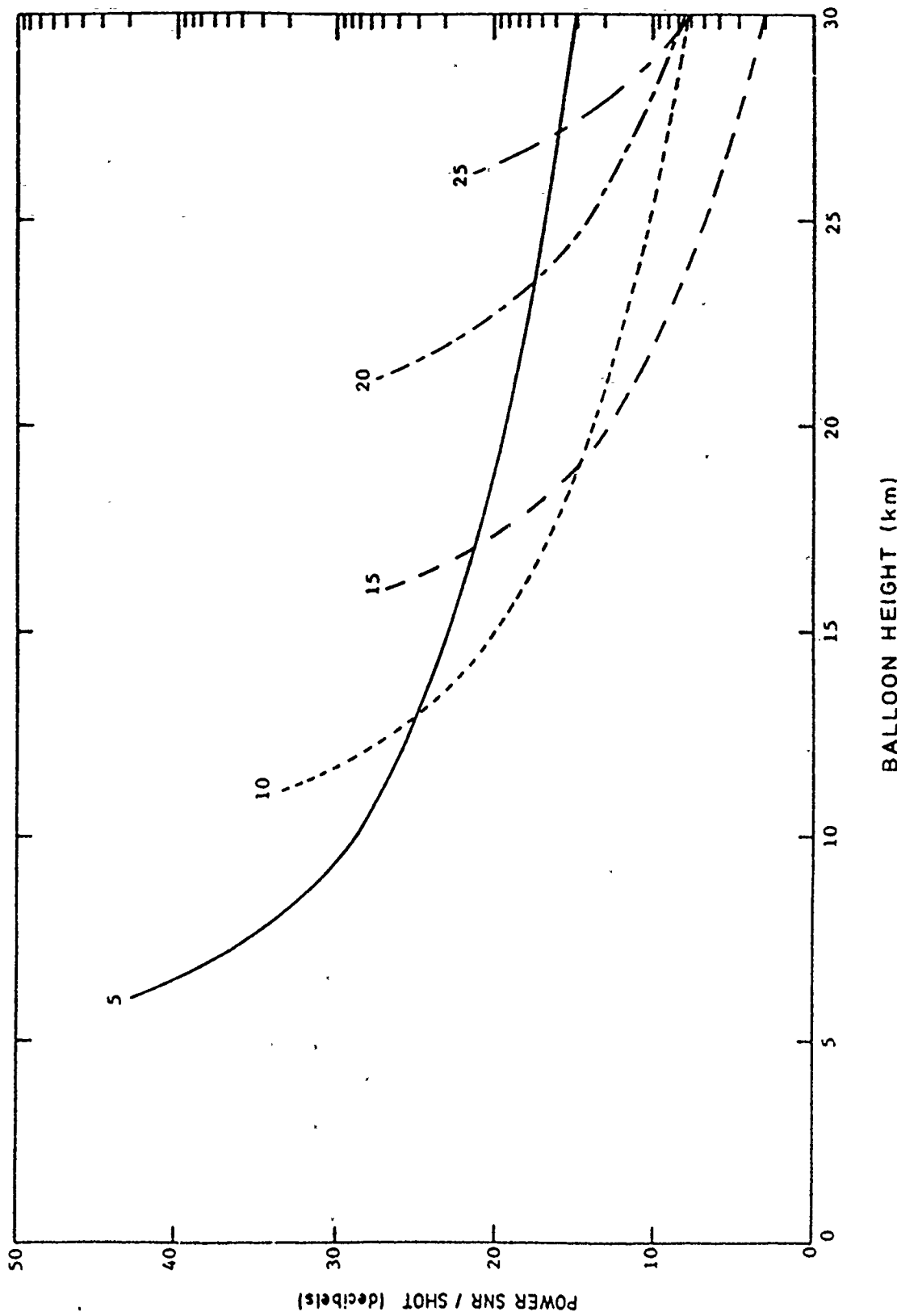


Figure 25. SNR at different altitudes vs. balloon height.

The effect of the solid angle is better displayed in Fig. 25. In this figure the SNR obtained from signals at specific altitudes are calculated for the lidar detector being at different altitudes. This result suggests that the maximum information about certain altitudes will be obtained as the balloon is ascending. As an example, the SNR from 15 km diminishes from a value of 500 to 2 per laser pulse as the balloon ascends from 16 to 30 km.

4.0 LIDAR DESCRIPTION

4.1 CO₂ Laser Description

The laser for the balloonborne 10.6 μm lidar payload was developed by Laser Science, Inc. (LSI) and will be provided as Government Furnished Equipment (GFE). It is a modified version of their Model PRF-150S hybrid CO₂ TEA laser^[3]. Specifications of this laser are given in Table 1, and an outline drawing is shown in Fig. 26. A sketch of the temporal beam output intensity is given in Fig. 27. Modifications have been incorporated which will provide for eight hours of closed cycle operation at a pulse repetition rate of 150 Hz and operation from a power source of 28 Vdc and 50 A.

Water cooling is required in three places: the TEA laser, the CW laser, and the power supply. The operating range of the laser was originally specified at $25 \pm 4^\circ\text{C}$. To increase the range to $\pm 10^\circ\text{C}$, Visidyne, Inc. suggested that LSI replace the invar mounting rods with super invar which has only 1/5 the expansion coefficient. This modification was completed by LSI.

4.2 CO₂ Laser Operation

A frequency-stabilized CO₂ CW laser is mounted on a same laser optics bench to provide the local oscillator (LO) optical frequency reference for pulsed TEA laser. The CW laser output is frequency-shifted by 40 MHz prior to injection into the TEA laser. This shift will provide a 40 MHz frequency difference between the lidar atmospheric backscatter signal and the local oscillator power at the heterodyne detector. The rated output power of the LO CW laser is approximately 50 mw. The local oscillator laser can be adjusted for maximum power output^[4]. An LN₂-cooled HgCdTe detector operated in the heterodyne mode monitors the TEA laser optical pulse mixed with the local oscillator. The signal from this "FAST Detector", when viewed on an oscilloscope, provides verification of TEA laser mode lock and a display of pulse shape. A second HgCdTe detector measures the LO 40 MHz power output. A chopper wheel, synchronized to the laser pulse repetition rate, masks this detector during laser pulsing. A fundamental requirement of the balloonborne lidar data system is that the downlinked PCM data frames be synchronized to laser firing. To enable this to be done, it was required that the

Table 1

Laser Specifications

Physical Specifications:	
Laser Head Weight:	198 lb
Control Cabinet Weight:	250 lb
Auxiliary Cabinet Weight:	150 lb
Line Voltage:	115 V nominal @ 60 Hz
Current:	12 A Maximum
Power Consumption:	1300 W Maximum
Water:	0.25 GPM Minimum at 60 \pm 10°F and 80 psig maximum
Gas Consumption:	0.1 SCFM at 150 pps
Mixture:	CO ₂ ; N ₂ ; He = 1:2:6 CO ₂ : 11% N ₂ : 22% He : Balance
Gain Cell:	gas, same as above vacuum, small mechanical vacuum pump approximately 10 CFM at atmosphere
Functional Characteristics:	
Mode	Circular TEM _{oo}
Divergence	2 mrad
Diameter	8 mm
Repetition Rate:	0 - 150 Hz standard
Energy Per Pulse:	200 mJ Maximum TEM _{oo}
Pulse Length:	200 ns Minimum, depending on gas mixture
Peak Power:	1 MW Maximum
Average Power:	30 W Maximum
Frequency Chirp:	400 kHz at 1.5 atm.
Pulse-to-Pulse Jitter:	Below 2 MHz
Long-Term Drift After Warm-Up:	Below 2 MHz/hr
Line Tunability:	60 CO ₂ lines

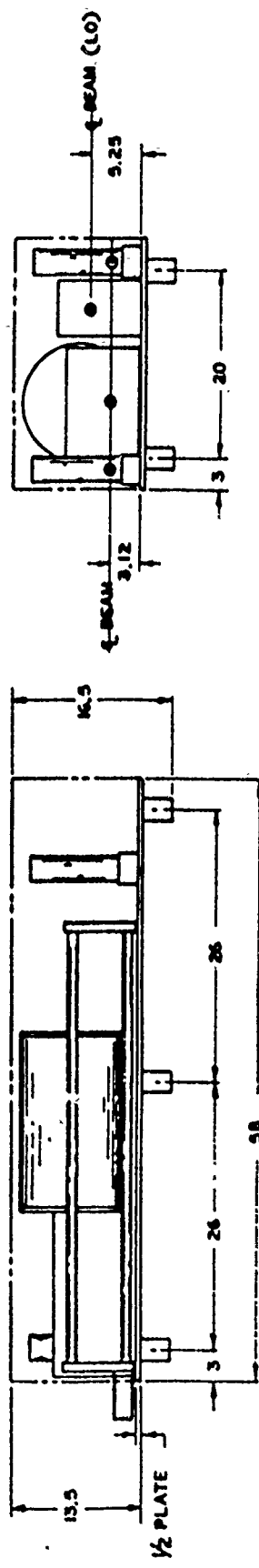
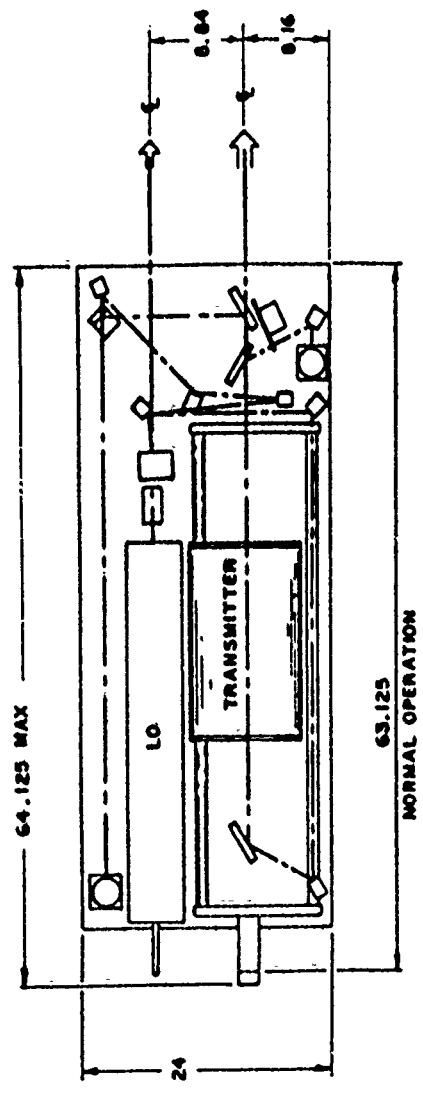


Figure 26. Outline drawing of LSI CO₂ TEA laser.

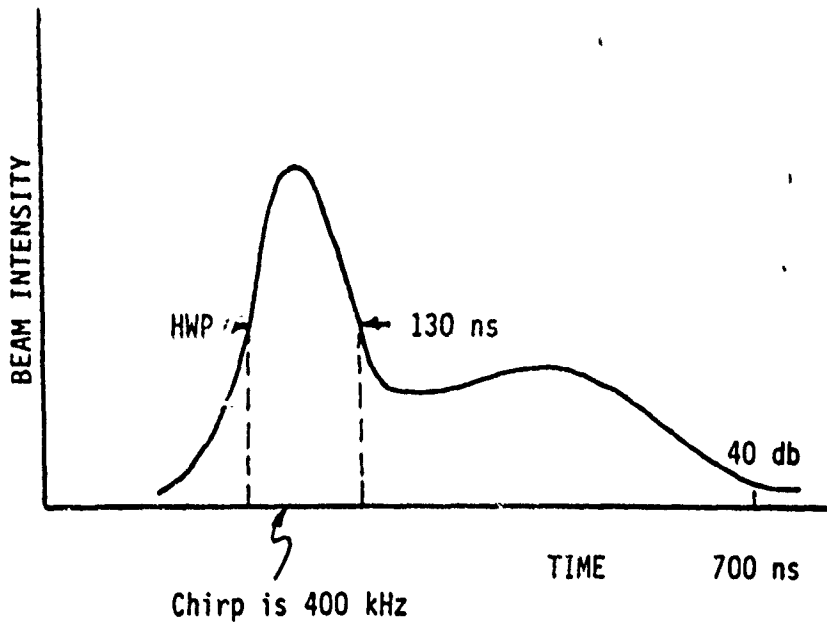


Figure 27. CO₂ laser output pulse.

"SLOW Detector" 100 Hz mechanical chopper be capable of being synchronized with a TTL pulse generated in the lidar data system. This synchronization has been incorporated into the laser.

The LN₂-cooled HgCdTe detectors have dewars with a 12-hour hold time. Provision has been made to enable these dewars to be filled when the laser is installed in the pressure chamber on the balloon payload. The gas mixture required for the gas flow of the TEA laser will be provided by a "lecture" gas bottle with premixed gas. This bottle, when filled to 1500 psi, will provide for 7-1/2 hours of laser operation.

The cooling fluid used for the laser in the laboratory configuration is tap water at a flow rate of 0.25 gal/min. For flight the cooling fluid will be a 60:40 mixture of ethylene glycol and water. This is required to prevent damage to the laser in the case of loss of power during flight which could cause payload temperature to decrease so that water alone would freeze.

To operate the laser remotely in flight, a set of uplinked commands and associated downlinked data monitors will be required. The commands will be to turn on and adjust and align the CW LO laser, and to turn on, align, and mode lock the TEA laser. Other signals to monitor will include the LO power, LO EMT translator voltage, TEA laser injection offset frequency (~ 40 MHz), TEA laser EMT voltage, and TEA laser output power. For ground testing, the wide bandwidth signals of the SLOW Detector and the FAST Detector will be available for oscilloscope display. A He-Ne alignment laser mounted on the laser optical bench will aid in laser/lidar alignment.

To provide a rigid mount between the laser optical bench and the lidar optics, the two systems are mounted back-to-back as shown earlier in Fig. 3.

4.3 Transmit-Receive Switch

4.3.1 Quarter-Wave Plate

The transmit-receive switch (T/R) includes a quarter-wave plate which retards the relative phase of the electric field components by $\pi/2$. This has the effect of converting circularly polarized light into linearly polarized light and converting linearly polarized light into circularly

polarized light. Just as right circular polarization would be converted into a specific linear polarization, left circularly polarized light would be converted into the orthogonal linear polarization.

The sensitivity of the quarter-wave plate to misalignment in the retardation angle and to variations in temperature are given in Table 2. The results in Table 2 are theoretical calculations based on measured parameters from the actual quarter-wave plate. These calculations assume the incident beam is normal to the plate since the quarter-wave plate has little sensitivity to misalignment in the angle of incidence. Results are given for the temperatures 15°C, 25°C, and 35°C and for misalignments between the polarization and the optical orientation of the quarter-wave plate of 0, 1, and 2 degrees. The results are the relative transmissions of the two components of polarization; the numbers in parentheses are the angles with respect to the incident polarization of maximum transmission. If the transmitted wave were perfectly circularly polarized the two components would be 50% each and independent of the angle. In addition, the apparent retardation is also given. Note that the quarter-wave plate is a perfect retarder at a temperature between 25 and 35 degrees Celsius.

Four different samples of quarter-wave waveplates were placed in a CO₂ laser beam operating at 10.6 μm. The four samples were provided by Cleveland Crystal Inc. and were constructed from either cadmium selenide (CdSe) or cadmium sulfide (CdS); each of the two materials were provided with and without antireflection (AR) coatings. CdSe and CdS are both efficient transmitters in the infrared with CdSe being the more efficient of the two. Although CdSe absorbs less energy at 10.6 μm than CdS, unlike CdS it is not transparent in the visible.

These pieces were taken to Laser Science Inc. to be tested with their PRF-150 CO₂ laser, which outputs higher power than the laser purchased for the CO₂ ABLE project.

The laser was operated multimode and the beam was rectangular in shape. The dimensions of the beam were 0.125 inches by 0.250 inches. Three quarters of the energy in the pulse occurs within 500 ns followed by an exponential tail out to 1500 ns. The laser was run at 200 mJ, 100 pps for 60 seconds and 200 mJ, 50 pps for 60 seconds. These correspond to approximate maximum incident energies as follows:

200 mJ: 1.49 MW/cm² pulse

300 mJ: 2.23 MW/cm² pulse

Table 2

CdS $\lambda/4$ -Wave Sensitivities

Misalignment	Temperature (°C)		
	15	25	35
0°	52.4 (0°) 47.6 (90°)	50.7 (0°) 49.3 (90°)	49.0 (0°) 51.0 (90°)
(Retardation)	807.3°	809.2°	811.1°
1°	53.0 (-17°) 47.0 (73°)	51.9 (-33°) 48.1 (57°)	48.0 (31°) 52.0 (121°)
(Retardation)	806.6°	807.9°	812.3°
2°	54.2 (-25°) 45.8 (64°)	53.6 (-37°) 46.4 (53°)	46.4 (39°) 53.6 (129°)
(Retardation)	805.2°	805.9°	814.2°

Results of these tests were the following:

CdS: Both the coated and uncoated samples showed no visible damage on either face of the crystals. A residue of carbon was found on the downstream face of the crystal and as attributed to the burning of markings from a felt tip pen on the slab of aluminum against which the crystals were leaned. The carbon was easily dusted off the sample.

CdSe: The AR-coated piece developed a discolored area immediately at 200 mJ and appeared to worsen at the increased energy. The uncoated piece was fine at 200 mJ but developed a "hot spot" at 300 mJ which left an etched area on both sides of the crystal. The discolored area on the coated piece is suspected to be the crystal burning underneath the AR coating.

It is not understood why the behavior of the crystal with the lower coefficient of absorption was much worse than the other crystal. Many different factors could have contributed, e.g., an unclean sample, damage from previous tests, and therefore no conclusions can be drawn for the CdSe. More importantly, a CdS plate can withstand the energy that will be seen during the actual CO₂ flight in addition to being transparent to a He-Ne laser and is therefore a good choice for a quarter-wave plate.

Based on the above results, the quarter-wave plate procured for the lidar is made from CdS. The transmission efficiency of this device is 98% at 10.6 μm . In addition to its transparency at the IR wavelength, it is also relatively transparent at 6328 Å, which permits a He-Ne laser to be used for alignment.

4.3.2 Brewster Window

The other component making up the T/R switch is a Brewster window. A Brewster window transmits or reflects light depending on its polarization. Specifically, the Brewster window reflects light having an electric field vector in the same plane as the window (s-polarized) and transmits light having an electric field out the plane of the window (p-polarized).

The lidar Brewster window is made from ZnSe, which also is transparent to a He-Ne laser. The efficiencies of the Brewster window are plotted in Figs. 28 and 29. Figure 28 shows the transmissive characteristics of the window and Fig. 29 shows its reflective behavior. At 10.6 μm the transmission efficiency (p-polarized) is 96% and the reflection efficiency (s-polarized) is 99%.

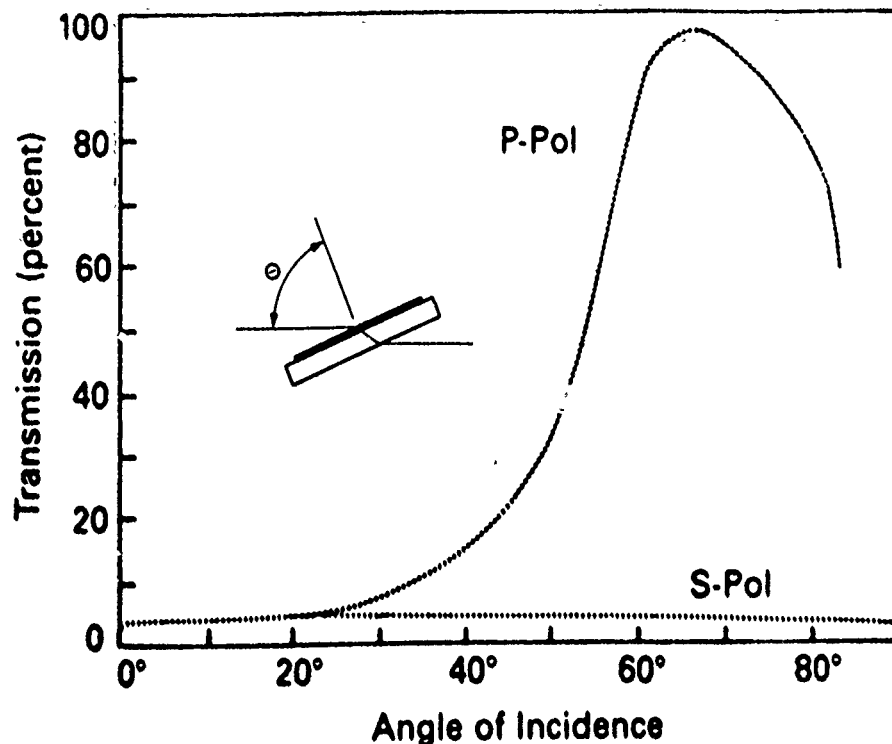


Figure 28. Brewster window transmission efficiency.

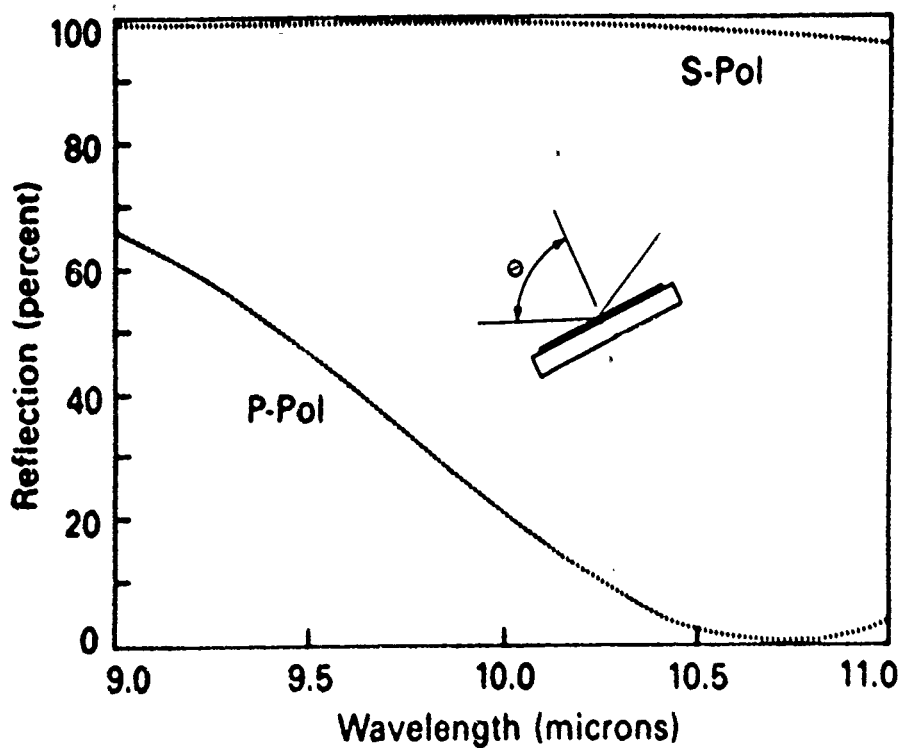


Figure 29. Brewster window reflection efficiency.

4.4 Telescope

4.4.1 Specifications

The optical layout of the telescope is shown in Fig. 30 and the specifications are given in Table 3. The coaxial receiver design consists of an off-axis telescope of three components. The primary and secondary mirrors constitute an off-axis beam expander, and the third mirror is a large diagonal folding mirror which directs and receives the beam.

The beam expander is a parabola-parabola configuration designed to focus at infinity. Another possible design is a Dall-Kirkham configuration which consists of a spherical secondary in conjunction with an ellipsoidal primary. However, this configuration does not focus at infinity and requires an additional corrector plate to simulate an afocal system.

The beam from the TEA laser which is incident on the secondary mirror has a divergence of 2 mrad and is Gaussian in intensity. The waist ($1/e^2$) of the beam at the secondary has a 0.46 inch diameter. The waist is expanded 25x onto the 11.5 inch diameter primary mirror and then is reflected out as a nearly parallel beam (85 μ rad) until it is incident on a large flat mirror that bends the beam 90 degrees from its original direction. The system wave front error produced by these three components is specified to be better than $\lambda/4$ peak to valley at 6327 Å.

The expansion ratio was determined by the optimal balance between losses due to speckle which increase with a larger expansion ratio and losses due to the integrated beam power which increase with a larger ratio. The maximum efficiency occurs when the beam is expanded such that apodization occurs at the beam waist. Approximately 13% of the beam power is lost as a result of the expansion.

4.4.2 Initial Design Considerations

As originally proposed, the telescope was to be of an on-axis Dall-Kirkham design. It was to be fabricated of aluminum and have a wavefront error of $\lambda/4$ at 10.6 μ m. Later investigations and calculations revealed the following problems with this design.

1. It has been concluded that the use of an on-axis design would introduce large backscattering into the detector. NASA previously designed and fabricated an on-axis lidar telescope for their system and after extensive testing, scrapped the on-axis telescope and replaced it with an off-axis telescope¹⁵.

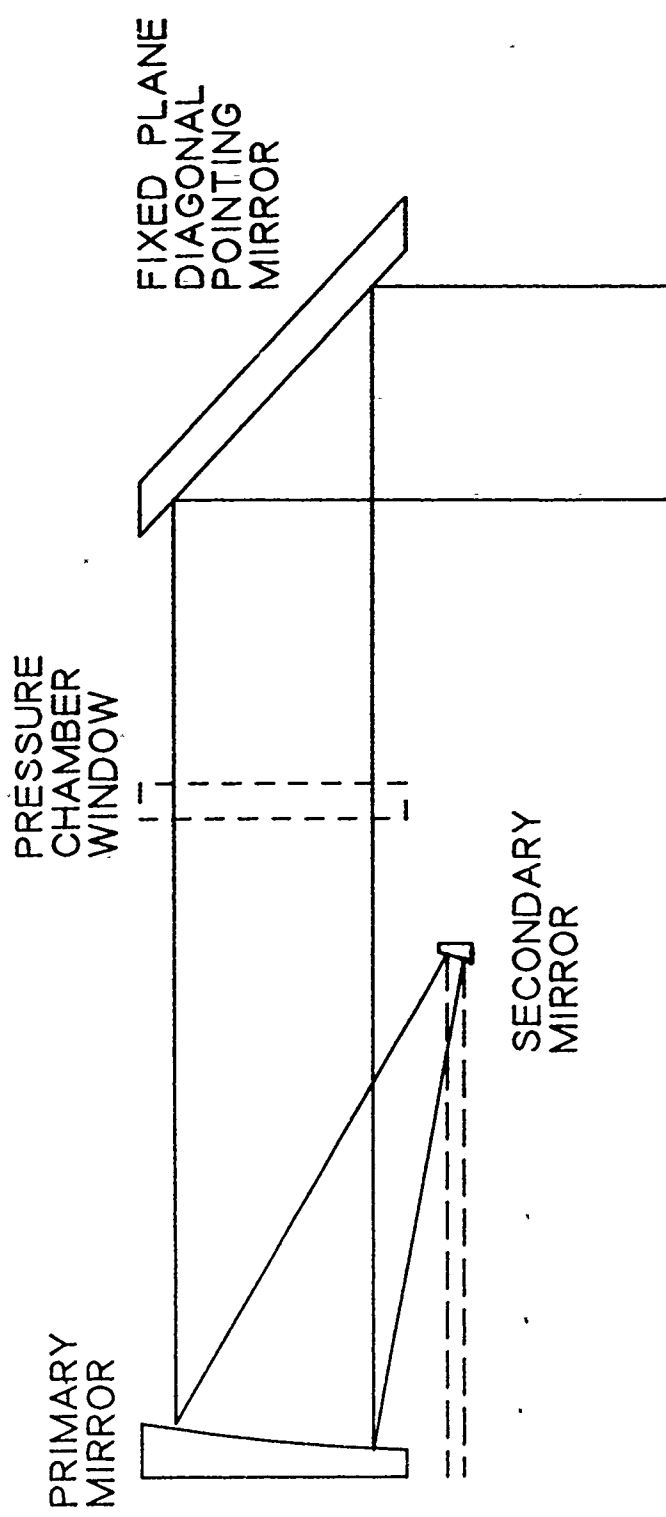


Figure 30. Lidar telescope optical layout.

Table 3
Telescope Specifications

1.0 OPTICAL SYSTEM	
Wavelength	10.6 μm
Total System (Peak-to-Valley) Wavefront Error	$\lambda/2$ at 0.6328 μm $\lambda/33$ at 10.6 μm
Optical Material	Zerodur
Optical Coating	TBD
Optical Alignment	To be measured interferometrically
Optical Mounting	To be provided by Visidyne, Inc., per Visidyne Dwg. E11009 Telescope Assembly
2.0 TELESCOPE	
Design	Afocal Off-Axis Beam Expander
Expansion Ratio	x25
Primary Clear Aperture	11.5 inches (29.25 cm)
Primary Diameter (max)	12 inches (30.5 cm)
Primary Thickness (max)	2 inches (5.1 cm)
Primary Weight (max)	25 lb.
Secondary Clear Aperture	0.47 inch (1.2 cm)
Secondary Diameter	1 inch (2.54 cm)

Secondary Thickness	TBD
Secondary Weight	TBD
Input Laser Beam Characteristics	
Intensity Distribution	Gaussian
Beam Diameter at Secondary	0.47 inches (1.2 cm) at e ⁻²
Divergence	2 mrad
Energy	200 millijoule/pulse
Pulse Rate	100 pps
Pulse Width	1 μ s
Peak Power/Pulse	70 mJ in 130 ns = 540 kW/pulse
Primary-Secondary Distance (nom.)	42.5 inches (108 cm)
Off-Axis, Primary Edge to Secondary Edge Distance ("Edge" defined by O.D. of blank)	1 inch (2.5 cm)
Temperature Range	T = 25 \pm 10°C
3.0 PLANE FOLDING MIRROR	
Folding Angle	90° \pm 1.0
Clear Aperture	Elliptical 17.7 inches (45.0 cm) x 12.5 inches (31.75 cm)
Size (max)	18.2 inches (46.2 cm) x 13 inches (33.0 cm)
Thickness (max)	3 inches (7.6 cm)
Weight (max)	57 lb.
Shape	Truncated Circle

2. The telescope is required to be afocal. Although a Dall-Kirkham design can be made to approximate an afocal system, for the accuracy required for efficient coherent detection, a true afocal system is required. It was recommended that the more complex paraboloid primary-paraboloid secondary system design be adopted.
3. A telescope wave front error of $\lambda/4$ at $10.6 \mu\text{m}$ is not sufficient to provide the recommended $\lambda/4$ total wave front maximum error required for efficient coherent detection^[8]. Thus a $\lambda/34$ at $10.6 \mu\text{m}$ ($\lambda/2$ at 6328\AA) is recommended. The lidar wave front error budget is discussed in Sec. 4.5.4. This level of tolerance required that the telescope primary, secondary, and folding mirrors be fabricated of Zerodur.
4. In order to maintain optical focus over the full operational temperature range of the lidar, $25 \pm 10^\circ\text{C}$, the Zerodur optics must be mounted with a structural material having a minimal thermal coefficient of expansion, namely Super-Invar.

4.4.3 Mechanical and Thermal Considerations

The primary mirror is two inches thick and 12 inches in diameter, and the secondary mirror is one inch in diameter and has a 0.47" clear aperture. The distance between the primary and secondary mirrors is 42.5 inches. In the design of this lidar system, the transmitting laser and the telescope are assembled on the opposite sides of the same optical bench. The material used by the laser manufacturer (Laser Science, Inc.) for the optical bench is 1/2" thick magnesium; in order to match the thermal characteristics of the optical bench a magnesium plate 3/4" thick was chosen as the level for the lidar optics. The total thickness of the optical bench is 1.250 inches, which substantially increased the stiffness of the individual plates. Additional stiffness was added to the laser-lidar optical bench assembly by the addition of stiffening channels. The lidar optical system is specified to maintain optical alignment over the temperature range of $25 \pm 10^\circ\text{C}$. For the telescope optics and mounting structure to maintain alignment over this temperature range, several design techniques were evaluated, as follows:

1. By constructing the telescope structure and the mirrors of the same material, thermal compensation of the telescope is attained. It is currently beyond the state-of-the-art to fabricate metal mirrors to meet the wavefront tolerance required by this lidar system. Therefore this technique was not used.

2. Use of graphite-epoxy composite structural material with Zerodur mirrors would enable both the wave front and thermal specifications to be met. The fabrication of a custom graphite-epoxy-composite structure would be very expensive and require a long lead time.
3. A small specialized mill was found that was able to supply Super-Invar 0.063 ± 0.005 inch thick in small quantities. Over the specified temperature range the thermal coefficient of expansion of the Super-Invar nearly matched that of Zerodur. Thus a thermally compensated telescope could be built using this technique.

The telescope mount shown in Fig. 31 has been designed as a cylindrical tube mounted to the optical bench by three bolts on one end and free on the other end. The optical requirements and weight restrictions are satisfied with this design. At the free end is the one inch diameter off-axis secondary mirror and the related supports. At the supported end the primary mirror is enclosed in a cell which is fastened to the tube. The back of the cell is constructed of small plates welded together in a truss pattern to maintain rigidity. In order to reduce the weight of the telescope, a pattern of lightening holes have been cut in the structural members which reduces the deflection at the free end. A calculation of the free end deflection shows that under a 1g load, the displacement of the secondary with respect to its undeformed position is approximately $2 \mu\text{m}$. This displacement is insignificant compared to the lidar $10.6 \mu\text{m}$ wavelength.

A stress analysis performed on selected sections of the telescope structure showed that the maximum stress induced by a 10g parachute opening is approximately 700 psi. For the Super-Invar material, with an ultimate tensile strength 96 800 psi, the safety factor would be $96800/700 = 91$. A preliminary computation of the natural frequency of the telescope shows an approximate value of 1000 Hz.

In order to compute the moment of inertia I of the telescope, a computer program was developed that calculates the moment of inertia of a cylindrical shell having a set of round lightening holes. The results of these calculations are summarized in Fig. 32. The moment of inertia of a thin cylinder with a fixed radius of 7.563" as a function of the wall thickness, and different hole diameters characterized by the parameter α . If we chose $\alpha = 7.5$, which corresponds to 2" diameter lightening holes, I increases with the thickness of the wall, reaching

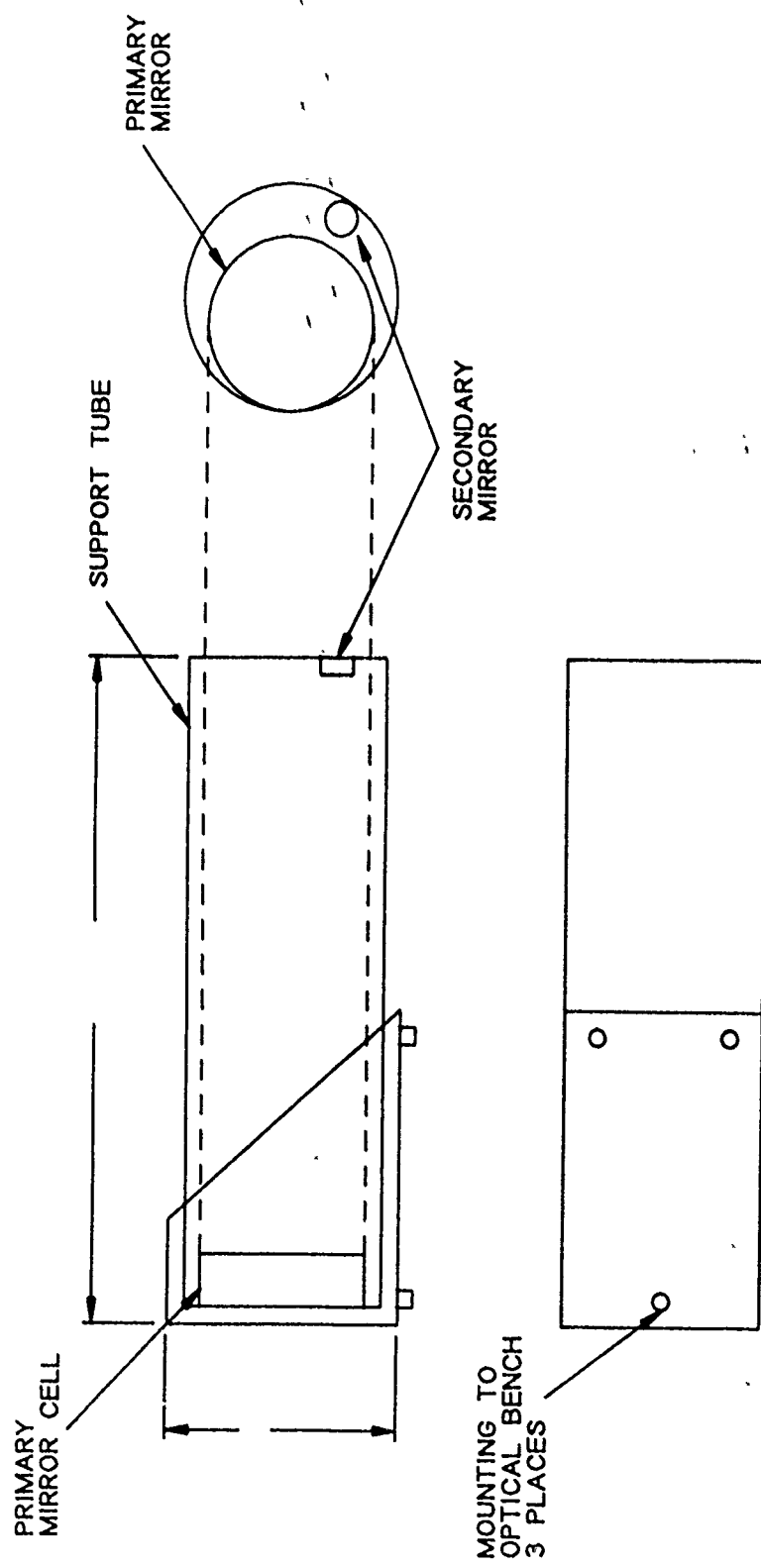


Figure 31. Balloonborne coherent CO₂ lidar telescope structure.

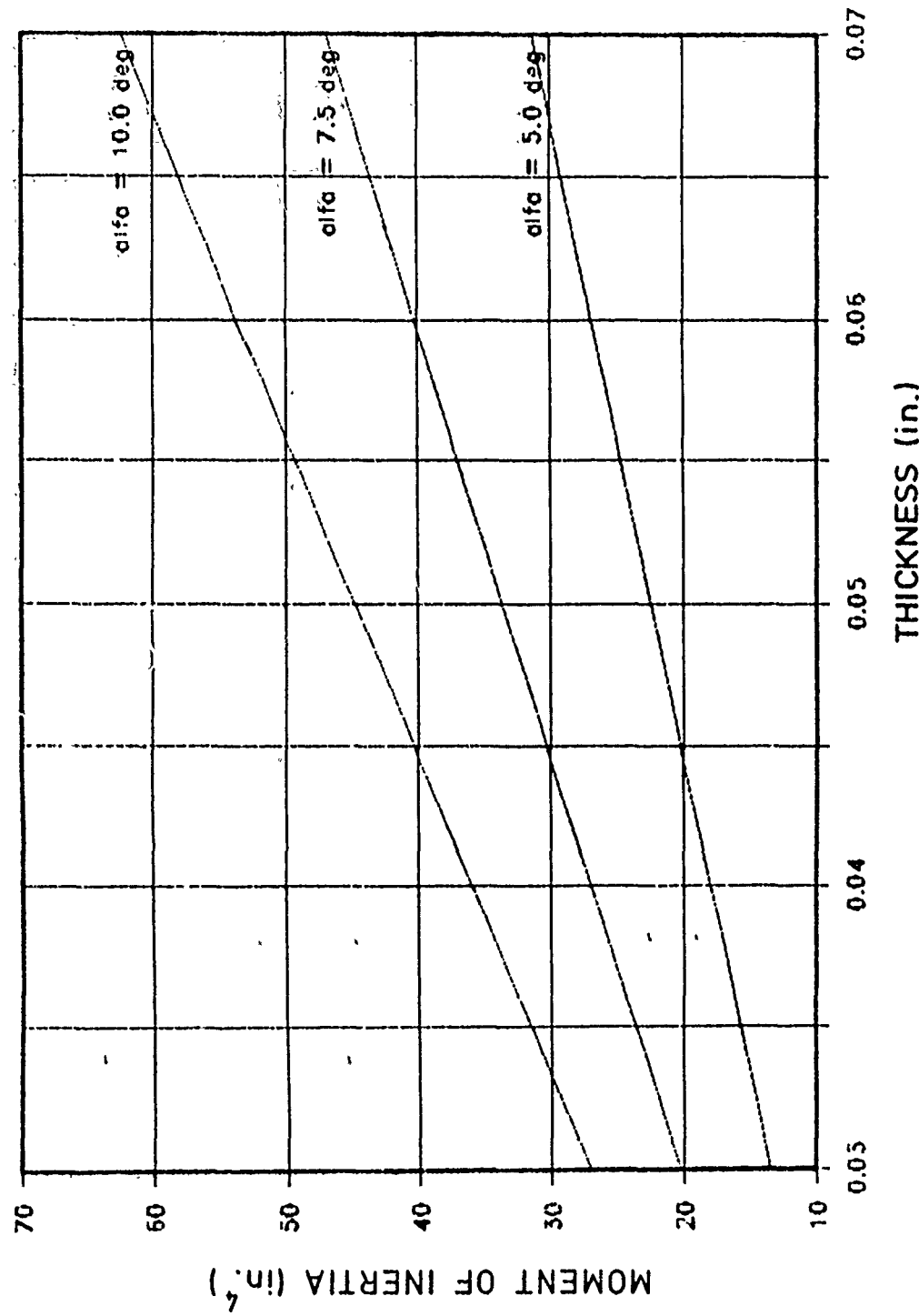


Figure 32. Moment of inertia, perforated tube vs. wall thickness.

a value of $I \sim 42$ in 4 for a wall thickness of 0.063 in. Figure 32 also demonstrates that increasing the diameter of the holes ($\alpha = 5.0$) results in the moment of inertia decreasing, and reducing the diameter of the holes ($\alpha = 10.0$) results in the moment of inertia increasing. In the case where the hole area is reduced, the gain in the moment of inertia is offset by the increased weight of the cylindrical shell, but the increased stiffness does not lead to a reduction of the displacement between primary and secondary mirrors. The selected 2" diameter of the uniformly distributed holes around the periphery of the shell achieves an optimum compromise between weight and stiffness of the structure. The structural stress analysis mentioned above was based on a moment of inertia of 42.4 in 4 .

4.5 Optical Alignment and Beam Characteristics

The lidar optics consists of three beams which must be maintained at diffraction limited quality and accurately aligned. These beams are the transmitted laser, the received backscatter, and the local oscillator. The optical component mounts have been designed to separate translation adjustment, (x,y,z) from those of angular motion (Θ, ϕ). Mounted on the lidar optical bench are four remotely controlled fine alignment adjustments which are available for flight operations. These remote adjustments are listed in Table 4. All of the optical components will transmit the visible light from a He-Ne laser which is fed through the system to facilitate the aligning process. For coarse alignment the infrared beam at 10.6 μm can be viewed by intercepting the radiation with a thin sheet of liquid crystal material. To help locate the beams during initial alignment, apertures have been mounted at different places in the optical paths of the three beams.

The height and angle of the transmitted beam incident on the secondary mirror of the telescope are controlled by a precision beam director located on the lidar side of the optical bench. Lateral displacement of the beam is accomplished by rotating the beam directors on the laser side and the lidar side about the optical axis.

The alignment of the received beam and the local oscillator are not independent. First, the received beam is aligned parallel to the optical axis of the detector lens by adjusting the folding mirror located downstream from the Brewster window. The local oscillator is then brought in

Table 4
Remote Adjustments Used for Alignment

<u>Component</u>	<u>Adjustment</u>	<u>Purpose</u>
Lens	X	Translates beams in x-direction on detector
Lens	Z	Translates beams in z-direction on detector
Beam Splitter	Y	Translates beams in y-direction on detector
LO Beam Detector	Z	Translates local oscillator in z-direction on detector

line with the received beam by adjusting the LO beam directors and the beamsplitter. Finally, the two beams are centered on the detector by moving the focusing lens in the x-z plane, which will translate the overlapping beams.

A telescope alignment port is positioned between the quarter-wave plate and the secondary mirror. When the beam is autocollimated, the port is designed to provide access to an interferometer used to monitor the telescope alignment and the wave front distortion from the telescope. The interferometer will also be used to monitor the wave front distortion of the entire beam by sampling the beam directly in front of the detector.

4.5.1 Detector Size

A HgCdTe photovoltaic detector is used to detect the $10.6 \mu\text{m}$ radiation. Photovoltaic detectors are generally used in heterodyne detection because of their high frequency response and their low shot noise. A typical manufacturer's specified quantum efficiency for this type of detector is approximately 60%. However, this specification is for low frequency signals only, and the detector efficiency at higher frequencies may be as much as a factor of two less. Measured characteristics for the actual detector are given in Table 5 and Fig. 33.

The detector size depends on the beam spot sizes and their wavefront distributions. How the local oscillator beam (LO) and the received signal interact with the detector determines the heterodyne mixing efficiency. In this lidar the intensity distribution of the LO is Gaussian and the distribution for the received signal is similar to an Airy pattern.

4.5.2 Transmitted Beam

The transmitted beam from the TEA laser and the CW laser providing the LO are generated in a pure Gaussian mode. The intensity distribution describing the Gaussian mode is

$$I = I_0 e^{-2(\frac{r}{w_0})^2} \quad (28)$$

where r is the radius of interest and w_0 is known as the waist of the distribution. At the point $r = w_0$, where $I/I_0 = e^{-2}$, the total power contained within the radius is 87%.

The divergence of a beam limited by diffraction is described below for the following two cases: a plane wave incident on a circular aperture (Airy pattern) and a Gaussian distribution incident on a circular aperture. The full divergence angle for each case is given by

Table 5
Lidar Heterodyne Detector Characteristics

Detector Type: HgCdTe PV Date: 09/15/88
 Part Number: 22218 Dewar: 358-2SMA
 Chip Serial No.: PV 435 Window: ZnSe A/R
 Model Number: MPV11-0.1-BXT60

Connector	:	SMA-1	SMA-2
Element Size (mm)	:	0.10 x 0.10	0.20 x 0.20
Area (cm ²)	:	1.16E-4	4.13E-4
RO (ohms)	:	1.03E4	3.77E3
ROA (ohms-cm ²)	:	1.20	1.58
Signal (mV)	:	3.1	9.8
Responsivity, Blackbody (A/W)	:	2.06	1.84
Responsivity, Lambda (A/W)	:	6.55	5.79
Cutoff Wavelength (Microns)	:	11.99	11.96
G Factor	:	3.00	3.00
Quantum Efficiency (%)	:	67.5	60.2
Detector Temperature (Kelvin)	:		77
Blackbody Temperature (Kelvin)	:		1000
Distance, Detector from BB (cm)	:		33.5
Chopping Efficiency	:		0.4
Aperture Diameter (in.)	:		0.2
Energy Density at Detector (W/cm ²)	:		1.29E-4
Window Transmission (%)	:		95
Feedback Impedance (ohms)	:		1E5

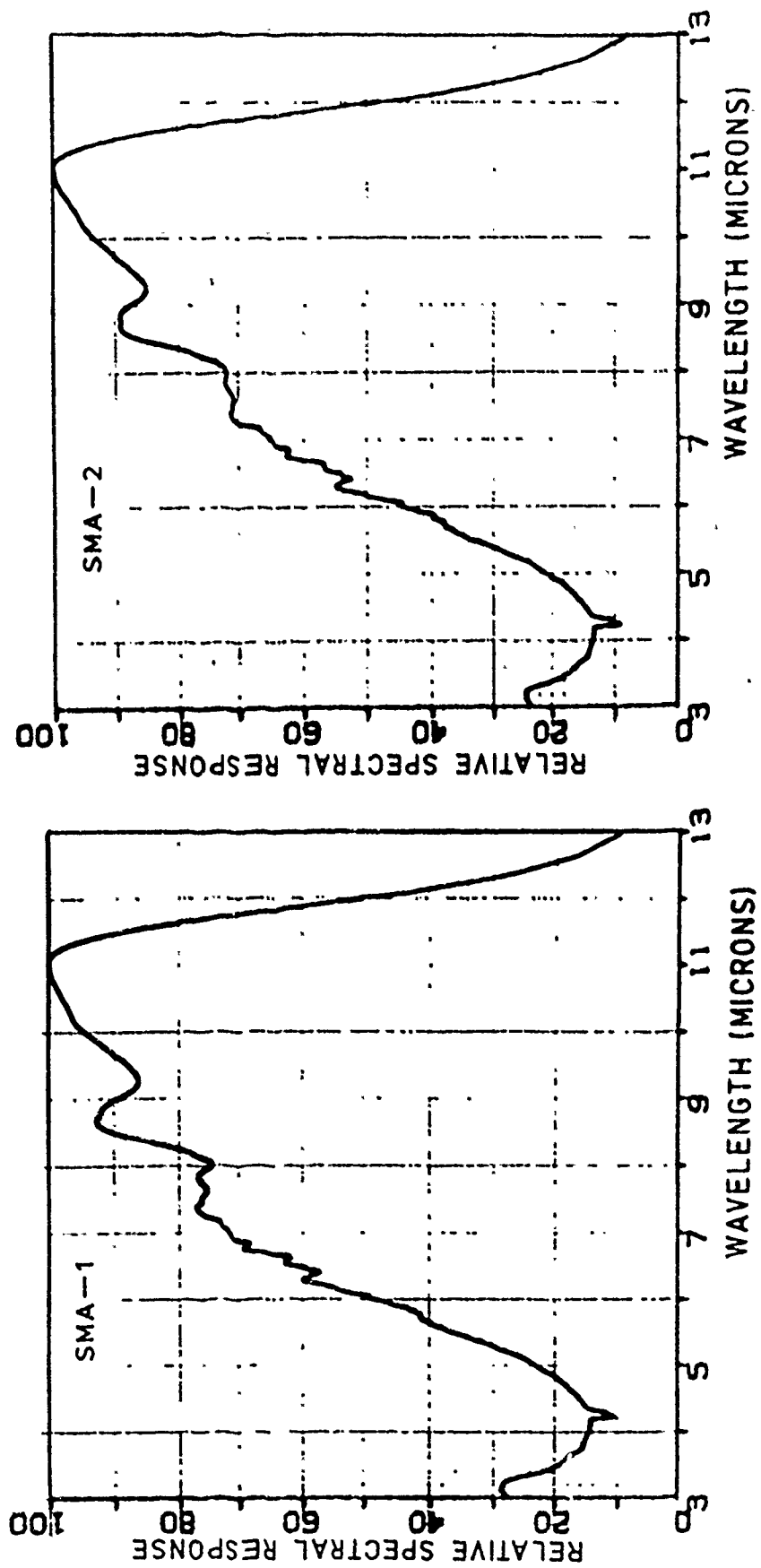


Figure 33. Detector spectral response.

plane wave: $\Theta = 2.44 \lambda/D$

Gaussian: $\Theta = (4/\pi) \lambda/2w$

The e^2 values for the TEA beam and the LO measured by LSI are listed below: the corresponding values for Θ were calculated using the Gaussian formula listed above.

Beam	w ₀ (mm)	Θ (mrad)
TEA	4	1.7
LO	1.8	3.7

The optical path length from the TEA laser to the secondary mirror is 2.12 m (83.5 inches). The beam spot size at the mirror is $8 \text{ mm} + (2120 \text{ mm}) (0.0017) = 11.6 \text{ mm}$ (0.46 inches). The optical path length from the cw laser to the lens for the LO is 1.69 m (66.5 inches). The size of the LO spot size at the lens is then $3.6 \text{ mm} + (1690 \text{ mm}) (0.0037) = 9.85 \text{ mm}$.

4.5.3 Received Beam

The signal backscattered by the atmosphere is approximately a plane wave when it reaches the 11.5 inch ZnSe chamber window. The incident radiation passes through the telescope and is demagnified by a factor of 25, reducing the ray bundle to a diameter of 11.7 mm. The optical path length from the secondary mirror to the focusing lens is 1.56 meters (61.4 inches).

The focusing lens is a standard one inch diameter lens with a 2.5 inch (63.5 mm) focal length which has a positive meniscus shape to reduce spherical aberrations. The diffraction pattern generated by the telescope-lens system is calculated. The plane wave radiation incident on the afocal telescope is treated as a plane wave incident on an aperture 11.7 mm in diameter.

First we compute the electric field incident on the focusing lens which we take to have a radius R₂. We use a Huygen's construction wherein each point on the aperture (of radius R₁) is assumed to be an infinitesimal source of spherical wavelets. The distance between the aperture and lens is sufficiently large that all the electric vectors at the lens are assumed to be parallel.

The path difference δ between an arbitrary point r_1 on the aperture and arbitrary point r_2 on the lens is

$$\delta(r_1, r_2, \beta) = (r_1^2 + r_2^2 - 2r_1 r_2 \cos\beta + D^2)^{1/2} \quad (29)$$

where D is the separation between the aperture and the lens, and $\cos\beta = \hat{r}_1 \cdot \hat{r}_2$. For $D \gg r_1$ and r_2 , $\delta(r_1, r_2, \beta)$ can be approximated as

$$\delta(r_1, r_2, \beta) \approx D + r_1^2/2D + r_2^2/2D - (r_1 r_2 \cos\beta)/D. \quad (30)$$

The net electric field at an arbitrary point on the focusing lens is therefore

$$E(r_2, t) \propto E_0 e^{i\omega t} \int \int \exp[2\pi i \delta(r_1, r_2, \beta)/\lambda] r_1 dr_1 d\beta. \quad (31)$$

The integral over β can be carried out analytically and yields

$$E(r_2, t) \propto E_0 e^{i\omega t} \exp(\pi i r_2^2/\lambda D) \int_0^R \exp(\pi i r_1^2/\lambda D) J_0(2\pi r_1 r_2/D\lambda) r_1 dr_1. \quad (32)$$

Note that because of the axial symmetry of the problem, the electric field depends only on the radial position on the lens.

We make use of the axial symmetry to compute the diffraction pattern found when this incident electric field is acted upon by the lens. In this case the diffraction pattern is just the modules squared of the Bessel transform of E :

$$I(k) \propto [\int_0^R E(r_2, t) J_0(kr_2) 2\pi r_2 dr_2]^2 \quad (33)$$

where $k = 2\pi \sin\Theta/\lambda$ and Θ is the angular displacement within the diffraction pattern. This double integral was evaluated numerically with a small computer.

The diffraction pattern was evaluated relative to the design of the coherent lidar payload, where $R_1 = 0.58$ cm, $R_2 = 1.27$ cm, $D = 156$ cm, and $\lambda = 10.6 \mu\text{m}$. The intensity and phase of the radiation incident on the focusing lens are shown in Figs. 34 and 35, respectively, as a function of the radial distance from the center of the lens. The electrical field intensity from the aperture at the lens position has a hole at the center which results from the near-field diffraction pattern. The diffraction pattern observed at the focal plane of the lens is shown in Fig. 36. Note that the diffraction pattern is nearly identical to the pattern that would be obtained by a lens with a diameter equal to that of the first aperture (of radius R_1). Significant deviations from this result do not occur until the separation between the aperture and the lens becomes larger than ~ 250 cm.

The spot size of the received signal at the detector is then calculated from Fig. 37 to be

$$\begin{aligned} d &= \Theta f \\ &= 2.44 \lambda f/D \\ &= (2.44) (10.6 \times 10^{-6} \text{ m}) (0.0635 \text{ m})/(0.0156) \\ &= 109 \mu\text{m} \end{aligned}$$

A detector 100 μm in diameter will be assumed.

The spot size of the LO due to diffraction is

$$\begin{aligned} 2w &= (4/\pi) \lambda f/2w \\ &= (4/3.14) (10.6 \times 10^{-6}) (0.635 \text{ m})/(2 \times 0.00985) \\ &= 87 \mu\text{m}. \end{aligned}$$

Cohen^[6] calculates the mixing efficiency of an Airy signal and a Gaussian LO signal. In this calculation the Airy signal χ_o and the Gaussian signal Z_o are characterized by $\chi_o = (\pi r_o)/(\lambda F)$ and $Z_o = r_o/w$, where r_o is the detector radius and F is equal to f/D_{Airy} . The value of χ_o for this system (assuming $r_o = 50 \mu\text{m}$) is 3.51. The value of Z_o for $r_o = 50 \mu\text{m}$ and $w = 43.5 \mu\text{m}$ is 1.15. Assuming perfect alignment of the received signal and LO, the above values for χ_o and Z_o correspond to a mixing efficiency of 70%. If a 200 μm diameter detector is assumed, the values of χ_o and Z_o would then be 7.02 and 1.3, respectively, and the mixing efficiency would be less than 30%. It should be noted that a maximum heterodyne efficiency of 82% is reached when the two wave fronts are perfectly aligned and are evaluated in the limit where they are uniform over the detector.

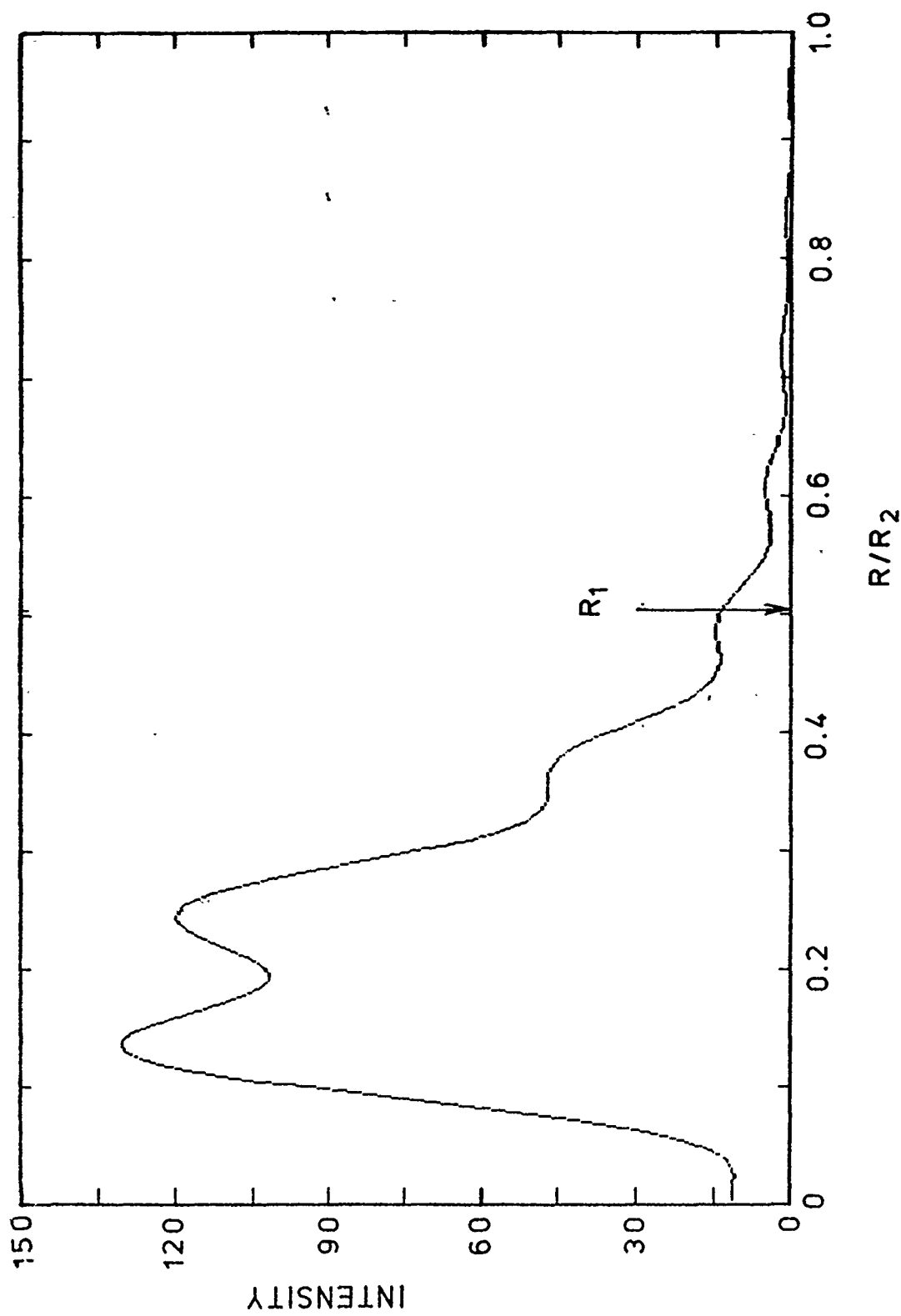


Figure 34. Intensity of the incident radiation of the focusing lens as a function of the radial distance.

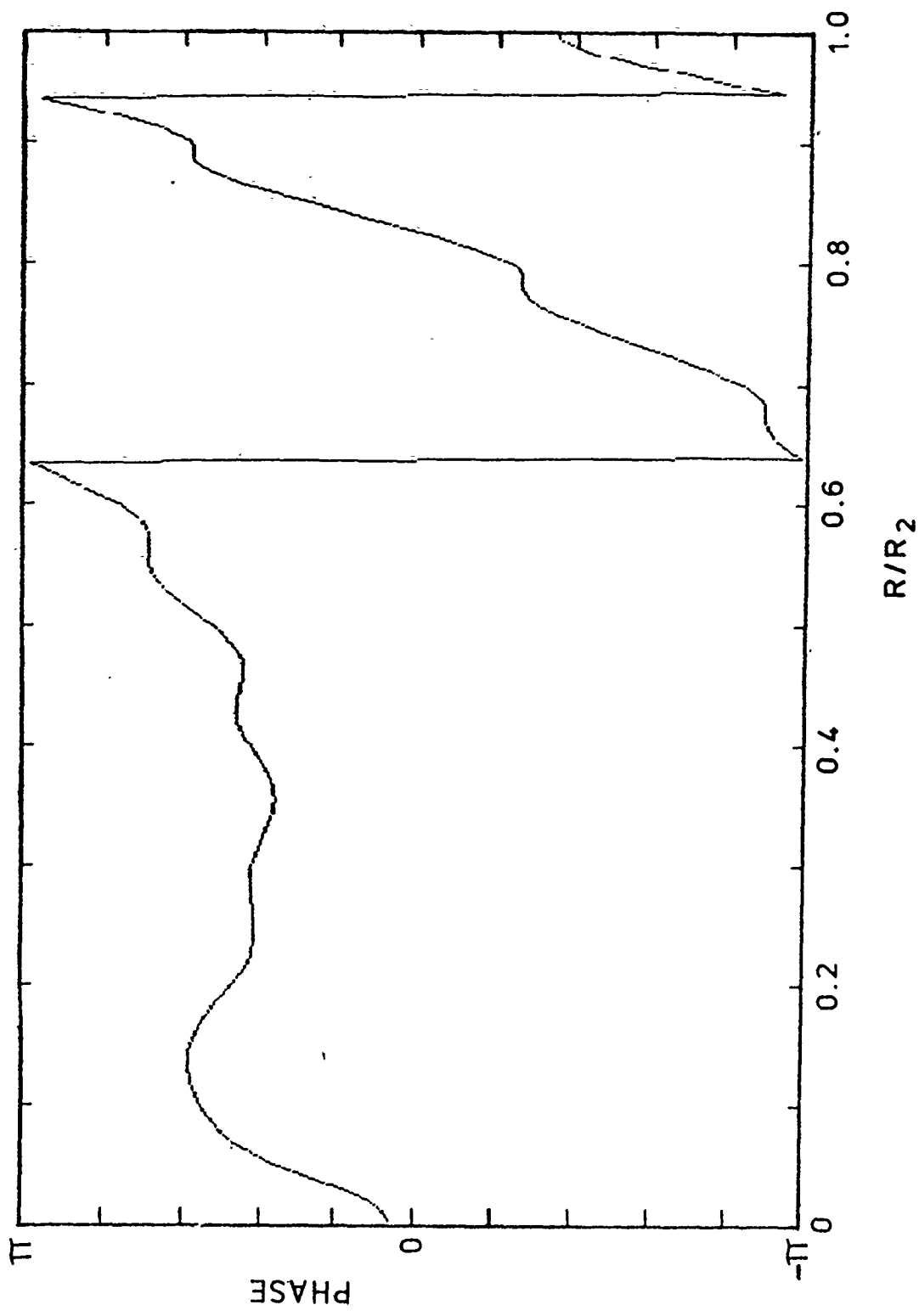


Figure 35. Phase of the incident radiation of the focusing lens
as a function of radial distance.

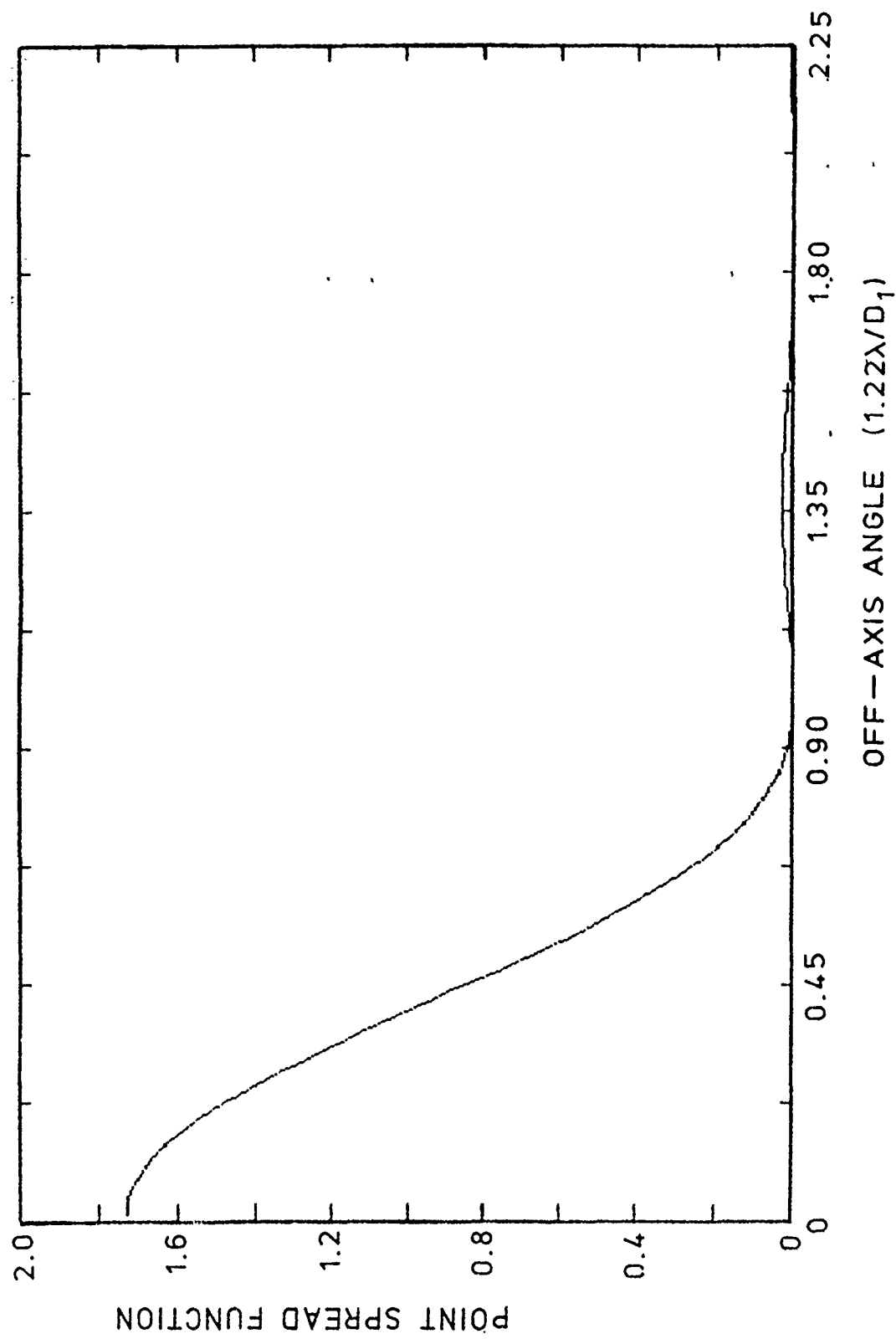


Figure 36. Diffraction pattern at lens focal plane.

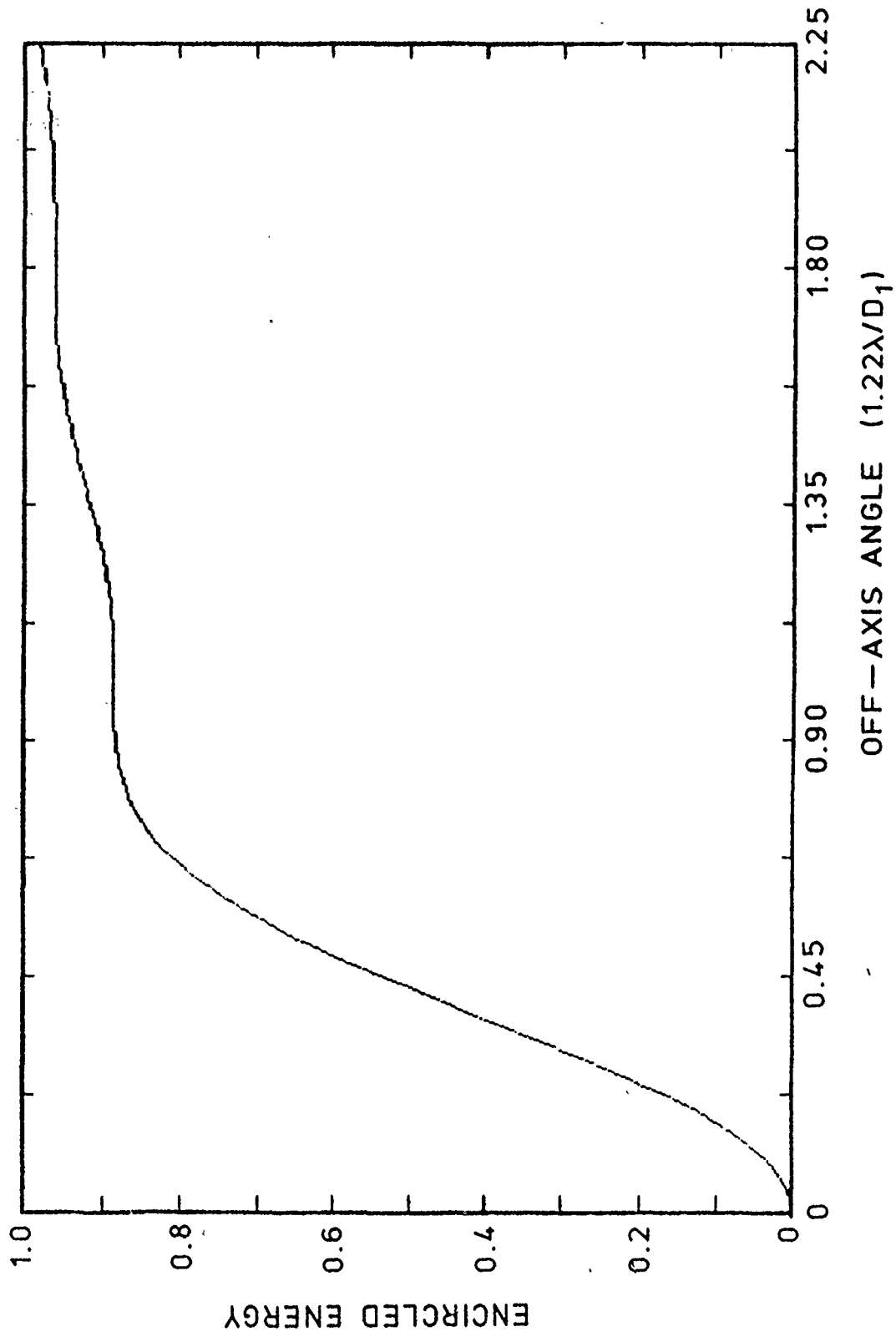


Figure 37. Integrated energy at detector vs. off-axis angle.

4.5.4 Lidar Wave Front Errors

In the course of the design of the coherent lidar it was determined that a complete wave front error budget must be developed. The purpose of this budget is to define the peak-to-valley wave front errors introduced by each optical element and to demonstrate that the total wavefront error of the combined local oscillator wavefront and the received wave front is $\lambda/4$. This is the maximum wave front misalignment allowable for adequate heterodyne efficiency as described by Cohen^[8], who also considers the effects of signal and local oscillator optical misalignment on heterodyne detection. The optical misalignment is defined in terms of the wavefront misalignment in degrees. To relate the heterodyne modulation parameter γ to the peak-to-valley wave front error E ,

$$E = \frac{r\theta}{\lambda} \quad (36)$$

where

r is detector radius ($100 \mu\text{m}$),

Θ is angular misalignment (radians), and

λ is $10.6 \mu\text{m}$.

Table 6 shows the degradation of the modulation parameter as a function of wave front error E . Table 7 lists the wave front error for each component in each of the three optical paths of the lidar and the total error for the lidar system. For comparison, the additional wave front error which would be introduced if a germanium window were used is also shown. An IR transmitting optical window is required in the lidar pressure chamber to provide a pressure barrier between the lidar at 14.7 psia and the high altitude ambient pressure.

The wave front errors introduced by various material windows were investigated. Discussions^[9] regarding a $13"$ diameter germanium window for the CO_2 lidar system revealed that the wave front error from a window $3/4"$ thick can be expected to be between $\lambda/3$ and $\lambda/2.5$. The reason for the degraded wavefront is not the quality of the polished surfaces, but instead is due to the inhomogeneity of the material. The formula for the wave front error is

Table 6

Degradation of Heterodyne Modulation as a Function
of Wave Front Error

<u>Total Peak-to-Valley Wavefront Error</u>	<u>Wave Front Angular Misalignment (Degrees)</u>	<u>Case 2⁽¹⁾ Heterodyne Detection Parameter</u>
0.0	0.0	0.7
0.26	1.6	0.45
0.51	3.1	0.08

Table 7

Wave Front Error Summary for CO₂ Lidar
 $\lambda = 10.6 \mu\text{m}$

LOCAL OSCILLATOR		
Laser	$\lambda/10$	
Four Folding Mirrors	$\lambda/84$	
Beamsplitter	$\lambda/20$	
	$\lambda/8.9$ (Quadratic Sum)	
RECEIVER		
Chamber Window	$\lambda/13$ (ZnSe)	$\lambda/3$ (Ge)
Telescope	$\lambda/34$	
$\lambda/4$ Plate	$\lambda/17$	
Brewster Window	$\lambda/20$	
Mirror	$\lambda/167$	
Beamsplitter	$\lambda/14$	
	$\lambda/7.5$ (Quadratic Sum) →	$\lambda/2.9$
TRANSMITTER		
Laser	$\lambda/10$	
2 Folding Mirrors	$\lambda/120$	
Brewster Window	$\lambda/14$	
$\lambda/4$ Plate	$\lambda/17$	
Telescope	$\lambda/34$	
Chamber Window	$\lambda/13$ (ZnSe) $\lambda/6.4 \leftarrow$ Quadratic Sum →	$\lambda/3$ (Ge) $\lambda/2.8$
TOTAL WAVEFRONT ERROR	$\lambda/4.3$	$\lambda/2.0$

- NOTES: 1. Wave front tolerances for the lens, detector window, and detector surface are small compared to the IF (40 MHz) wavelength (reference mixing theorem).
2. Telescope includes primary, secondary, and plane diagonal pointing mirror.

$$\Delta \lambda = P(N-n) S + \Delta N t \quad (37)$$

where

P is the number of sides (two for transmission),

N is the index of refraction for the material,

n is the index of refraction for air,

S is the surface figure,

ΔN is the error in N (inhomogeneity), and

t is the material thickness.

According to Exotic Materials¹⁷¹ ΔN for commercial Ge is $1.0-1.5 \times 10^{-4}$. Their proprietary methods may be able to reduce this number but not to the levels required to obtain $\lambda/10$ peak to valley (P.V.). Adams¹⁸¹ of Eagle Picher informed Visidyne, Inc. of two independent measurements of ΔN in Ge.

Measurement	Size	ΔN
1.	3" diameter x 1" thick	2×10^{-4}
2.	6" diameter x 1" thick	
	Polycrystalline samples	1.27×10^{-4} 1.02×10^{-4} 0.96×10^{-4} 0.86×10^{-4}
	Single crystal sample	0.81×10^{-4}

Because of the high index of refraction in Ge ($N_{Ge} \sim 4$), the surface figure required for $\Delta\lambda = \lambda/10$ P.V. (assuming the material is perfect!) must be better than $\lambda/60$ ($\lambda/3.6 @ 0.6328 \mu m$). Standard surface figures for germanium optics are $\lambda/40$ ($\sim \lambda/2.4 @ 0.6328 \mu m$); this corresponds to $\Delta\lambda = \lambda/6.7$.

To maintain a total error of $\lambda/8$, the contribution from the material must be $\sim \lambda/40$. This corresponds to $\Delta N = 15 \times 10^{-6}$ for a piece 0.75" thick. The contribution to the error from material with $\Delta N = 1000 \times 10^{-6}$ is $\lambda/5.6$.

The total error expected from a surface figure of $\lambda/40$ and $\Delta N = 100 \times 10^{-6}$ is $\lambda/3$.

Exotic Materials routinely measures wave front errors at 10.6 μm after transmission through Ge windows. The errors recorded are typically $\lambda/3$ P.V., which is consistent with the numbers derived above. It should be mentioned that Vandermeer¹⁹ questions the measurements of ΔN and believes the total errors derived are too large based on data from smaller Ge optics he has seen.

ZnSe is very desirable to use instead of Ge for the following reasons. The index of refraction is 2.4, and the inhomogeneity ΔN of our material is $< 3 \times 10^{-6}$, 40 times purer than Ge. (The ΔN for Ge is larger because germanium must be doped to remove the free charge carriers.) The disadvantages of ZnSe compared with Ge are its higher price ($\sim 1\text{-}1/2$ times more costly) and lower tensile strength (although a 3/4 inch thick ZnSe window still has a safety factor of 5).

Assuming a surface figure of $\lambda/40$,

$$\begin{aligned}\Delta\lambda_{\text{ZnSe}} &= 2(2 \cdot 4 - 1) \frac{\lambda}{40} + (3 \times 10^{-6}) (0.0254 \mu\text{m}) \frac{\lambda}{10.6 \times 10^{-6} \mu\text{m}} \\ &= \frac{\lambda}{14.3} + \frac{\lambda}{14.0} = \frac{\lambda}{13}.\end{aligned}\tag{38}$$

Based upon this analysis it is recommended that the ZnSe window be used.

5.0 SIGNAL PROCESSING

5.1 Local Oscillator Power

To achieve ideal heterodyne detection (i.e., shot noise limited) the local oscillator power incident on the detector must be sufficient to dominate the noise generated by the detector preamplifier. This power is⁽¹⁹⁾

$$P_{LO} > > \frac{2kT_N}{e} \frac{h\nu}{e} \frac{1}{\eta R} \quad (39)$$

where

k = Boltzmann's constant,

T_N = Noise temperature of preamplifier,

h = Planck's constant,

$\nu = c/\lambda$,

e = Unit electron charge,

η = Heterodyne efficiency, and

R = Load resistance.

Assuming a 300°K noise temperature and choosing a 50 ohm resistor yields a local oscillator power requirement of a few milliwatts.

5.2 Electronics

The signal processing electronics, Fig. 38, provides the capability to acquire 10.6 μ m backscatter data at the maximum laser pulse repetition rate of 10.7 Hz. The detected signal is an amplitude-modulated 40 MHz waveform which is amplified and bandpass filtered (80 MHz) before being fed to an Envelope Detector. The detected signal is low-pass filtered and sent to the payload CAMAC electronics where a 10 bit A-D Converter and Averager module converts the data to 10 bit digital and averages a selected number (typically 10) of laser pulses. A 2 MHz A-D sampling rate provides 75 meter backscatter range bin data. Two Envelope Detection channels are provided to extend the measurement dynamic range. The gain of each

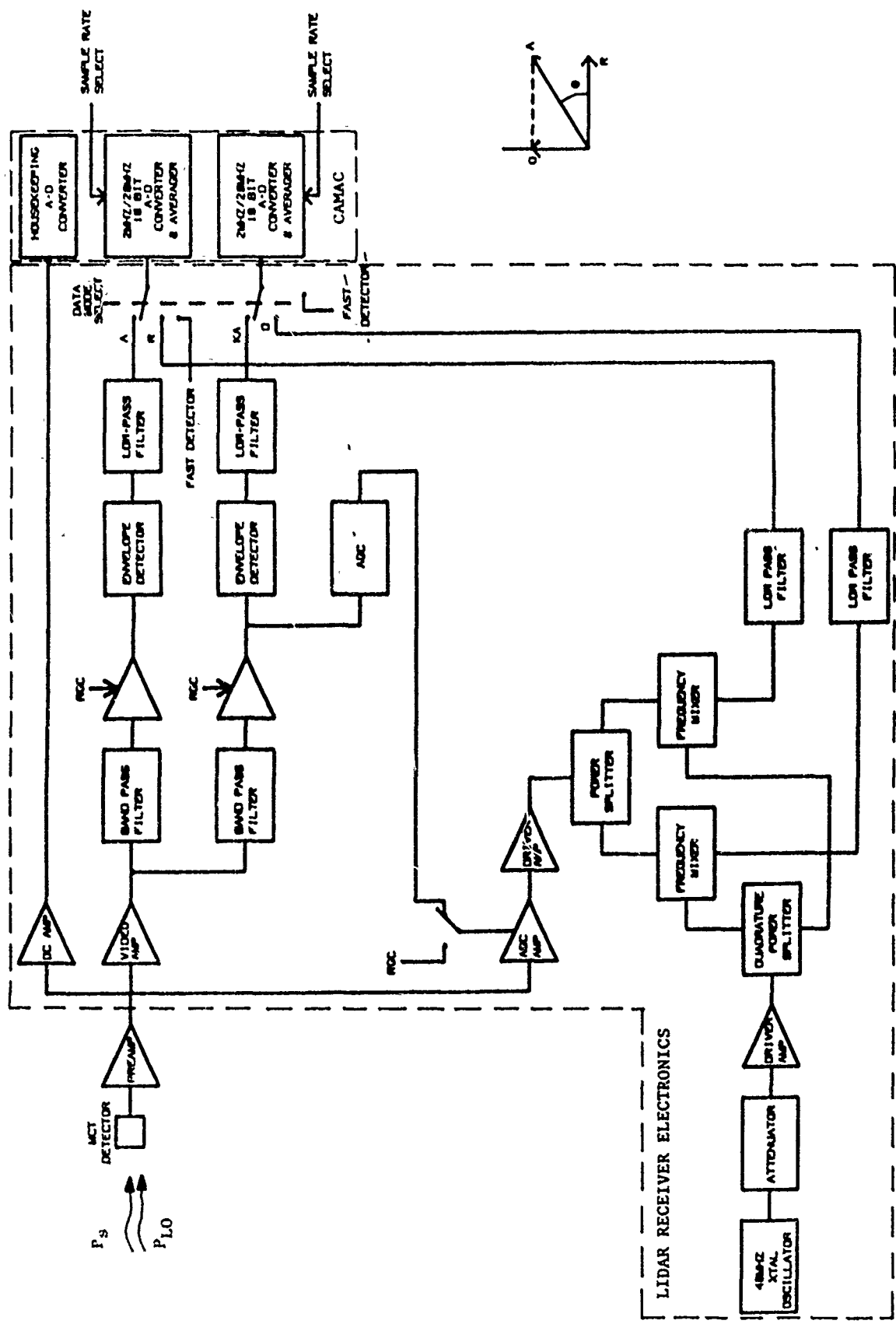


Figure 38. Signal processing electronics.

channel is digitally controlled by the CAMAC electronics. A dc amplifier is provided to monitor the detector average signal which is the cw local oscillator power incident on the detector.

An optional capability which could be incorporated into the system is to measure aerosol velocities along the lidar beam backscatter. In this channel the detected backscatter lidar signal, modulated at 40 MHz, is split into inphase and quadrature components. These components are then mixed with a 40 MHz crystal oscillator reference and low pass filtered to obtain a low frequency signal. The CAMAC 10 bit A-D converter samples these signals at 20 MHz and transfers the data to the down-linked PCM data stream. Frequency analysis of this backscatter data would then be performed during post-flight data analysis by Fast Fourier transforming the backscatter data stream in 32 sample chunks ($1.6 \mu\text{s} - 240 \text{ m}$). The inphase and quadrature frequency spectra amplitudes would then be combined to obtain a resultant aerosol velocity which then could be multishot averaged to obtain aerosol velocity data.

The lidar receiver electronics would be packaged in an enclosure which is mounted inside one of the lidar chamber hemispherical covers. The lidar payload electronics configuration is shown in Fig. 39.

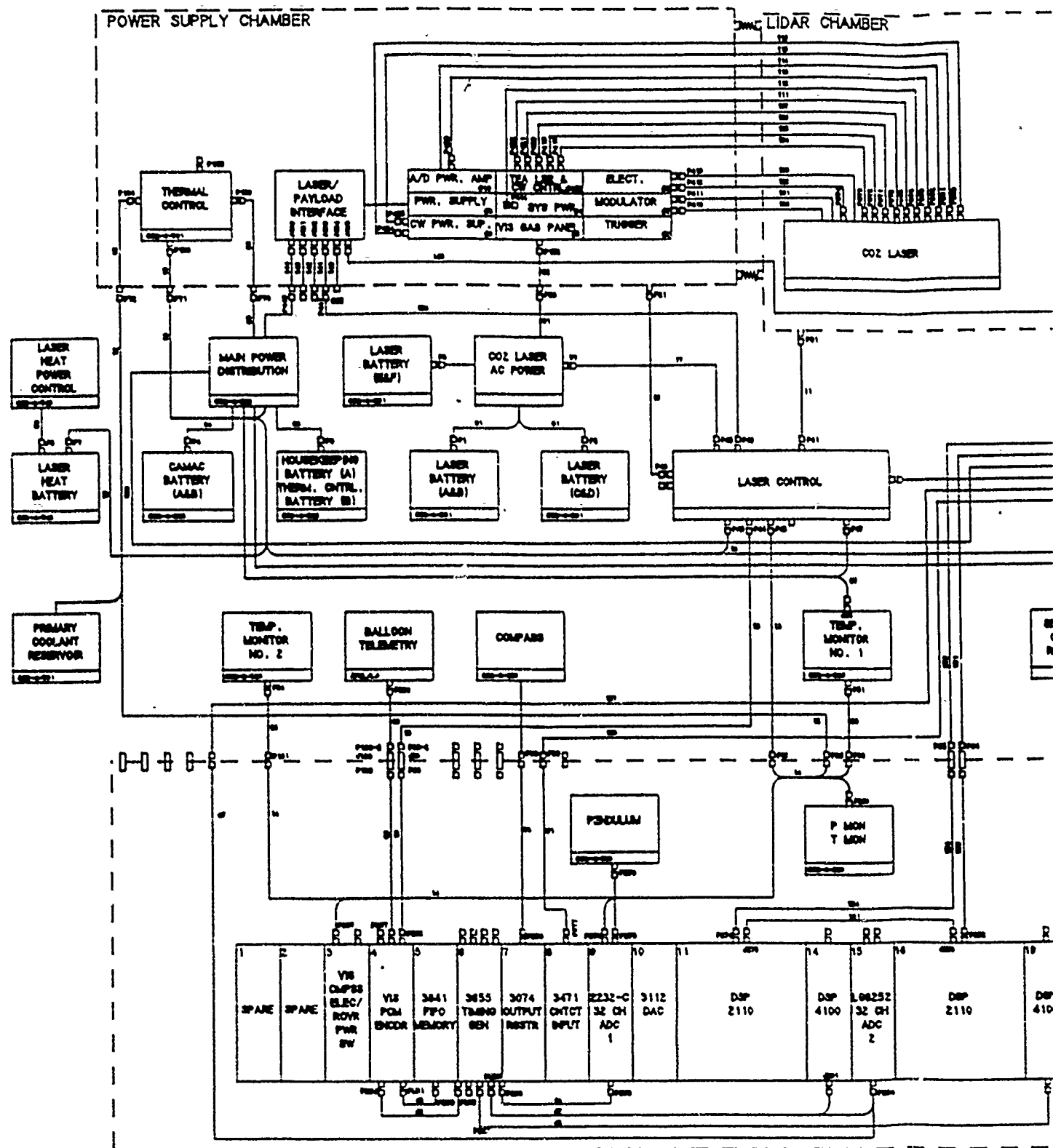


Figure 39.

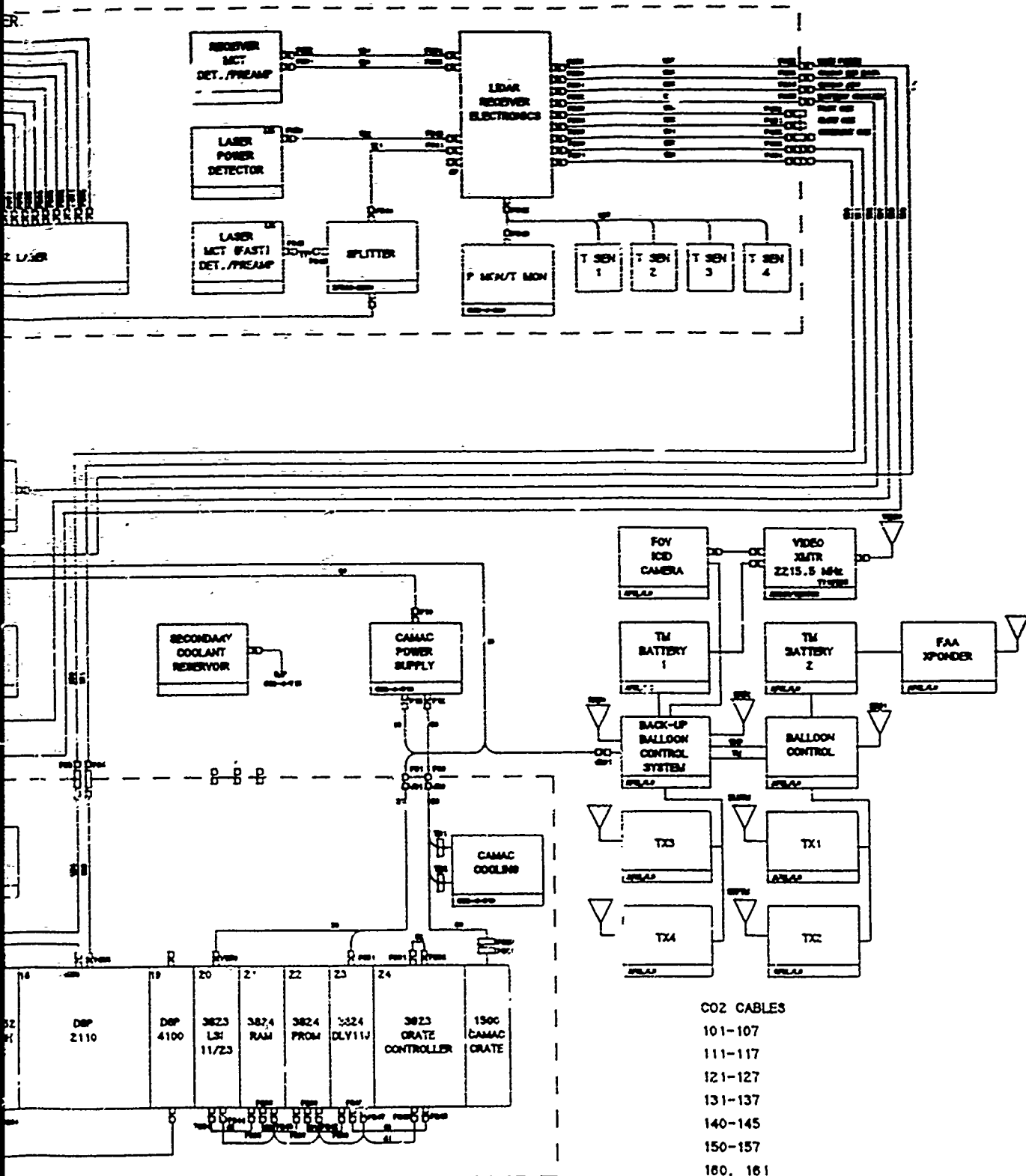


Figure 39. Lidar payload electronics.

202

6. BALLOON PAYLOAD

6.1 Mechanical Design

A balloon payload for the coherent CO₂ lidar system was designed¹¹¹¹ and fabricated. The functional requirements of the coherent CO₂ lidar balloon payload were the following:

1. To provide a lidar measurement platform which could be flown at typical altitude of 20 km for a period of up to eight hours using USAF balloon integration and launch facilities.
2. To house the lidar optics, CO₂ laser, and laser control electronics in an ambient 14.7 psia pressure and temperature environment.
3. To provide the additional systems required to perform a flight mission, thermal control, power, and telemetry uplink commandability.
4. To provide the capability for the lidar system to maintain optical alignment under all flight conditions.
5. To provide a robust structure which would protect on-board systems from damage during launch, parachute landing, and recovery.

The design pressure and shock environment specifications for the payload are in Table 8. The configuration of the lidar pressure chamber is shown in Fig. 40, and the laser power supply chamber is shown in Fig. 41. The layout for the laser power supply rack installed in the laser power supply chamber is in Fig. 42. A side view of the payload structure with the chamber installed is in Fig. 43 and a top view is Fig. 44. A photograph of the payload assembly mechanical structure is in Fig. 45. The partially assembled optical bench is shown in Fig. 46.

The CO₂ laser is shown in Fig. 47 with the lidar/laser in chamber mounting shown in Fig. 48. The laser power supply mounting configuration is shown in Fig. 49, and Fig. 50 shows the installation of the power supply mounting rack in the power supply chamber. The payload weight budget is in Table 9.

The lidar chamber and power supply chambers were integrated with the payload structure. The CO₂ laser was integrated with the lidar optical bench and installed in the lidar chamber. The hermetically sealed lidar and power supply chambers were successfully pressure tested and leak tested. The mechanical fit check of the CO₂ laser and the balloon payload was completed.

Table 8
Balloon Payload Environmental Specifications

Pressure

<u>Event</u>	<u>Definition</u>	<u>Comments</u>
Pre-Launch	14.7 psia \pm 4 psia	
Balloon Ascent 1,000 ft/min	14.7 psia to 0.029 psia	Ambient pressure change with altitude
Balloon Flight	0.16 psia to 0.029 psia (for up to six hours)	Float altitudes up to 100 000 ft
Test	15 psig for five hours no detectable leakage	Prelaunch pressure test on all chambers

Shock

<u>Event</u>	<u>Definition</u>	<u>Comments</u>
Launch	\pm 2.0 g, 70 ms, half sine all axes	No degradation of experiment system performance
Chute Opening	\pm 10 g, 70 ms, half sine all axes	Laser is not required to maintain alignment. No permanent damage is permitted. Optical misalignment is permitted.
Ground Impact	Can be > 10 g, any axis	Amount of damage will depend on terrain, horizontal impact velocity.
Test	2.0 g, 70 ms, z-axis only	No degradation of experiment system performance

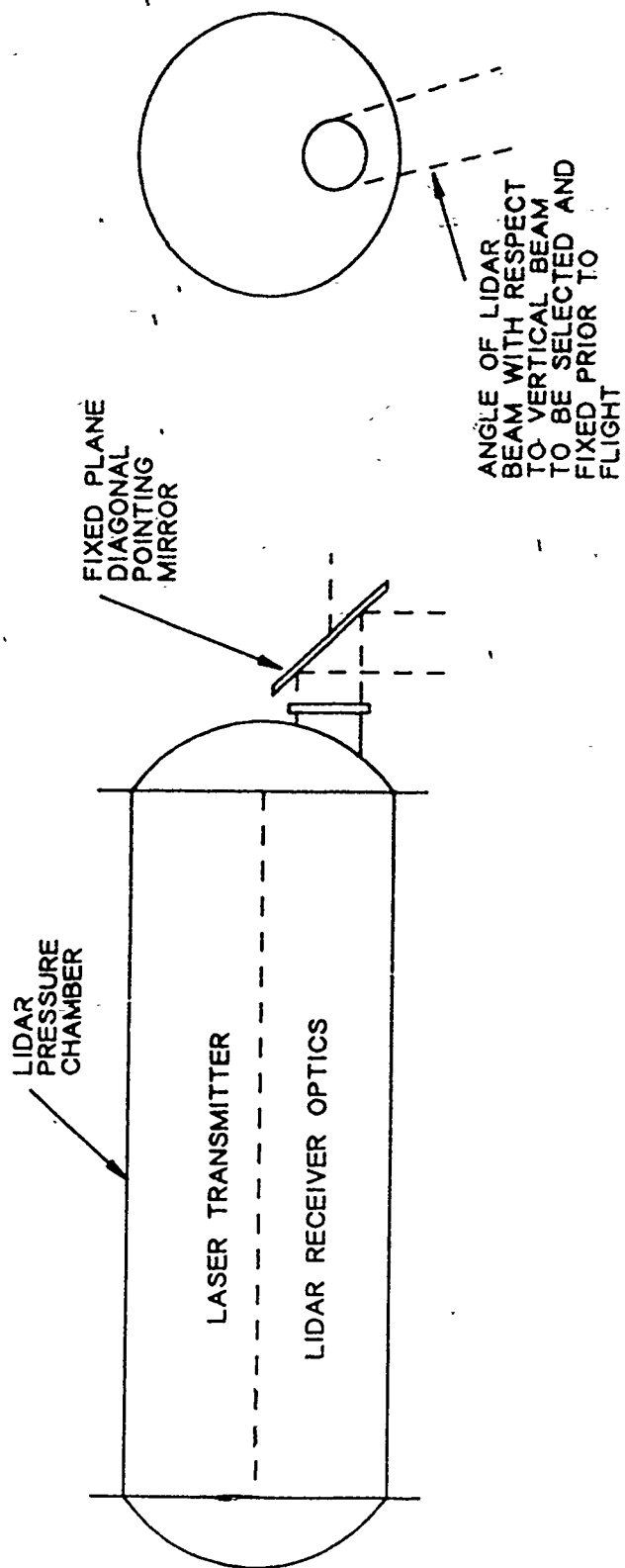


Figure 40. Lidar pressure chamber.

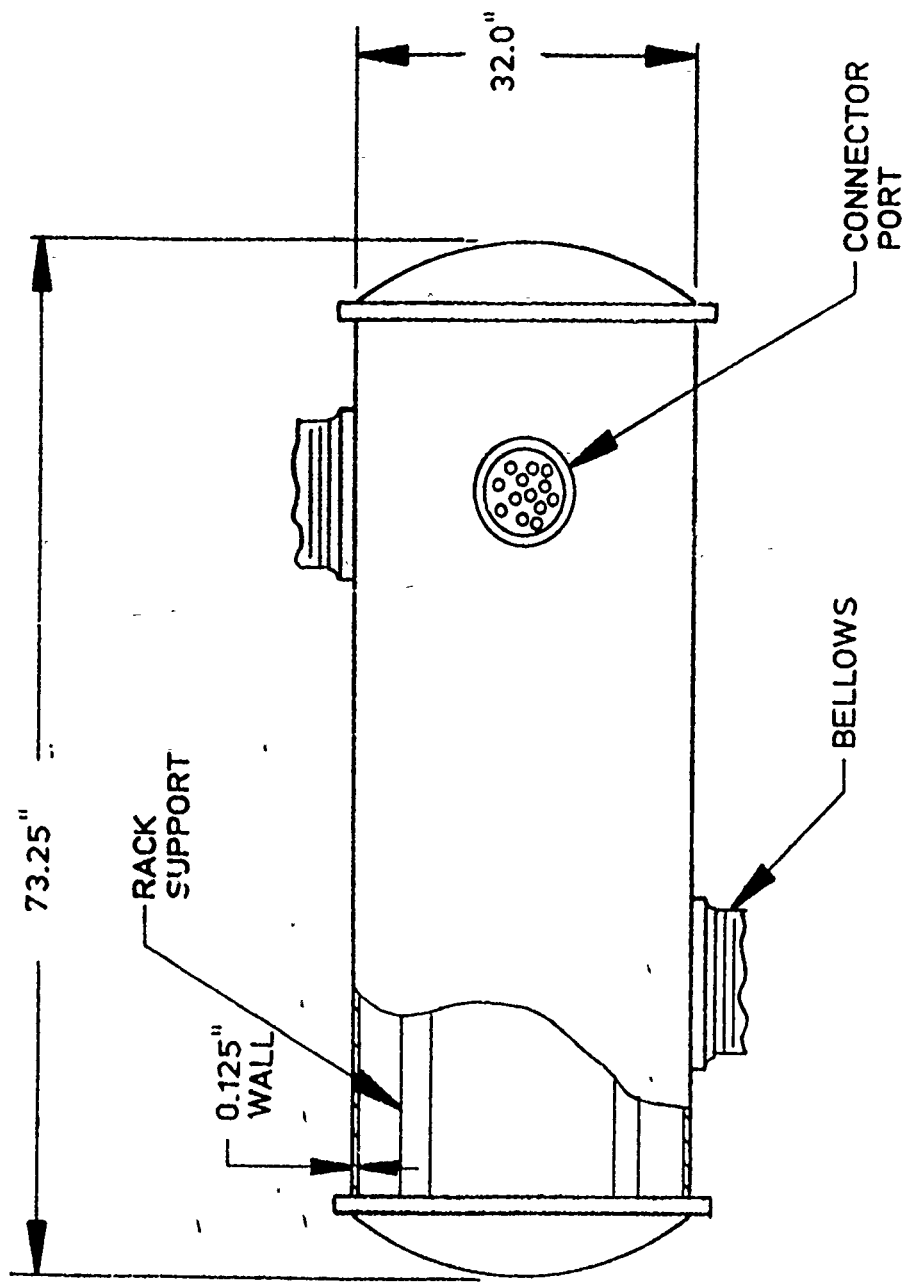


Figure 41. Laser power supply chamber.

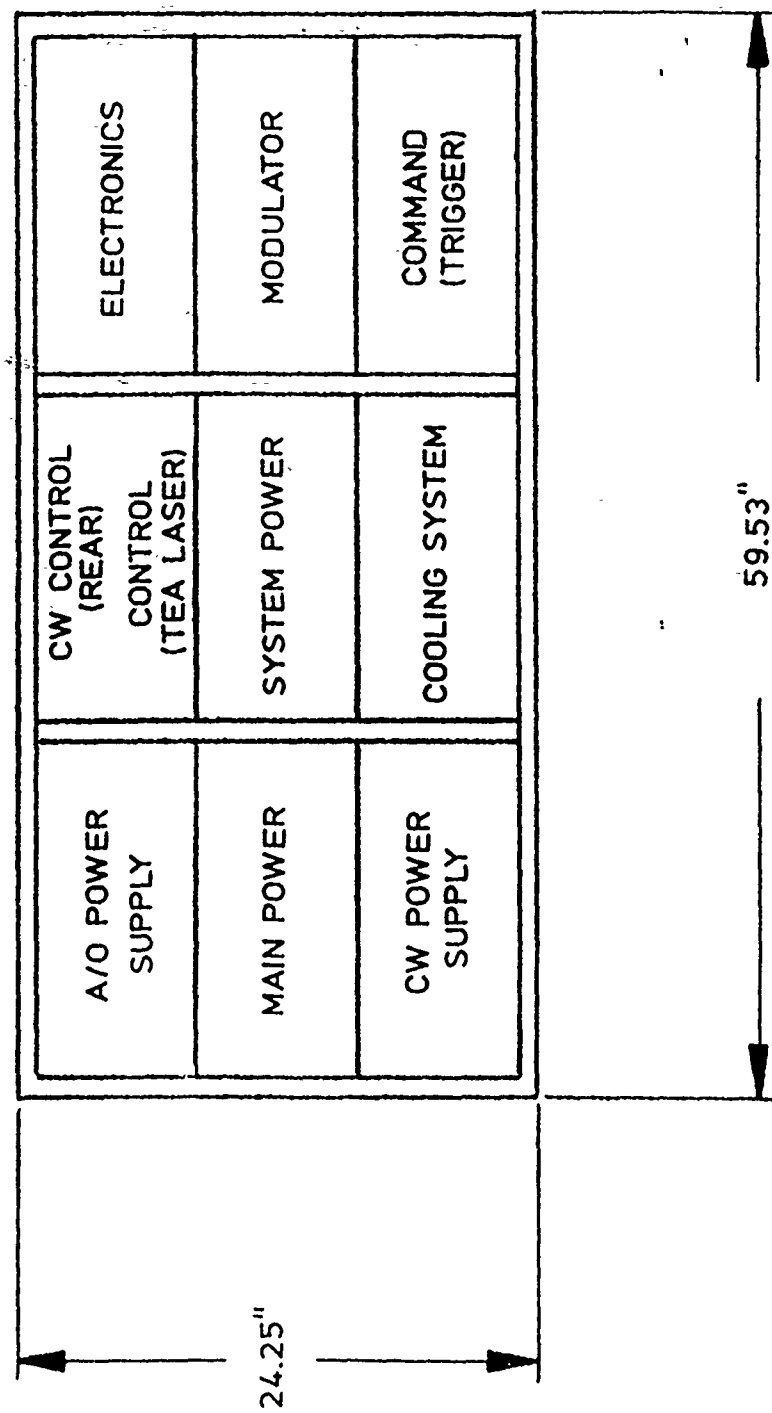


Figure 42. Laser power supply rack.

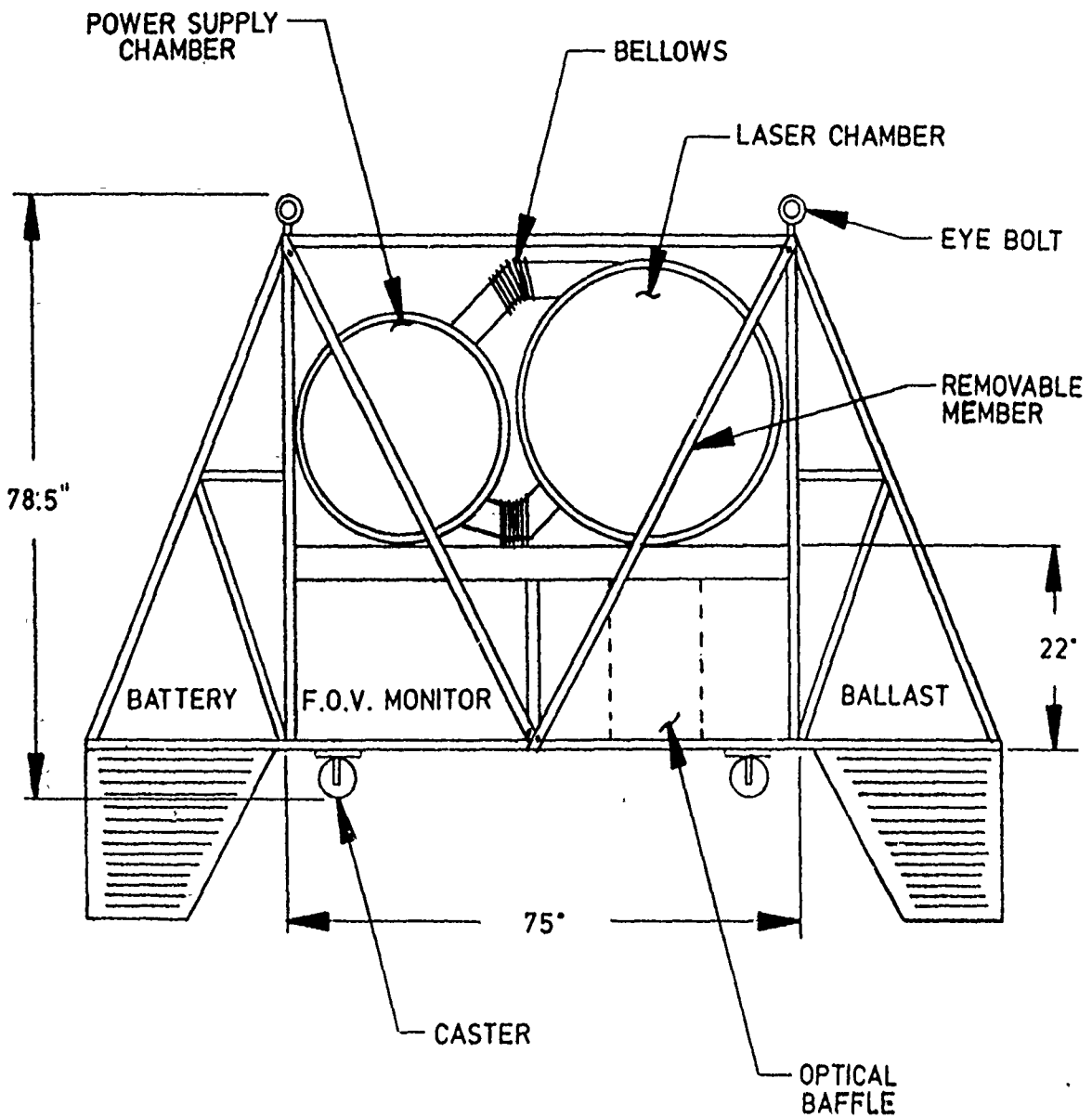


Figure 43. Balloonborne coherent CO_2 lidar payload, side view.

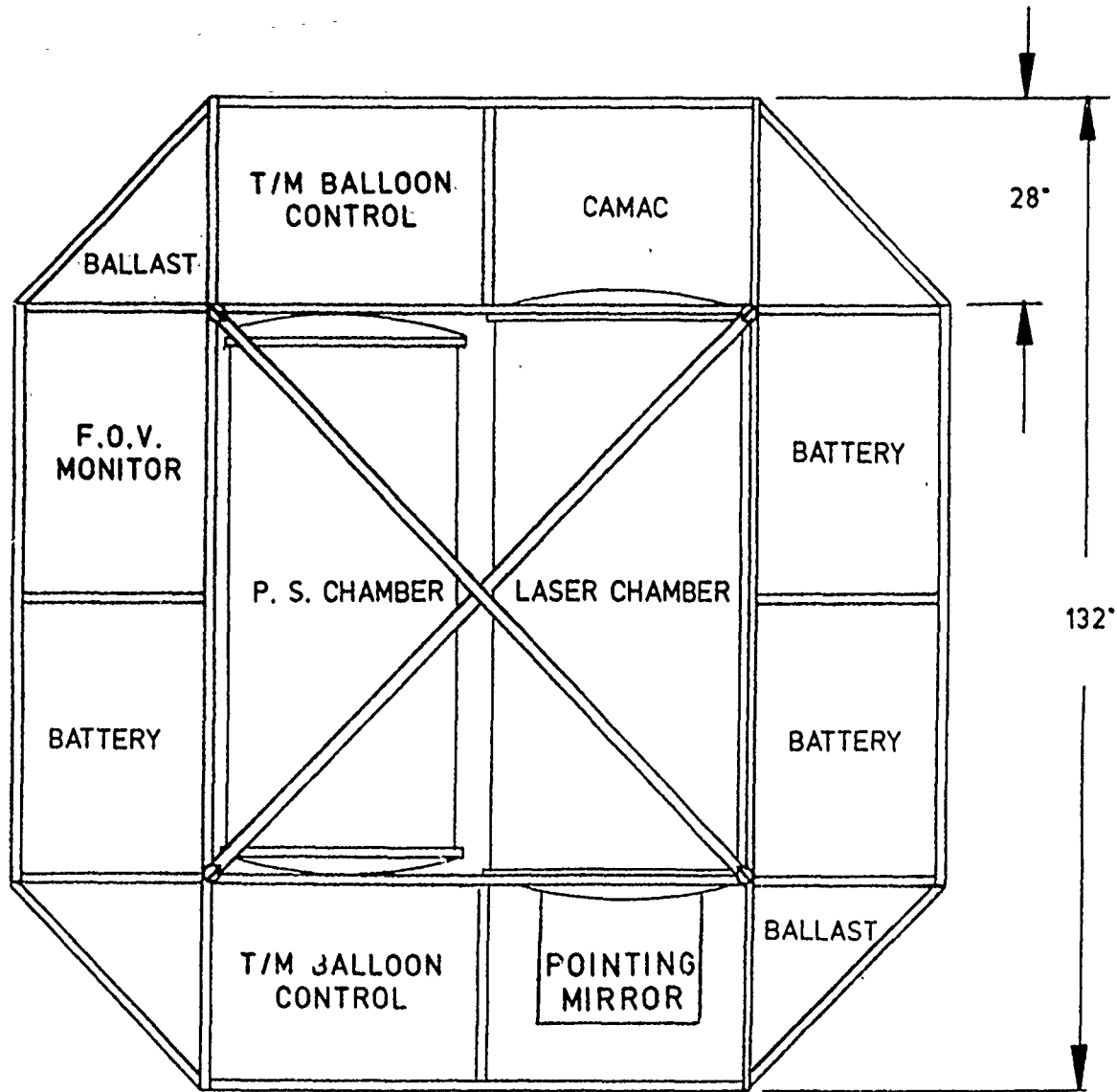


Figure 44. Balloonborne coherent CO_2 lidar payload, top view.

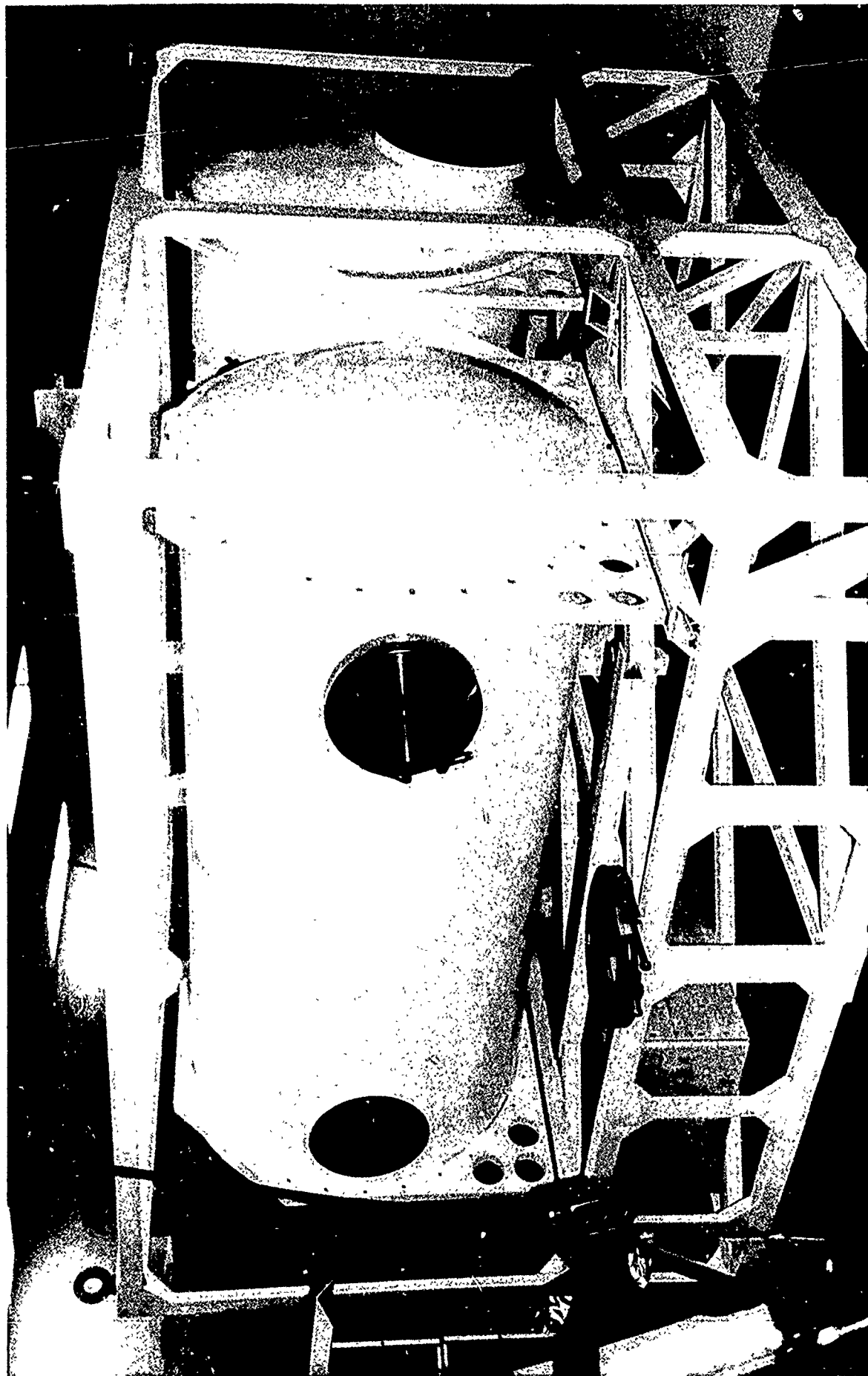


Figure 45. Lidar payload, assembled mechanical structure.

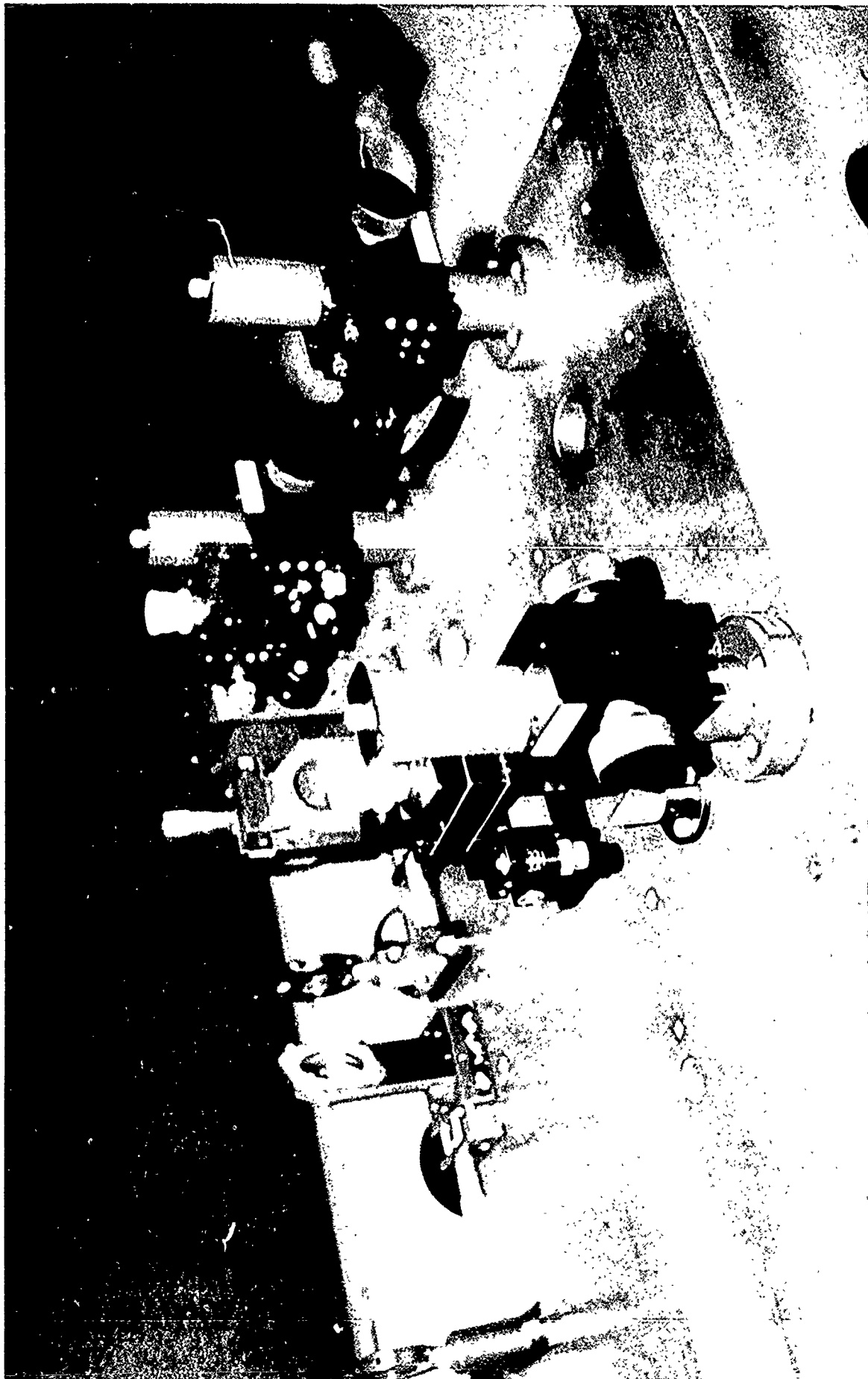


Figure 46. Coherent CO₂ lidar receiver optical bench.

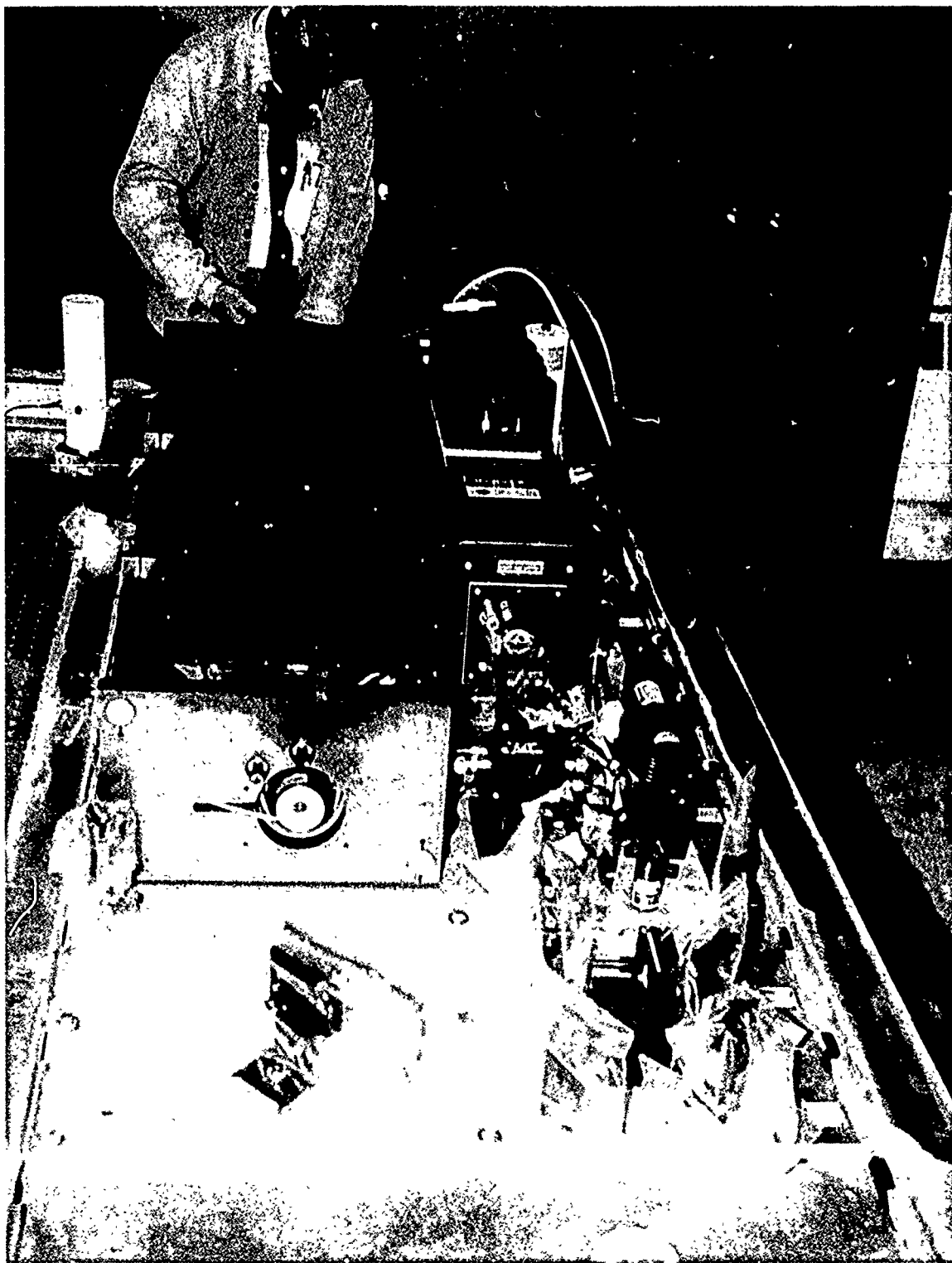


Figure 47. CO_2 laser.

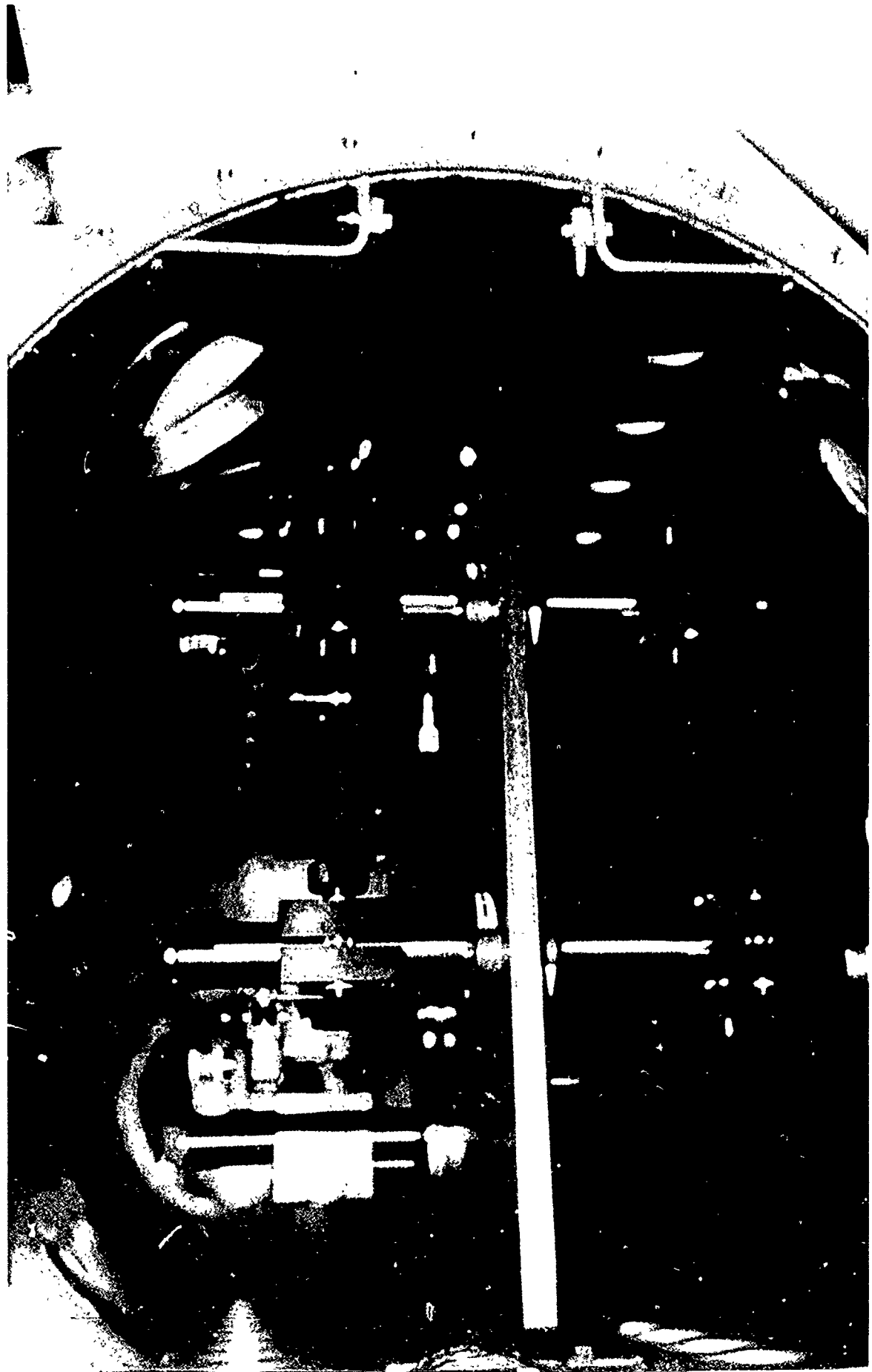


Figure 48. Receiver optical bench mounted in lidar pressure chamber.

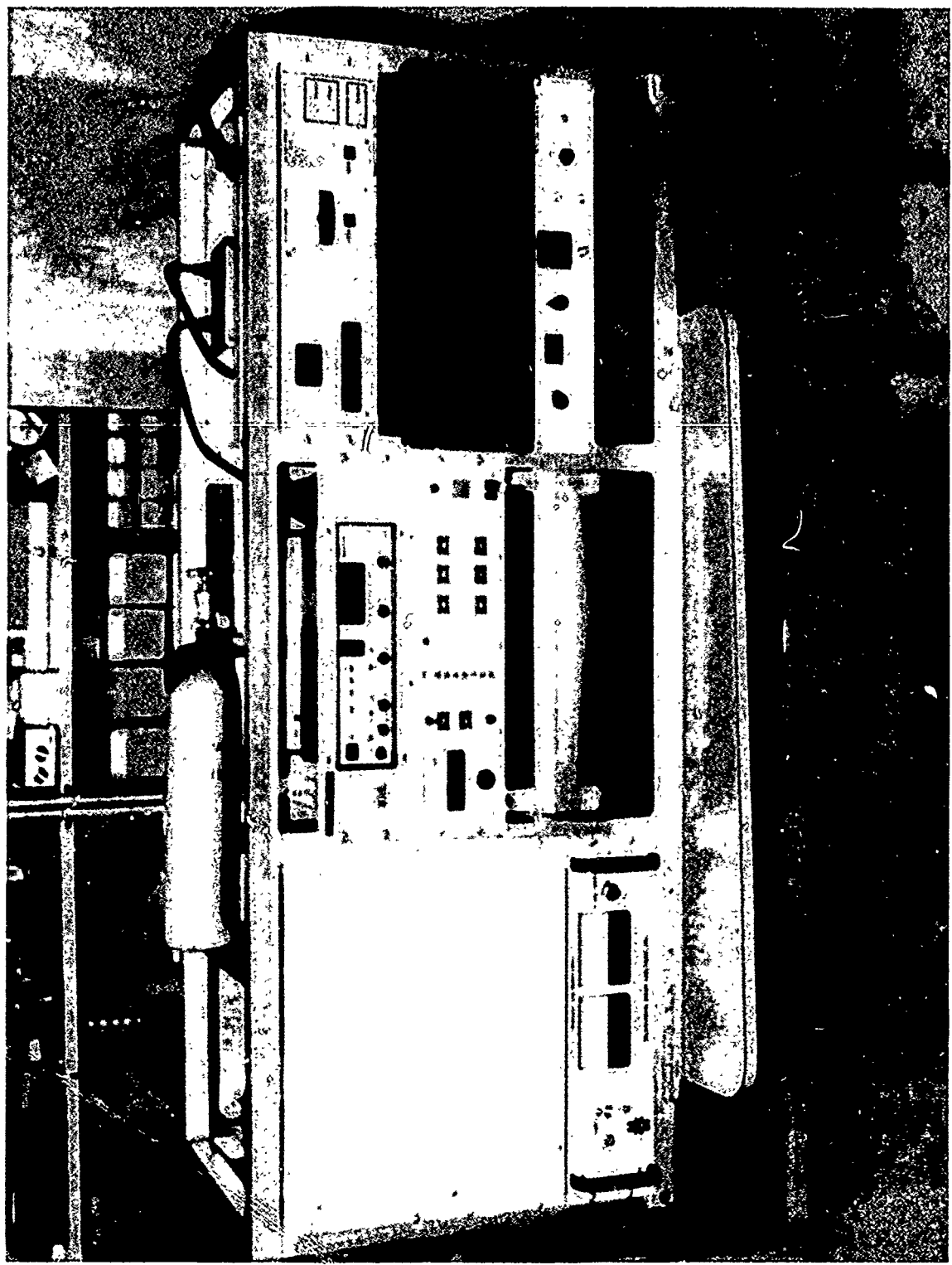


Figure 49. Laser power supplies and controls mounted in pressure chamber rack.

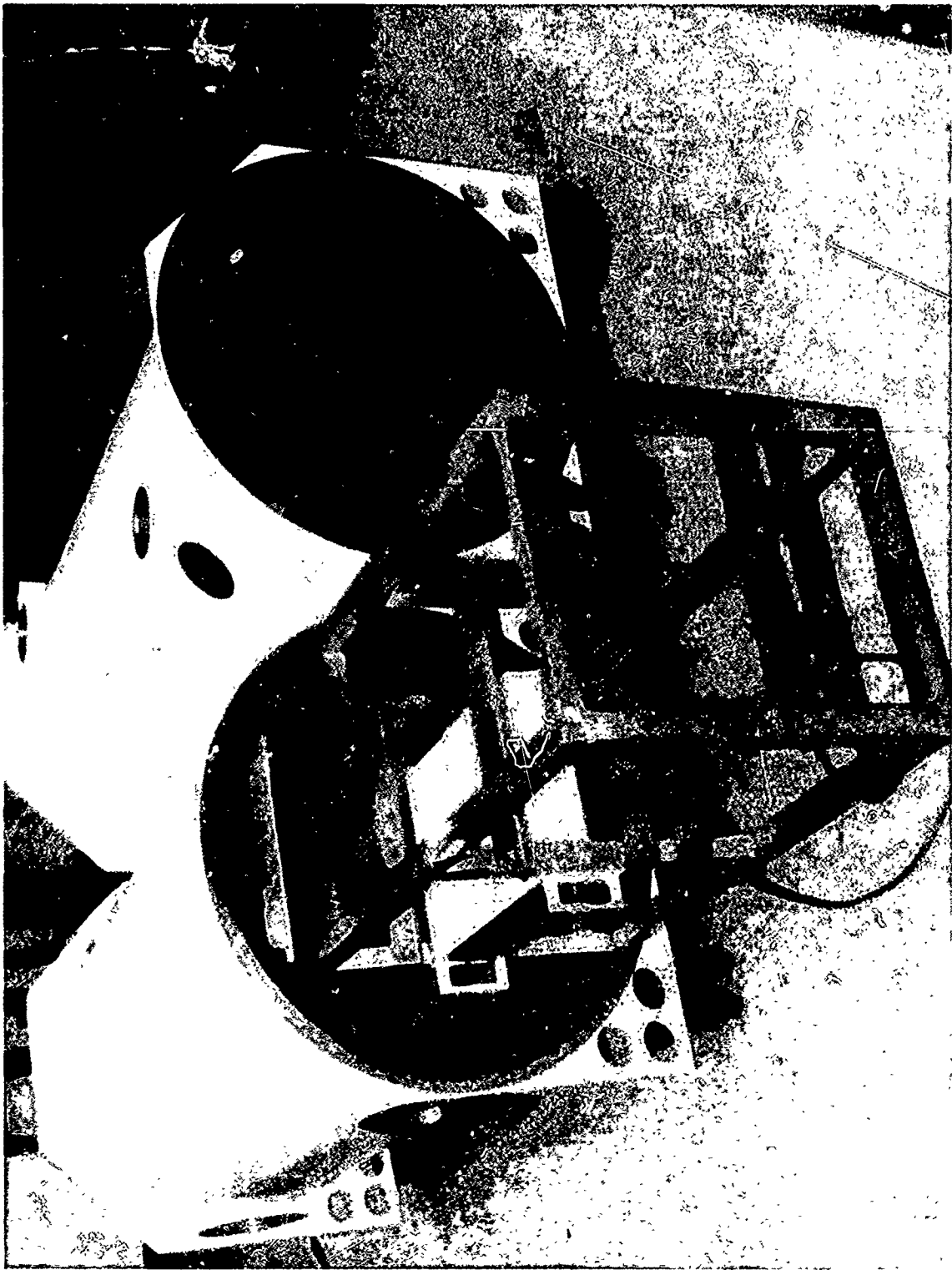


Figure 50. Chamber installation of laser power supply rack.

Table 9
CO₂ Lidar Payload Weight Budget

<u>Component</u>	<u>Weight (lb)</u>	<u>Basis</u>
Frame	690	C
Crush Pads (4)	48	W
Radiators (2)	102	C
Primary Balloon Control	46	LC
Backup Balloon Control	75	LC
Interface Electronics	45	LC
Batteries (12)	660	W
Coolant Reservoirs (3)	33	W
Compass	7	W
Receiver Power Supply	25	C
Temperature Monitor	3	W
Main Power Distribution	10	C
Laser Power Distribution	10	C
Laser/HG Controller	12	C
Baffle Assembly	100	C
Receiver Electronics (CAMAC)	100	W
Laser Chamber Assembly (237 # Chamber Only)	650	W/C
Laser Pwr. Sup. Chamber Assembly (200 # Chamber Only)	450	W/C
Power Supply Frame	41	W
Bellows System (2)	37	W
Cabling and Hardware	100	E
Coolant Fluid	28	E
Rigging	28	W
Insulation	25	E

Hardware	30	E
C-Band Beacon	50	LC
Transponder	25	LC
FOV Monitor	112	W

Subtotal	3451 lb
Ballast	600 lb
Parachute	<u>180</u> lb
	4231 lb

Basis Code

W = Actual Weight

E = Estimated

LC = Information Provided by LC

C = Calculated

6.2 Thermal Control System

The payload thermal environment specifications are in Table 10, and the lidar system thermal loads are in Table 11. A diagram of the payload thermal control system is in Fig. 51.

The CO₂ laser, when operating at the maximum pulse repetition rate dissipates 600 W in the TEA laser, 400 W in the cw laser and its power supply, and 350 W in the control electronics, for a total of 1.35 kW.

The thermal control system is based upon the premises that the lidar and power supply pressure chambers are wrapped with insulation to minimize radiative and convective heat loss and that the two chambers are thermally insulated from the payload structure. The two chambers are interconnected with two six-inch semiflexible tubes. By placing a vanaxial fan in one of the tubes the air will freely circulate between the two chambers providing for nearly uniform air temperatures in each chamber.

Since the radiative, conductive, and convective losses are minimized, the only way heat can be removed from the two chambers is by the ethylene glycol-water cooling fluid. Since this can be controlled, the chamber temperatures can be controlled. The chamber air (actually backfilled dry N₂) will be cooled with a liquid-air heat exchanger. Temperature control will be maintained by a fan on the exchanger.

The ethylene glycol-water coolant loop will remove the 1.35 kW from the lidar system pressure chamber and transfer the heat to a trichloroethylene coolant loop. This coolant flows through outboard-mounted radiator panels where the heat is radiated out from the payload into space. The trichloroethylene coolant is used because it retains its low viscosity over the wide range of temperatures encountered during a balloon flight.

The payload system interconnection cabling was previously shown in Fig. 39.

6.3 Power

The primary electrical power of the payload is 28 \pm 4 Vdc which is provided by rechargeable GFE Ag-Zn batteries. Each battery consists of 20 series-connected cells and has an 80 ampere-hour capacity. The payload power budget and battery requirements are listed in Table 12. This will provide sufficient power for eight hours of laser operation.

Table 10
Balloon Payload Thermal Environment Design Specifications

<u>Event</u>	<u>Definition</u>	<u>Comment</u>
Pre-Launch	5°C to 35°C	Operational
Balloon Ascent 1,000 ft./min.	-76°C @ 50,000 Ft. 25°C ± 10°C	Minimum ambient air temperature design goal required laser and receiver
	10°C to 35°C	CAMAC electronics temperatures
Balloon Float 6 Hours Duration (Max.)	-46°C to -20°C 25°C to 10°C	Ambient air temperature design goal required laser and receiver
	10°C to 35°C	CAMAC electronics temperatures
Test	Simulate Balloon Ascent & Float	Thermovac Test Chamber

Table 11
Thermal Load Summary

Lidar Chamber	
Laser Liquid/Liquid	500 Watts
Receiver	Negligible
Power Supply Chamber	
Laser P.S. Liquid/Liquid	500 Watts
Laser-Power Supply Liquid/Air	500 Watts
Thermal Control System	100 Watts
CAMAC Chamber	
Electronics	300 Watts

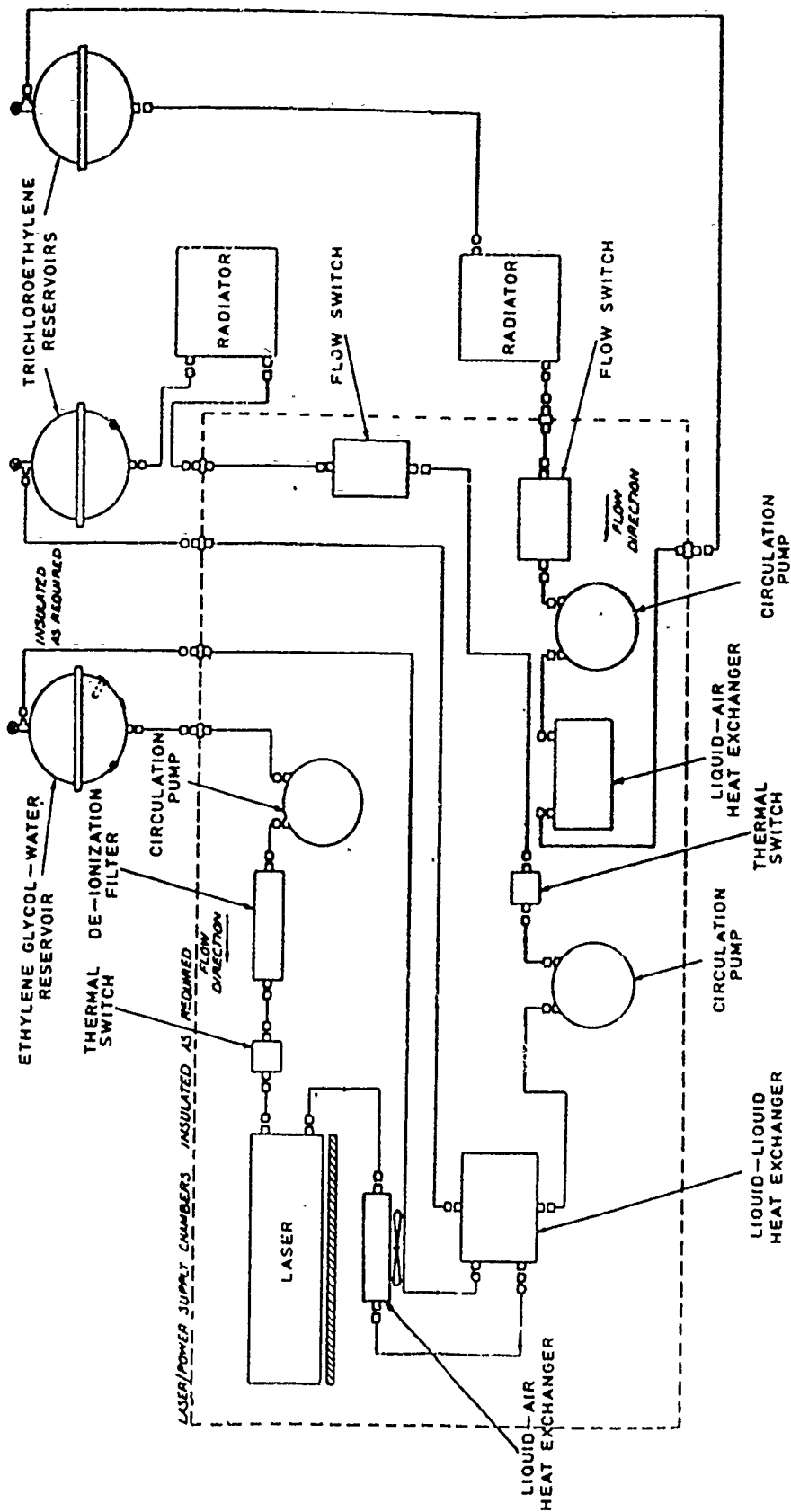


Figure 51. CO_2 lidar thermal control system.

Table 12
Payload Power Summary

<u>System</u>	<u>Estimated Power</u>	<u>No. of Batteries Req. (28 Vdc, 80 Ah)</u>
Laser	1750 Watts	6
Thermal Control	200 Watts	1
CAMAC Electronic	350 Watts	2
Housekeeping	120 Watts	1
FOV Monitor	180 Watts	1
Spare		1
	TOTAL	12

The laser requires 115 Vac 60 Hz power which is provided by three aircraft-type 28 Vdc to 115 Vac inverters¹¹²¹. The inverters are rated by the manufacturer to operate at altitudes up to 55,000 ft. To qualify them for balloon operation, a single inverter was tested in a high altitude test chamber. The inverter was set up to drive a variable dummy load. The single inverter operated reliably at a simulated altitude of 100 000 ft and a temperature of -60°C while delivering 825 volt-amperes to the load. The inverters are designed for multiple parallel operation, so using three inverters in parallel to drive the 1350 watt laser load will permit each inverter to operate at 55 percent of its test-rated output power.

6.4 Data

The primary lidar data are those acquired by the heterodyne detector. For backscatter data the modulation envelope of the 40 MHz modulated signal is detected, filtered, and sampled at 2 MHz for 10 bit digital conversion. The laser pulse repetition rate is 100 pps. Speckle noise in the backscatter returns requires that a minimum of 10 pulses be averaged to be interpretable as data. Thus, the basic PCM data rate will be 10 major frames/second. Each major frame will contain 600 heterodyne detector data words for two gain settings, each a 10 shot average of a 75 meter range bin. Approximately 50 samples will be acquired prior to laser firing to provide a noise measurement.

The data to the downlink are listed in Tables 13 through 21. Both temporal and range averaging of the data can be done during postflight data analysis. The estimated downlink PCM data rate is 200 kilobits/sec. The data will be in a standard IRIG PCM format, biphase encoded and outputted to telemetry. Premodulation filtering is to be provided by telemetry.

6.5 Experiment Control Software

The control software for the experiment consists of a program which provided the real-time control of the Raman detection lidar system. This program, written in MS-FORTRAN and C, will be developed on a PC-386 computer using MS-DOS operating system. The developed and tested program will then be loaded into EPROM and installed in the payload CAMAC electronic crate where it will be integrated with the flight PC-386 computer.

Table 13
Thermal Control Monitors/Data

Primary Coolant (Reservoir) Temperature
Secondary Coolant (Reservoir) Temperature
Power Supply Coolant (Reservoir) Temperature
TEA Laser Radiator Input Temperature
TEA Laser Radiator Output Temperature
TEA Laser Input Coolant Temperature
TEA Laser Output Coolant Temperature
Power Supply Radiator Input Temperature
Power Supply Radiator Output Temperature
Lidar Chamber Air Temperature
Power Supply Chamber Air Temperature
CAMAC Chamber Air Temperature
CAMAC Power Supply Temperature
Laser Power Inverter Temperature
Payload Frame Temperature

Table 14

CO₂ Laser Data

Analog Data - 10 Bit Digitization
LO Power High Gain
LO Power Low Gain
Fast Detector Discriminator
LO EMT Voltage
TEA Laser EMT Voltage
TEA Laser Avg. ($\tau = 100$ msec) Power
Digital Data - 1 Bit
Main Interlock
Filament Cold
Laser Head
Water Flow
Gas Pressure
Laser Head Fan
Regenerator
Ground Test Data
Slow Detector (BW $\simeq 10$ MHz)
Fast Detector (BW $\simeq 10$ MHz)

Table 15
Receiver Data

TEA Laser Power Monitor (Transmitted Pulse Power)
Envelope Detection High Gain Envelope Détection Low Gain
Optical Bench Temperature Monitors (4)
Lidar Chamber Air Temperature Monitor
Lidar Chamber Pressure Monitor
Optical Adjustment Encoders (6)
Detector DC Signal (LO Power Incident or Detector)

Table 16

CO₂ Laser Controls

<u>Analog Voltages - 10 Bit Digitization</u> LO Offset Control LO Bias Control TEA Laser Control
<u>Switch Closures</u> LO Stab Switch TEA Laser Stab Switch TEA Laser Filter Switch 28 VDC/115-VAC Inverters ON/OFF Power Supply ON/OFF Laser Head ON/OFF High Voltage ON/OFF Regenerator ON/OFF
<u>Ground Controls</u> HeNe Laser ON/OFF High Voltage Adjust (Preset and Locked for Flight) Preamplifier Battery Charge

Table 17
Receiver Controls

Analog Voltage - Bit Digitization
Focus Lens X Adjust Focus Lens Y Adjust
(4 remote optical adjustments to be defined)
RF Amplifier Gain Control
Switch Closure Preamplifier ON/OFF RF Amplifier ON/OFF
Ground Control Preamplifier Battery Charge

Table 18
Thermal Control Functions

Interchamber Fan	
Primary Coolant Pump	Automatically ON when Laser Power ON
Primary Coolant Reservoir Heater	Thermostat Controlled
Primary Coolant Liquid/Air Heat Exchanger Fan	
Secondary Coolant Pump	Thermostat Controlled
Power Supply Liquid/Air Heat Exchanger Fans	Thermostat Controlled
Power Supply Coolant Pump	Thermostat Controlled

Table 19

CO₂ Lidar Payload

Balloon Control Interface
Mechanical
Primary Balloon Control (Visidyne Dwg. 662-3-03)
Backup Balloon Control (Visidyne Dwg. 662-3-035)
C-Band Beacon
FAA Transponder
Balloon Payload Rigging
Electrical
High Rel/Safety Uplink Commands
Modem Uplink Commands
Lidar PCM Data
Balloon Control PCM Data

Table 20
High Reliability/Safety Commands

Laser Power ON/OFF
Laser ARM/SAFE
Laser Fire (Continuous Command Transmission Required for Laser Firing)
Interlock Override (2)
RCVR Power ON/OFF
Thermal Control Power ON/OFF
Housekeeping Power ON/OFF
FOV Monitor Power ON/OFF
Computer Boot
Spare (4)

Table 21
Balloon Control

PCM Data

Laser Power
Laser ARM
Laser Fire
Receiver Battery Voltage
Spare (10)

The program is a derivative of the previously developed and flight-tested experiment control programs.

6.6 Functional Description

BCBL Functional Description

Figure 52 is a block diagram of the BCBL program architecture. The functions of the program and of each subroutine are listed below.

BCBL

1. System data inputs.
2. To call subroutines INITC and XMITC.

INITC

1. Initialize CAMAC crate controls.
2. Initialize CAMAC modules.
3. Initialize PCM array.
4. Initialize system timing.

XMITC

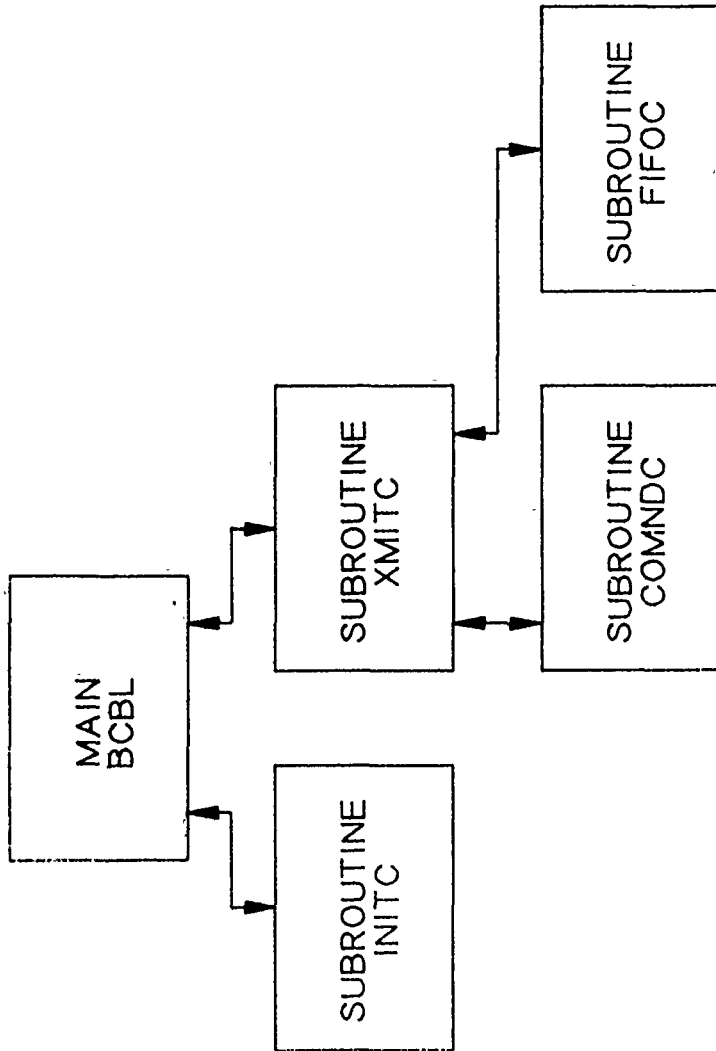
1. Rayleigh Data - Upon completion of the digitization of the 1200 data samples for each of two heterodyne detector gain channels, the data are transferred by DMA to the PCM array.
2. Housekeeping Data - Up to 64 channels of housekeeping data are scanned, digitized, and transferred to the PCM array.
3. PCM Array - The contents of the PCM array are DMA transferred using FIFO to the PCM serial encoder for telemetry transmission to the ground station.
4. Command - The input serial port buffer is checked for uplinked command characters, and if ACCESS REQUEST has been set, the characters are transferred to COMNDC.

COMNDC

1. Perform a conditional branch, based upon the valid character transferred from XMITC, to the appropriate command routine.
2. Perform the selected routine and return to XMITC.

Figure 52. Program BCBL architecture.

89-449



7. CURRENT STATUS OF CO₂ LIDAR SYSTEM

Lidar

The optical design has been completed. All small optical components have been procured. The optical bench has been fabricated and integrated with laser and chamber.

The designs of the telescope structure and optics are complete.

Chambers

Lidar and power supply chambers have been designed, fabricated, and tested.

Chambers have been pressure-tested and leak-tested.

Lidar optical bench with laser optical bench have been integrated and installed in lidar chamber.

Laser electronics and power supplies have been mounted in rack and installed in power supply chambers.

Payload

The payload structure design and fabrication have been completed.

Power supply and lidar chambers have been installed on payload.

Lidar Electronics

The design of the lidar data processing electronics, which utilizes a CAMAC system, has been completed. Detailed designing of the RF electronics and coding of the real-time control system software remain to be done. It is recommended that the existing ABLE CAMAC system be modified to meet the lidar data requirements of this system.

Lidar Power System

The design is complete, and a full power test of the lidar power inverter was conducted in a high altitude vacuum chamber.

Thermal Control

The control system design has been completed.

Payload Housekeeping Systems

Most of the housekeeping system will be based upon the ABLE designs.

Payload Cabling

The cabling design is complete, but detail cable drawings must be completed.

8. TASKS TO BE DONE

The following tasks remain to be completed:

- Telescope and diagonal pointing mirror fabrication, assembly, and alignment.
- Procurement of lidar chamber IR window.
- Lidar assembly and alignment.
- Lidar ground test and calibration.
- Lidar electronics fabrication and assembly.
- Lidar power system assembly.
- Thermal control system parts procurement and assembly.
- Payload housekeeping system design and fabrication.
- Payload assembly.
- Payload cable fabrication.
- Payload integration.
- Payload thermovac test.
- Lidar ground test and calibration flight test.

9. CONCLUSIONS AND RECOMMENDATIONS

In the course of the lidar optical design, a detailed wavefront tolerance analysis of the transmit, receive, and local oscillator optical components was performed. The results of this analysis showed that to attain a high heterodyne detection efficiency, the wave front errors of each optical component must be minimized. If the lidar system wave front errors are measured interferometrically during system optical alignment and confirmed to be within the specific limits, then a highly sensitive coherent lidar system performance will be attained.

Although the payload and lidar system are only partially complete at this time, the most challenging engineering tasks have been completed and many long lead components have been procured. The design of the entire lidar payload is nearly complete.

It is recommended that the Balloonborne Coherent Lidar System be completed and flight tested. The completion would be undertaken in two phases. During Phase I the lidar optics, telescope, CO₂ laser, and lidar data processing and control electronics would be fabricated and tested. A ground test sequence would be included in this phase.

For Phase II the balloon payload would be assembled and integrated with the lidar system. A thermovac test of the integrated system in a high altitude chamber would provide a simulated flight test at a to-be-designated launch site. A fully operation data acquisition flight would then be conducted.

10. REFERENCES

1. O. Shepherd, G. Aurilio, R.D. Bucknam, R.W. Brooke, A.G. Hurd, and T.F. Zehnpfennig, "Balloonborne Lidar Experiment", Final Report, Contract No. F19628-80-C-0094, AFGL-TR-80-0373, Visidyne, Inc. (1980). ADA095366.
2. O. Shepherd, G. Aurilio, R.D. Bucknam, A.G. Hurd, and W.H. Sheehan, "Project ABLE Atmospheric Balloonborne Lidar Experiment", Final Report, Contract No. F19628-81-C-0165, AFGL-TR-85-0064, Visidyne, Inc. (1985). ADA160372
3. PRF-1505, CO₂ Laser Operators Manual, Laser Sciences, Inc., Cambridge, MA.
4. EMT Translator & Stabilization System 901 Manual, MPB Technologies, Inc., Keene, NH.
5. J. Bilbro, NASA/Marshall SFC (private communication, 1987).
6. S.C. Cohen, Appl. Opt. 14, 1953 (1975).
7. M.L. Moreau, Exotic Materials, Inc., Costs Mesa, CA (private communication, 1987).
8. J. Adams, Eagle-Picher Industries, Inc. Quapaw, OK (private communication, 1987).
9. H.W. Vandermeer, Optical Systems and Technology, Inc., N. Billerica, MA (private communication 1987).
10. R.H. Kingston, "Detection of Optical and Infrared Radiation", Springer-Verlag, Berlin (1978).
11. O. Shepherd, G. Aurilio, A.G. Hurd, R.J. Rieder, and W.P. Reidy, "Balloonborne Coherent CO₂ Lidar Experiment, R&D Design Evaluation Report", Visidyne, Inc., VI-1046A (1989).
12. Avionics Instruments, Inc. Static Inverter Model 3A1000-1G, Installation Manual.